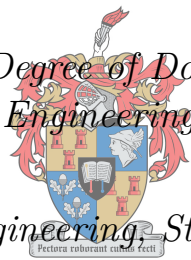


Magnetic Modelling, Analysis and On-Chip Shielding of SFQ Circuits

Rodwell Simeon Bakolo

Dissertation presented for the Degree of Doctor of Philosophy in Electronic Engineering



at the Faculty of Engineering, Stellenbosch University

UNIVERSITEIT
iYUNIVESITHI
STELLENBOSCH
UNIVERSITY

100
1918 · 2018

Supervisor: Professor Coenrad J. Fourie

Department of Electrical and Electronic Engineering

March 2018

Declaration

By submitting this dissertation electronically, I declare that the entirety of the work contained therein is my own, original work, that I am the sole author thereof, that reproduction and publication thereof by Stellenbosch University will not infringe any third party rights and that I have not previously in its entirety or in part submitted it for obtaining any qualification.

Rodwell Simeon Bakolo

Date: March 2018

Abstract

Single Flux Quantum (SFQ) based electronic circuits are susceptible to failure if exposed to external magnetic fields, even in very small quantities. Operating margins of SFQ circuits have shown to decrease significantly in the presence of magnetic fields as small as $5 \mu\text{T}$. This challenge makes SFQ circuits infeasible for the normal environment in which other technologies, such as CMOS, operate. Sources of magnetic fields include SFQ circuit's own bias lines, the Earth, which can produce magnetic fields up to $65 \mu\text{T}$ and any other electromagnetic interference sources. Without protective measures, most SFQ circuits cannot work in the open environment.

By using the tools available in the inductance extraction tool, *InductEx*, a method for projecting uniform magnetic fields, of varying orientations on SFQ cells, strides have been made to make SFQ circuits more tolerant to magnetic fields. On-chip analysis of SFQ cells was done in the presence of magnetic fields from the x , y and z orientations. In addition, by varying currents in 3-D coils, the orientation of the magnetic fields can be varied. This way, it is now possible to analyse bias, parameter and operating field margins of SFQ cells in any direction of the magnetic field.

Two on-chip shielding solutions were analysed and developed. The conventional continuous superconductor layer shield, dubbed the solid shield, and the grid shield. The grid shield resembles a Faraday cage and it is implemented by laying out bars of $2.5 \mu\text{m}$ width using the topmost layer in the *Hypres'* 4.5 kA/cm^2 process. The solid shield is more effective against perpendicular (z -directed) magnetic fields than against those in-plane (x and y -directed). In addition, the solid shield's inclusion in SFQ cells results in the reduction of circuit inductance by up to 25 %. The grid shield is a very effective approach against in-plane magnetic fields. However, its effectiveness is inversely proportional to the spacing between grid bars. Compared to the solid shield, the grid shield has less effect on circuit inductance with a typical reduction of 8 % at a grid bar spacing of $5 \mu\text{m}$. The large reduction in inductance can be overcome by making the inductors thinner and shorter. Shielding effectiveness of on-chip shields is enhanced by making ground contact vias from the shield layer to the ground plane. So far, uniformly grounded shields have shown to be the most effective approach.

The solid shield improved the operating field margin of a DFF cell against a z -directed magnetic field from $30 \mu\text{T}$ to $531 \mu\text{T}$, while the grid shield, of $5 \mu\text{m}$ grid spacing, improved the margins from $68 \mu\text{T}$ to $290 \mu\text{T}$ against an x -directed magnetic field. In the DC-SFQ cell, the operating field margin was improved with a solid shield from $47 \mu\text{T}$ to $464 \mu\text{T}$, against a z -directed magnetic field, while with a grid shield, the improvement was from $211 \mu\text{T}$ to $381 \mu\text{T}$, against an x -directed fields.

To further enhance the magnetic field tolerance of SFQ circuits, design tenets that target specific components, such as inductors, were analysed. Thin and narrow inductors have shown less coupling to external magnetic fields. In addition, moats have shown to influence OFM results depending on the orientation of magnetic fields.

This work has delivered design and analysis methods for magnetic field tolerant SFQ circuits.

Opsomming

Elektroniese stroombane gebaseer op Single Flux Quantum (SFQ) tegnologie is sensitief vir selfs klein eksterne magnetiese velde. Werkbereik van SFQ stroombane is reeds gedemonstreer om beduidend te verklein wanneer die bane vloeddigtheid so laag as $5 \mu\text{T}$ ervaar. Dit is een van die uitdagings wat SFQ bane onprakties maak in die tipe werksomgewings waar ander tegnologieë soos CMOS normaalweg opereer. Magnetiese veldbronne sluit die voorspanningslyne van die SFQ bane en die geomagnetiese veld in. Laasgenoemde kan vloeddigtheid van tot $65 \mu\text{T}$ bedra. Ander elektromagnetiese steurnisse kan ook die werking van SFQ bane beïnvloed, sodat SFQ bane nie sonder beskermende maatreëls in 'n oop omgewing kan funksioneer nie.

Deur die gebruik van die gereedskap beskikbaar in die induktansie-onttrekkingsmodule InductEx, naamlik 'n metode om uniforme magneetvelde met veranderende oriëntasie oor SFQ selle aan te lê, is groot vordering gemaak om SFQ stroombane meer vas te maak teen magnetiese velde. Analise van SFQ selle soos dit op 'n mikroskopiese geïmplementeer word, is simulasierigig in die teenwoordigheid van magnetiese velde met x -, y - en z -oriëntasie verrig. Sodoende is dit nou moontlik om voorspanning-, parameter- en veld-werkbereik van SFQ selle te analiseer vir enige veldrigting.

Twee afskermingsoplossings vir geïntegreerde skyfies uitlegte is ontwikkel en geanaliseer: die konvensionele kontinue supergeleier afskermingslaag – of soliede afskerming – en rooster-afskerming. Rooster-afskerming benader 'n Faraday kou, en is geïmplementeer deur die uitleg van stroke met $2.5 \mu\text{m}$ wydte in die boonste supergeleierlaag van Hypres se 4.5 kA/cm^2 proses. Soliede afskerming is meer effektief teen loodregte magnetiese velde (in die z -rigting) as teen velde in die xy -vlak. Soliede afskerming verlaag egter stroombaaninduktansies met ongeveer 25 %. Rooster-afskerming is 'n baie effektiewe metode teen xy -geïoriënteerde magnetiese velde, maar effektiwiteit is omgekeerd eweredig aan die spasiëring tussen stroke. Vergeleke met soliede afskerming, het die rooster-afskerming 'n kleiner effek op stroombaaninduktansie, met tipies slegs sowat 8 % vermindering wanneer strookspasiëring $5 \mu\text{m}$ is. Afskermingseffektiwiteit word verbeter deur grondkontakte van die afskermingslaag na die grondvlak. Eweredig-gegronde afskermings is aangetoon om die mees effektiewe benadering te wees.

Soliede afskerming verbeter die veld-werkbereik van 'n DFF sel in z -gerigte magneetvelde vanaf $30 \mu\text{T}$ tot $531 \mu\text{T}$, terwyl rooster-afskerming met $5 \mu\text{m}$ strookspasiëring die veld-werkbereik in x -gerigte magneetvelde vanaf $68 \mu\text{T}$ tot $290 \mu\text{T}$ verbeter. In die GS-na-SFQ sel is die veld-werkbereik met soliede afskerming verbeter vanaf $47 \mu\text{T}$ tot $464 \mu\text{T}$ in z -gerigte magneetvelde, terwyl dit in x -gerigte magneetvelde vanaf $211 \mu\text{T}$ tot $381 \mu\text{T}$ verbeter is met rooster-afskerming.

Vir verdere verbetering van die magnetiese veldtoleransie van SFQ bane, is ontwerpmetodes vir spesifieke komponente, soos induktore, ontwikkel. Dun en nou induktore is aangetoon om swakker te koppel met eksterne magneetvelde, terwyl gragte in die grondvlak aangetoon is om veld-werkbereik te beïnvloed.

Hierdie werk stel ontwerp- en analisemetodes daar vir magnetiese veldvaste SFQ bane.

Acknowledgements

I would like to thank my supervisor, Professor Coenrad J. Fourie for the expert guidance throughout my research and Prof. Pascal Febvre for the numerous discussions that led to some of the achievements in this work.

I also acknowledge the various contributions colleagues in the research group offered towards the successful completion of my work. A special mention goes to Dr. Nicasio Maguu Muchuka, Ruben van Staden, Johannes A. Delpont and Kyle Jackman.

The Malawi Government through funds from the African Development Bank, and the HEST project funded this research. I would like to thank the policy makers and all who made it possible for the funds to trickle down to support my studies.

Lastly, but in no way least, I give special thanks to my dear wife, Fatima, and daughter, Ivana, for enduring many days without me. Thank you for the understanding and the sacrifices you had to make as I ran away from you, time and again, to pursue my studies.

List of Publications

1. Modelling of the Influence of Magnetic Fields on the Operation of Digital Superconductive Circuits

Rodwell S. Bakolo and Coenrad J. Fourie

Conference: *15th International Superconductive Electronics Conference (ISEC), 2015*

Abstract:

We present a simulation model for analysing and predicting magnetic field patterns and their influence on superconductive digital circuits. Unwanted magnetic fields can cause these circuits to experience reductions in operating margins or fail completely. We use *InductEx* to simulate the effect of running current carrying conductors around and above the circuit under study. We also use coils to mimic ambient fields. As a test bed, D-flip flops from both RSFQ and eSFQ libraries were simulated in a roughly uniform magnetic field and the coupling to every circuit inductance is recorded. From these results we construct models that link circuit inductance and by association the bias current distribution, to applied magnetic fields.

2. Modelling Magnetic Fields and Shielding Efficiency in Superconductive Integrated Circuits

Rodwell S. Bakolo. Ruben. van Staden. Pascal Febvre. Coenrad J. Fourie

Journal: *Journal of Superconductivity and Novel Magnetism, 2016*

Abstract:

We present a magnetic field model that shows how Single Flux Quantum (SFQ) based electronics can be affected by nearby current carrying strip lines and other external magnetic field sources. This work is an enabling step towards the design of SFQ circuits that can operate without the need for ferromagnetic shielding. Firstly, a specific 3-D coil system was optimized to apply external homogeneous magnetic fields during a magneto-quasistatic numerical analysis of a SFQ Delay-Flip-Flop (DFF) circuit. We used magnetic field and current density visualization tools to identify the most affected areas in the circuit layout. Secondly, grid patterned and solid on-chip shielding techniques were verified through simulations to design magnetic field tolerant SFQ circuits. Without any form of shielding, the DFF operated up to maximum external magnetic field of $38 \mu\text{T}$ or $46 \mu\text{T}$, whereas with magnetic shields, the DFF failed at $50 \mu\text{T}$ or $98 \mu\text{T}$ and $50 \mu\text{T}$ or $86 \mu\text{T}$ for the grid and solid shields, respectively. Both shields have comparable failure points for the DFF. However, the grid based shield has a lower influence on SFQ circuit inductance, requiring a faster re-optimization without the need to redesign the circuit.

3. Analysis of a Shielding Approach for Magnetic Field Tolerant SFQ Circuits

Rodwell S. Bakolo, Johannes A. Delport, Pascal Febvre and Coenrad J. Fourie

Journal: *IEEE Transactions on Applied Superconductivity*, 2017

Abstract:

The operating margins of unshielded SFQ circuits are influenced by external magnetic fields, and earlier research showed experimental results of operating region versus bias current for circuits with in-plane and perpendicularly applied magnetic fields. Here we report a method that can be used to analyse shields to protect SFQ circuits from external magnetic fields. To validate the approach, we investigated a grid patterned shield of varying spacing. The analysis was done with cell layouts made according to the *Hyppres'* 4.5 kA/cm² process, in which the top-most layer, M3, was used to implement the shields. It was calculated that a grid shield of 2.5 μm grid bar width and spacing of 5 μm offered a good compromise at both providing shielding and causing a relatively small drift in circuit inductance. In order to make SFQ circuits more tolerant to magnetic fields, we have simulated with circuit parameter alterations to realise the best bias and higher operating field margins, due to external magnetic fields. The external magnetic fields are modelled through 3 orthogonal coils that generate roughly a uniform magnetic field density throughout the cell under test.

Contents

Declaration	ii
Abstract	iii
Opsomming	iv
Acknowledgments	v
Publications	vi
1 Introduction	1
1.1 Background and Motivation	1
1.1.1 Magnetic Fields Issues in SFQ Circuits	2
1.1.1.1 Susceptibility to External Magnetic Fields	2
1.1.1.2 Susceptibility to Magnetic Fields due to Bias Currents	2
1.1.1.3 Susceptibility to Magnetic Fields due to Return Currents	3
1.1.2 Large bias currents and Current Recycling	4
1.1.3 Flux Trapping	4
1.2 Magnetic Field Tolerant and Energy Efficient Circuit Designs	5
1.3 Research Aim	6
1.4 Contribution to Knowledge	6
1.5 Document Layout	6
2 Modelling of Magnetic Fields in SFQ Circuits	8
2.1 General Simulations Procedure	8
2.2 Preliminary Simulations: Delay Flip-Flop (DFF) in proximity of strip line sources	11
2.2.1 A strip line run close to the DFF - Single circuit inductor coupling	11

<i>CONTENTS</i>	ix
2.2.2 A strip line run round the DFF: Single circuit inductor coupling	12
2.2.3 A strip line run over the DFF: Single circuit inductor coupling	12
2.3 Modelling of magnetic fields using coils	13
2.3.1 A Hypres DFF Cell as a Test Circuit	14
2.3.1.1 Naming of Coils	14
2.3.2 Generation of Uniform Magnetic Fields	15
2.3.3 Simulations with the DFF under the influence of a single coil	18
2.3.4 Simulations of the DFF under the influence of 3-D Coils	18
2.4 Simulations with the DC-SFQ cell	21
2.5 Conversion from Webers (Wb) to Tesla (T)	21
2.6 Validation of coupling coefficients	23
2.6.1 Concentric Coils	23
2.6.2 Coils and Circuit Inductors	24
2.7 Chapter Conclusion	25
3 On-Chip Shielding of SFQ Circuits	26
3.1 Introduction	26
3.1.1 Shielding Background	26
3.1.2 Superconductor Material Based Shields	28
3.1.3 Factors that determine shielding effectiveness (SE)	29
3.2 Simple Superconducting Shields for Strip-lines in SFQ Circuits	29
3.3 Preliminary Analysis of New Shielding Implementations	31
3.4 Grid-patterned Shield Concept	33
3.4.1 A Comparative Analysis of the Grid and Solid Shields	34
3.5 Further Analysis of Grid Shield	36
3.5.1 Background	36
3.5.2 Effect of Grid Spacing on Shielding Effectiveness and Circuit Inductance	38
3.6 Chapter Conclusion	40

4	On-Chip Shielding Design Considerations	41
4.1	Introduction	41
4.2	Effect of ground contact positioning on shielding effectiveness	41
4.2.1	Simulations and Results	42
4.2.1.1	Grid Shield	43
4.2.1.2	Solid Shield	43
4.3	Effect of Grid Bar Spacing on Uniformly and Sporadically Grounded Shields	44
4.3.1	Uniformly grounded grid shield for a DFF	44
4.3.2	Sporadically grounded grid shield for a DFF	46
4.3.3	Shield and Ground Plane Current Distribution	47
4.3.4	Points To Consider	48
4.4	Further Shielding Analysis with Inclined Magnetic Fields in 3-D	48
4.4.1	Performance of the DFF in a rotated magnetic field	50
4.4.2	Performance of the DC-SFQ in a rotated magnetic field	50
4.5	Rotated Magnetic fields and Bias Margin Analysis	51
4.6	Chapter Conclusion	56
5	Magnetic Field Tolerant Design	57
5.1	Inductor Design	57
5.1.1	Straight Discrete Inductors	57
5.1.2	Meandered Discrete Inductors	59
5.1.3	Ring Shielded Inductors	60
5.2	Cell Layout for Improved Magnetic Field Tolerance	63
5.2.1	The DFF Cell	63
5.2.2	Layout Changes to the DFF Cell	65
5.2.3	The DC-SFQ Cell	66
5.2.4	Layout Changes to the DC-SFQ Cell	68
5.3	Design for Known Magnetic Fields	69
5.4	Moats and Magnetic Field Tolerant SFQ Circuits	72
5.5	Chapter Conclusion	73

<i>CONTENTS</i>	xi
6 Conclusions and Recommendations	74
6.1 Conclusions	74
6.2 Recommendations	75
Bibliography	75
A Additional Procedure for Magnetic Field Calculations	82
A.1 Calculation of Parameter Margins with External Magnetic Fields	82
A.2 Circuit's Failure Point	88
B Software Tools	89
B.1 <i>InductEx</i>	89
B.2 gEDA	89
B.3 Stellenbosch University (SU) Tool set	90
B.4 LASI	90

List of Figures

2.1	Josephson Transmission Line (a) schematic captured in gschem with $B1 = B2 = 250 \mu A$, $L1 = L2 = L3 = L4 = 2 pH$ and $IB1 = 350 \mu A$ and (b) layout made in LASI according to the IPHT process design rules.	9
2.2	Phase plots for the JTL simulated with two SFQ pulses (not shown).	10
2.3	Bias and parameter margins for the JTL	10
2.4	A Schematic of a 5-Junction DFF with an adjacent bias line, L_p . Parameters: $L_1 = 1.8 pH$, $L_2 = 1.8 pH$, $L_x = 6.6 pH$, $L_3 = 1.8 pH$, $L_4 = 1.2 pH$, $L_5 = 2.0 pH$, $L_6 = 1.4 pH$, $L_p = 2 pH$, $R_L = 1 \Omega$, $J_1 = 175 \mu A$, $J_2 = 200 \mu A$, $J_3 = 150 \mu A$, $J_4 = J_5 = 250 \mu A$, $Ib1 = 230 \mu A$ and $Ib2 = 135 \mu A$	11
2.5	A 5-Junction DFF with a an external inductor loop L_p around it - Laid out in IPHT $1kA/cm^2$ process	12
2.6	A 5-Junction DFF a conductor in M3 run over it - Laid out in Hypres $4.5kA/cm^2$ process	13
2.7	A 5-Josephson junction DFF shown with one coil L_{yz} . Coil coupling to DFF inductances not shown. Parameters: $L_1 = 1.86 pH$, $L_2 = 1.59 pH$, $L_3 = 7.73 pH$, $L_4 = 1.5 pH$, $L_5 = 2.13 pH$, $L_6 = 1.3 pH$, $L_7 = 1.91 pH$, $L_{yz} = 920.8 pH$ at radius $R = 125 \mu m$, $J_1 = 175 \mu A$, $J_2 = 200 \mu A$, $J_3 = 150 \mu A$, $J_4 = 200 \mu A$, $J_5 = 250 \mu A$, $Ib1 = 220 \mu A$ and $Ib2 = 135 \mu A$	14
2.8	Coils around the DFF laid out for Hypres $4.5 kA/cm^2$ process, DFF size is $100 \mu m$ by $100 \mu m$. Radii of $R = 125 \mu m$, $130 \mu m$ and $135 \mu m$ were chosen for each coil to prevent them from touching each other.	15
2.9	Magnetic flux density variation with distance (x) for (red) from the centre of a DFF for the extremes as expressed in (2), (black) for a small distance change from the centre of a DFF. In the plots $R = 125 \mu m$, $I = 5 mA$ and $\mu_o = 4\pi \times 10^{-7}$	16
2.10	A plot of $I_{max}(R)/R$ against R for the yz , xz and xy coils each with a radius $R = 125 \mu m$ around a DFF of $100 \mu m \times 100 \mu m$ size	17
2.11	Magnetic field plots of a simple SFQ circuit (strip line) with (a) a coil with radius $R = 50 \mu m$ which results in a non-uniform field distribution in its centre and (b) coil with radius $R = 125 \mu m$ confirming the homogeneity of the magnetic field at the centre. The disparity in the two figures can be judged by the colour distribution and magnetic field pattern in the centre of the coils. The SFQ circuit (strip-line) has the same dimension in both cases: $100 \mu m \times 5 \mu m$	17

2.12	A 5 junction DFF simulated with the yz -coil that generates magnetic fields in the x direction with respect to the cell	18
2.13	The resultant magnetic field in spherical coordinates	19
2.14	A magnetic field vector plot of the DFF surrounded by 3 coils that produce approximately an equal amount of magnetic field each. The resultant is a magnetic field that penetrates the DFF at an angle, as shown by the arrows inside the dashed box.	20
2.15	DFF bias and parameter margins with a current of 4.5 mA injected in each of the three coils. The distribution signifies failure of the DFF operation. At this stage, the DFF exhibits wrong switching patterns.	20
2.16	A DC-SFQ with parameters: $L_1 = 0.56$ pH, $L_2 = 0.52$ pH, $L_3 = 1.0$ pH, $L_4 = 4.78$ pH, $L_5 = 2.2$ pH, $L_6 = 4.1$ pH, $J_1 = 225$ μ A, $J_2 = 225$ μ A, $J_3 = 250$ μ A, $Ib_1 = 275$ μ A and $Ib_2 = 175$ μ A. Optimised bias margins: $-56\% \sim 34\%$	21
2.17	The DC-SFQ simulated with the yz -coil that generates magnetic fields in the x direction with respect to the cell	22
2.18	An illustration of a circular current carrying coil with an SFQ cell at its centre	22
2.19	An illustration of concentric coils, with a current I_1 flowing through the larger coil	23
2.20	A coil with a co-axis rectangular inductor in the centre. The length of the inductor extends equally in both directions towards the coil	24
3.1	A simplified view of a shield placed between Areas A and B to reduce EM interaction between the two areas.	26
3.2	Layout of three scenarios: Top: $M1$ (red) under $M3$; Middle: $M1$ and $M3$ separated by a wide shielding layer in $M2$ and at the bottom $M1$ and $M3$ separated by a shield in $M2$, grounded at both ends.	30
3.3	An equivalent circuit of the stripline shielding implementation. I_{int} is the equivalent current that causes magnetic field interference ($\Phi = L_{M3}I_{int}$). L_{M3} , L_{M2} and L_{M1} are the inductance of the respective layers. k_{31} and k_{21} are coupling coefficients as shown by the arrows.	30
3.4	The DFF covered in (a) a solid shield and (b) A grid patterned shield made with $2.5\mu m$ strips and a spacing of $5\mu m$	31
3.5	A DFF covered in (a) solid shield and (b) grid shield. The circled position indicate ground contacts. It was observed that a minimum of two contacts improved the shielding. Ideally, ground contacts should be positioned roughly in the same line axially. However, layout constrains may not accord the design such a privilege as such positions could be occupied by interface and bias lines.	32
3.6	Magnetic field images with cross-section of the DFF and a test current injected at the encircled points - no external fields. (a) unshielded DFF - cross-section, (b) with solid shielding, (c) with grid shielding. Point X was chosen arbitrarily.	33
3.7	The Grid shield showing the superconducting loop created by each aperture.	34

3.8	A cross section of a grid shield with different width of aperture - More stray field creep through wider apertures.	34
3.9	Current density plots of a DC-SFQ surrounded by 3 orthogonal coils, (a) unshielded and (b) under a standard grid shield	37
3.10	A bar graph showing the reduction of current density, due to external magnetic field, in a shielded DC-SFQ Cell, compared to the unshielded case	38
3.11	A DFF covered in a grid patterned shield - each grid bar is $2.5 \mu\text{m}$ wide and are spaced $5 \mu\text{m}$ from each other. The layout was done in the <i>Hypres'</i> $4.5 \text{ kA}/\text{cm}^2$, in which the layer, M3, with fixed thickness $d = 600 \text{ nm}$ was used to make the grid shield.	38
3.12	The variation of shielding effectiveness with changing grid spacing - A grid shield with smaller spaces offers better shielding, but the downside is that the circuit inductance are affected to the point that re-optimisation of the entire circuit might be necessary and vice-versa. Positive and negative currents refer to fields from coils.	39
3.13	Percentage inductance drop against variations in grid spacing in both the DFF and DC-SFQ	40
4.1	(a) <i>Grid1</i> grounded at 3 points only by taking advantage of the available spaces after initial layout and (b) <i>Grid2</i> with 12 ground contacts at specifically chosen positions. For <i>Grid2</i> , some circuit elements had to be moved around to accommodate the uniform ground contact placement.	42
4.2	(a) <i>Grid3</i> grounded at 4 points, one at each corner of the cell, (b) <i>Grid4</i> with 8 ground contacts at positions close to and in-line with input/output locations on the cell.	42
4.3	OFMs of a uniformly grounded DFFs against grid bar spacing for magnetic fields from the <i>xy</i> -coil, (a) from $0 \mu\text{m}$ spacing and (b) from $2.5 \mu\text{m}$ spacing.	45
4.4	OFMs of a uniformly grounded DFFs against grid bar spacing for magnetic fields from the <i>xz</i> -coil, (a) from $0 \mu\text{m}$ spacing and (b) from $2.5 \mu\text{m}$ spacing.	45
4.5	OFMs of a uniformly grounded DFFs against grid bar spacing for magnetic fields from the <i>yz</i> -coil, (a) from $0 \mu\text{m}$ spacing and (b) from $2.5 \mu\text{m}$ spacing.	45
4.6	OFMs of a sporadically grounded DFFs against grid bar spacing for magnetic fields from the <i>xy</i> -coil, (a) from $0 \mu\text{m}$ spacing and (b) from $2.5 \mu\text{m}$ spacing.	46
4.7	OFMs of a sporadically grounded DFFs against grid bar spacing for magnetic fields from the <i>xz</i> -coil, (a) from $0 \mu\text{m}$ spacing and (b) from $2.5 \mu\text{m}$ spacing.	47
4.8	OFMs of a sporadically grounded DFFs against grid bar spacing for magnetic fields from the <i>yz</i> -coil, (a) from $0 \mu\text{m}$ spacing and (b) from $2.5 \mu\text{m}$ spacing.	47
4.9	Different grid shield scenarios (a) a circuit inductor laid out under a bar for a uniform grid shield and in (b) a non-uniform grid shield created specifically to remove the inductor from under a grid bar. The effect on the shielding efficiency is very small, but the inductor's value is restored to the design value.	48
4.10	Magnetic field vectors in 3-D space corresponding to Type 1, 2 3 and 4 in Table 4.3. The other orientations are simply 180° phase shift versions of the vectors here, as follows: Type 5(is -4), Type 6(is -2), Type 7(is -3) and Type 8(is -1).	49

4.11	Analogy of the effected rotation of an external magnetic field around a fixed DFF cell. Alternatively, in experiments, the DFF can be rotated instead while keeping the field orientation fixed. The 5-Junction DFF was also used in these simulations, where IN and OUT are the DFF's input and output, respectively. The DFF is positioned as shown, i.e. vertically.	52
4.12	A simplified bias margins diagram for the DFF. The length of each line indicates the bias spread for that angle.	52
4.13	Bias margin results for the DFF with a magnetic field rotated around it, (a) unshielded, (b) grid shielded and (c) solid shielded DFFs.	54
4.14	Bias margin results for the DC-SFQ with a magnetic field rotated around it, (a) unshielded, (b) grid shielded and (c) solid shielded DC-SFQs.	55
5.1	Set 1: Three inductors of different dimensions, but equal inductance.	58
5.2	Set 2: Inductors of equal length, but different widths	58
5.3	Inductors of equal inductance but different shapes. Inductor L_S has the same dimensions as L_B of Fig. 5.2.	60
5.4	Three grounded (GND) ring configurations around the inductor L_D laid out in layer M2. A: Inductor with a ring in M1 and one ground contact, B: Inductor with a ring grounded at two locations across the Inductor and C: Inductor with a ring grounded at two locations at both ends of the inductor.	61
5.5	Magnetic field plots for the three configurations (a), (b) and (c), corresponding to A, B and C, respectively, shown in Fig 5.4, for x , y and z -directed magnetic field density	62
5.6	Two SFQ cell layouts in their formally optimised form: (a) DFF and (b) DC-SFQ	63
5.7	Directions of flow for the coupled currents in each loop according to the coupling coefficients depicted in Table 5.6. The assumed positive direction of flow is left to right.	64
5.8	Margins of the DFF, before failure that is $67 \mu\text{T}$ (or $13.4 \mu\text{A}$ through the yz -coil) for only one direction of coil current. K2, K4 and K6 are in blocks.	65
5.9	Two DFF cells, lined-up side by side. The dashed boxes show the effected changes	66
5.10	Directions of flow for the coupled currents in each loop according to the coupling coefficients depicted in Table 5.9. The assumed positive direction of flow is left to right.	67
5.11	Margins of the DFF, soon before failure that is $199 \mu\text{T}$ (or $39.6 \mu\text{A}$ through the yz -coil) for only one direction of coil current). K2 and K3 are the block.	68
5.12	Two DC-SFQ cells, lined-up side by side. The dashed boxes show the changes made. . . .	69
5.13	A 5-Josephson junction DFF with parameters: $L_1 = 1.86 \text{ pH}$, $L_2 = 1.59 \text{ pH}$, $L_3 = 7.73 \text{ pH}$, $L_4 = 1.5 \text{ pH}$, $L_5 = 2.13 \text{ pH}$, $L_6 = 1.3 \text{ pH}$, $L_7 = 1.91 \text{ pH}$, $J_1 = J_4 = 200 \mu\text{A}$, $J_2 = J_5 = 250 \mu\text{A}$, $J_3 = 150 \mu\text{A}$, $Ib_1 = 230 \mu\text{A}$ and $Ib_2 = 135 \mu\text{A}$. Optimised bias margins: $-53\% \sim 42\%$	70

5.14	A DC-SFQ with parameters: $L_1 = 0.56 \text{ pH}$, $L_2 = 0.52 \text{ pH}$, $L_3 = 1.0 \text{ pH}$, $L_4 = 4.78 \text{ pH}$, $L_5 = 2.2 \text{ pH}$, $L_6 = 4.1 \text{ pH}$, $J_1 = 225 \text{ }\mu\text{A}$, $J_2 = 225 \text{ }\mu\text{A}$, $J_3 = 250 \text{ }\mu\text{A}$, $Ib_1 = 275 \text{ }\mu\text{A}$ and $Ib_2 = 175 \text{ }\mu\text{A}$. Optimised bias margins: $-56\% \sim 34\%$	71
5.15	Margins calculated one step before failure point (OFM) for (a) DFF and (b) DC-SFQ, showing critical components (in boxes) marked for alteration.	71
5.16	Cell layouts with moats (a) DFF and (b) DC-SFQ	72
A.1	JTL schematic showing the magnetic field inductor LF1 and simulated current ILF1	83
A.2	JTL Layout made in LASI 6	83
A.3	Margins of the JTL against a y-directed magnetic field produced with a current ILF1 through Inductor LF1. The margins calculated at (a) $ILF1=0 \text{ }\mu\text{A}$, (b) $ILF1=10 \text{ }\mu\text{A}$ and $ILF1=20 \text{ }\mu\text{A}$	85
A.4	Margins of the JTL against a y-directed magnetic field produced with a current ILF1 through Inductor LF1. The margins calculated at (a) $ILF1=30 \text{ }\mu\text{A}$, (b) $ILF1=40 \text{ }\mu\text{A}$ and $ILF1=47 \text{ }\mu\text{A}$	86

List of Tables

2.1	Josephson junction switching instances. The values under B1_P and B2_P are the number of times the junction made 2π phase shifts. At time =0 the values are only for initialisation.	10
2.2	Magnetic fields produced by the 3-D coils - the total magnetic field acting on the DFF is a vector summation of the three i.e. $37.4 \mu\text{T}$	21
2.3	Comparison of analytical and extracted coupling coefficients	24
2.4	Analytical and extracted coupling coefficients between a coil and an in-plane rectangular inductor	24
3.1	k_{31} - Coupling between $M3$ and $M1$; k_{21} Coupling between $M2$ and the shield in $M1$. . .	31
3.2	Values of DFF circuit inductances in presence of grid and solid shields- regardless of coil type used	32
3.3	Comparison of failure points of the DFF for the two on-chip shields with different sources of external magnetic field. The unshielded case is shown as a reference.	35
3.4	Comparison of failure points of the DC-SFQ for the two on-chip shields with different sources of external magnetic field. The unshielded case is shown as a reference	35
4.1	OFMs for each ground type in the grid shield	43
4.2	OFMs for each ground type in the solid shield	43
4.3	Types of magnetic field orientations determined by the directions of coil currents in the xy , xz and yz coils.	49
4.4	DFF OFMs (μT) after the orientation of external magnetic fields was changed. Bold figures show improvement in OFMs compared to the unshielded case.	50
4.5	DC-SFQ OFMs (μT) after the orientation of external magnetic fields was changed. Bold figures show improvement in OFMs compared to the unshielded case.	50
5.1	Induced currents in the Inductors of Set 1	58
5.2	Induced currents in the inductors of Set 2	58
5.3	Induced currents in inductors with equal length but different widths as shown in Fig. 5.3.	60

5.4	Induced currents from different magnetic fields in the ring configurations shown in Fig. 5.4.	61
5.5	Operating field margins for the unshielded DFF	63
5.6	Coupling coefficients between the yz -coil and respective inductors L1 to L7. K2, K4 and K6 (all in bold), are, on average, higher than the rest by over 10 times.	64
5.7	New coupling coefficients between DFF circuit inductance and x -directed fields from the yz -coil	66
5.8	Operating field margins for the unshielded DC-SFQ	67
5.9	Coupling coefficients between yz -coil and respective inductors L1 to L6. K2, K3 (all in bold), are much higher than the rest, by over 10 times, on average.	67
5.10	New coupling coefficients between DC-SFQ circuit inductance and x -directed fields from the yz -coil.	69
5.11	New operating field margins (OFMs) for the DFF and DC-SFQ after selected parameters were altered. OFMs presented for positive & negative currents, respectively.	71
5.12	A comparison of between a no-moat DFF's OFMs to another with moats	72
5.13	A comparison of between a no-moat DC-SFQ's OFMs to another with moats.	72

Nomenclature

ADP2	Advanced Process 2
AIST	Advanced Industrial Science and Technology
ERSFQ	Energy-efficient Rapid Single Flux Quantum
eSFQ	Energy-efficient Single Flux Quantum
gEDA	GNU Electronic Design Automation
IPHT	Institute of Photonic Technology
IPHT	Institute of Photonic Technology
JSIM	Josephson Simulator
LASI	Layout System for Individuals
LDF	Layer Definition File
RSFQ	Rapid Single Flux Quantum
SPICE	Simulation Program with Integrated Circuit Emphasis

Chapter 1

Introduction

Rapid Single Flux Quantum (RSFQ) [1, 2] was introduced several years ago as a Josephson junction based electronics technology. Over the years, derivatives of RSFQ have surfaced and continue to uphold the prospect to offer a high speed and energy-efficient alternative to CMOS, in the long run. As a result, the technology has undergone several advancements to ensure that it is indeed efficient and ready for large scale integration. However, the technology is still affected by several challenges that include the need for large bias currents, flux trapping and vulnerability to unwanted magnetic fields from external sources and the inherently large bias currents. Of the three, the magnetic field challenge still needed to be looked into to effectively design SFQ circuits that have high immunity or tolerance to such fields.

Studies [3–6] have been made to ascertain the effect magnetic fields have on the proper operation of RSFQ circuits, especially operating margins, and have yielded possible solutions to either eliminate or reduce the effects thereof. Elsewhere, suggestions have also been made to alter the technology to reduce bias currents through current recycling [7] and reduce static power dissipation by making changes to the RSFQ technology. One unparalleled attempt has been the introduction of energy efficient SFQ (eSFQ) [8, 9] that uses Josephson junctions in bias lines instead of resistors to completely eliminate bias resistors and associated static power dissipation. The authors report that these junctions do not switch, normally, but are only required to ramp up the required bias currents. However, eSFQ and other similar variants are still susceptible to magnetic fields and they require just as much bias current as RSFQ. It is quite apparent that techniques have to be developed to prevent magnetic fields due to bias currents and external sources from affecting SFQ circuits.

1.1 Background and Motivation

Electronic circuits based on SFQ technology, such as RSFQ, have gone through several developments and most of them are becoming mature for very large scale integration (VLSI) designs. However, work remains to be done in several areas. For instance, SFQ (RSFQ, eSFQ and others) circuit design becomes challenging as the circuit complexity increases. Need for large bias currents and susceptibility to magnetic fields caused by the bias currents, ground return currents or external sources are still intricate issues and need to be addressed. Presented next are the three challenges currently facing the technology. These are categorised into three, namely: magnetic field issues in SFQ circuits, large bias currents and current recycling and flux trapping.

1.1.1 Magnetic Fields Issues in SFQ Circuits

The nature of SFQ circuits makes exclusion of all other unwanted magnetic fields requisite and yet extremely challenging. The SFQ pulse is a very small quantity, $\Phi_0 = 2.07 \times 10^{-15}$ Wb, and any larger magnetic field would compromise circuits that respond to such pulses, such as RSFQ. Therefore, it is important that circuits are designed around these issues. Magnetic fields couple to circuits and induce currents that add to existing loop currents in SFQ circuits. The additional loop or bias currents can cause operational errors and sometimes malfunction in SFQ circuits. In these circuits, the main sources of unwanted magnetic fields can be categorized as external, due to bias currents and ground return currents.

1.1.1.1 Susceptibility to External Magnetic Fields

External magnetic fields can emanate from different sources. The Earth's magnetic field, which needs to be excluded from any SFQ circuit, is significant and its density varies in magnitude around the globe. For instance, in Cape Town, South Africa, the field density, at $25 \mu T$, is large enough to cause malfunctions in SFQ circuits. The fields are higher in other parts of the world, but do not exceed $65 \mu T$ [10]. Any current carrying conductor can produce unwanted magnetic fields that can also affect SFQ circuits adversely. During experiments, Helmholtz coils were used to generate uniform magnetic fields across an RSFQ chip [6]. It was discovered that magnetic fields parallel to the plane of the chip under investigation had more effect on the operation of the RSFQ chip than those perpendicular to it. For fields parallel to the chip, the critical field (failure point) was found to be $5 \mu T$. Magnetic fields in the perpendicular direction had little effect on the chip with a critical field of $15 \mu T$. This clearly shows the vulnerability of SFQ circuits to the Earth's magnetic fields.

1.1.1.2 Susceptibility to Magnetic Fields due to Bias Currents

SFQ circuits require large bias currents to operate. The current becomes quite large with increased circuit complexity. Apart from producing heat in bias feed cables, the large currents generate strong magnetic fields that could couple to components on SFQ circuit chips. These large currents undermine most advances towards large scale integration because an entire circuit could malfunction if these currents and generated magnetic fields are not eliminated or reduced to acceptable levels. The dilemma is that increase in circuit complexity results into an increase in the required bias currents. According to *Biot-Savart* Law, the SFQ circuit will be exposed to the generated magnetic fields, due to currents from the bias line, of varying magnitudes. The magnetic fields affect the Josephson junctions and may also couple to the line inductors in the circuit. The result could be a total circuit malfunction because Josephson junctions could erroneously switch due to the additional currents introduced by the coupled magnetic fields.

The effect of bias lines on the performance of RSFQ circuits was also investigated in [5], and it was also verified in simulations that coupling occurs between bias lines and circuit inductances [4]. In addition, the authors examined the effect of mirrored currents in the ground plane [5, 11]. These currents can create a phase gradient that can lower or increase the applied current needed to cause a 2π phase leap in a Josephson junction, depending on the orientation. It was suggested that meticulous design be incorporated so that current return pads are strategically located to reduce the effects of such currents. A sky plane, which is a continuous superconducting layer used to keep out external magnetic fields, was used in the simulations and it showed to reduce coupling between bias lines and circuit inductance.

A bias line carrying 10 mA of current has a potential of producing magnetic fields that can significantly reduce the operating margins of a shift register circuit [4]. In the circuit, a complete failure occurred at a current of 20 mA . It was, however, demonstrated that the effect of magnetic fields from the bias line can be reduced if the bias line was shielded throughout or hidden under a ground plane (shielded) away from Josephson junctions and circuit inductance [3]. For this to be achieved, it is necessary that the fabrication processes be modified to accommodate several ground planes as it is in the Japanese Advanced Industrial Science and Technology's (AIST) advanced process 2 (ADP2) [12]. Nonetheless, this does not completely eliminate the effect of magnetic fields due to bias currents as these would still couple with other circuit elements, unless the ground planes are made much thicker [13]. Another concern is that layer thickness is a process dependent attribute and may not be readily available to the user, unless proper changes are made in the fabrication process. In multilayer processes, the bias lines traverse layers through vias as bias pillars. A challenge arises as the vias still allow coupling between bias lines and circuit components [14, 15]. Nonetheless, this challenge can be addressed through proper grounding around or near these bias pillars as suggested in [16].

1.1.1.3 Susceptibility to Magnetic Fields due to Return Currents

All the bias currents have to return to a superconducting ground plane and this poses a great design challenge. These currents produce magnetic fields that could couple with the RSFQ circuit at different positions [17]. The authors estimated that a ground return current of 100 mA crossing a $0.5\text{ cm} \times 0.5\text{ cm}$ chip can produce a magnetic field density of 25 μT . If enough coupling (in terms of coupling coefficient, effective area and magnetic field orientation) occurs, such a field has a potential to disrupt the operation of the RSFQ circuit, significantly. In complex RSFQ circuits, there is more than one bias point. Therefore, the creation and hence paths of the ground currents could be convoluted.

To deal with these currents, it was suggested that strategic positioning and balancing of the bias points and ground contacts would minimize the presence of these currents. Careful placement of ground bondings can reduce currents that flow in the ground plane [3]. It was established that if a return path is placed right under a bias input, magnetic fields from these lines would cancel out. However, this would require accurate circuit simulations and layout designs to make sure that both the bias and return lines carry the same amount of current. In addition, the ground plane can be removed at those points where it is not required, such as under bias lines, inductors and transmission lines. However, through simulation, it was established that cutting off the ground plane under inductors increases their inductance [18].

The overall bias current can be reduced through a technique call current recycling [7] that is used to implement serial biasing of SFQ circuits. A reduction in the bias current means less current could find its way to the ground plane. Further, the effect of the bias currents can be reduced by adding another superconducting plane (called a sky plane), above the circuit components [11, 17]. The top superconducting plane is then connected to the lower ground plane through vias. The suggested approach relies on the cancellation of the fields that are produced by the ground current through the various superconducting loops created through the vias. However, the use of the top superconducting plane needs further investigation as it may lead to flux trapping in critical circuit components, such as Josephson junctions [17]. The ground plane can be removed in areas not required, however this could increase the current density around critical Josephson junctions.

Use of upper and lower ground planes [11], increased ground plane thickness above or below bias lines [13, 19] and bias line shielding [20] are some of the developments that have been reported to address the issues of magnetic fields emanating from different sources. Such sources include bias lines and ground

return currents that can degrade circuit performance, if not dealt with. Solutions have been suggested, usually in isolation, to address specific problems, but they sometimes address issues that are specific to particular fabrication process. The number of wiring layers varies from one fabrication processes to another, even though attractive, some solutions cannot be implemented in other fabrication processes. For instance, normal shielding of bias lines can not be implemented in two-wiring layer technologies and fabrication processes.

1.1.2 Large bias currents and Current Recycling

Current recycling is the serial biasing of SFQ sub-circuits [7]. It aims at reducing the total DC bias current required to bias a larger SFQ circuit. The reduction in bias current suggests there is less current being drawn from the power supply and hence low static power consumption and weaker magnetic fields [7, 21–23] that could have a negative effect on circuit operation. Smaller currents mean less magnetic fields produced. Current recycling has over the years been touted as the best way of reducing bias currents for an RSFQ circuit. However, it is necessary that the circuits are laid out on separate ground planes and that they should have the same bias current requirements. Further, the circuits at both ends should not contribute any current to the system. Current recycling is quite promising and several investigators are looking at ways of improving and perfecting it [21].

Furthermore, for proper transfer of SFQ pulses between a driver and receiver sub-circuits, on different ground planes, it is required that the coupling be very strong. The normal vertical separation between layers makes it difficult to achieve such a strong coupling on a layout. At best, the ground planes can be made to overlap, a task that is impossible to do in fabrication processes that have one ground plane. In addition, the idea has to be modified so that sub-circuits with different bias requirements can be serially biased. Otherwise, current recycling may only be suited for circuits that require repeated cells, such as shift registers.

1.1.3 Flux Trapping

Flux trapping has been a huge concern since attempts were made to usefully apply superconductors in electronic circuits and other applications. Flux quanta can be trapped in superconducting films during cooling from room temperature to operating cryogenic temperature due, in particular, to thermal gradients and the presence of external magnetic flux [24–29]. Critical currents of Josephson junction could be altered by flux trapping as explained in [30].

Flux trapping can be reduced, but not completely eliminated, by careful placement of moats [24, 27, 28] at strategic positions on the circuits, such as around Josephson junctions and critical inductors. Moats are essentially rectangular holes that are deliberately made on a superconducting ground plane of a superconducting circuit. The idea behind moats is to have the flux migrated/trapped in them and not in circuit elements instead. Flux trapping could also be reduced through the use of multilayer, planarized fabrication processes because they prevent pinning of vortices in the ground plane [29]. The authors also report a particularly slow and controlled cooling rate of 3 mK/s that was established to significantly reduce flux trapping in Reciprocal Quantum Logic circuits (RQL). However, the reported cooling rate has to be applied with additional μ -metal shielding to exclude external magnetic fields, especially the Earth's. Even with these significant strides, there is still a limit on the number of Josephson junctions that can effectively be integrated on $5 \text{ mm} \times 5 \text{ mm}$ mm chip without suffering the effects of flux trapping. On the physical layout, moats are still the only option for the circuit designer. Several

geometries have been reported in literature [29,31], but so far, there is no established standard geometry for moats. Current progress seems to indicate that long moats are more efficient at trapping flux quanta that would otherwise affect circuits if trapped elsewhere. The effectiveness of moats for both high- T_c and low- T_c superconducting materials can be verified through the use of scanning SQUID microscope as demonstrated in [31]. Further, an analytical approach into the formation of flux vortices (trapped quantized flux) in superconducting materials and how moats can be used to trap them can be formulated following [32]. The authors also infer at completely eliminating flux trapping if the ambient magnetic field is excluded before cooling. However, this could require the use of multilayer μ -metal shields.

1.2 Magnetic Field Tolerant and Energy Efficient Circuit Designs

Attempts focused on, but were not limited to, ferromagnetic shielding, have been made before [4, 17, 20], to minimize the effect of external magnetic fields in RSFQ circuits. These include the use of a top superconducting layer called a sky plane to keep out any field from above the circuit and by laying out shielded bias lines. The latter reduces emissions from the bias lines significantly, but magnetic fields could still escape near the holes where bias current is fed to every cell. Researchers in Japan have implemented a superconducting shield [33], whereby the bias lines or entire circuits are almost completely shielded. However, to address issues due to unwanted magnetic fields affecting SFQ circuits, there is a need for a comprehensive approach that aids analysis of the magnetic field patterns from different sources, shows how the evident behaviour of the fields can be addressed across fabrication processes and deals with bias currents and their effects.

Shielding is normally achieved by using the topmost layer to envelop almost the entire circuit [20, 33]. The challenge is that such type of shielding causes circuit inductors to drop in value and the circuit needs to be redesigned and re-optimized. In addition, with a such shield in place, moats designed to prevent flux trapping become irrelevant and yet the flux trapping problem still persists. An alternative approach to shielding has been proposed, whereby the same superconducting wiring layers are laid out around SFQ circuits, grounded or not [34]. The shielding effectiveness is quite evident and circuit inductance is not affected. However, the proposed method could interfere with the routing of interface and biasing lines.

Research on SFQ based electronics has accelerated of the years, however, a lot still needs to be done for the technology to mature, as inferred in [35]. Suggested solutions to deal with magnetic fields have been isolated and most reported work has concentrated on small scale circuits. Stray magnetic fields continue to negatively affect SFQ circuits. In addition, issues of large bias currents and flux trapping are yet to be dealt with to the fullest. To properly address the problems of magnetic fields in SFQ circuits, a better understanding of these fields in SFQ circuits is required.

The attractiveness of SFQ based circuits lies in high operating speeds and comparatively much lower energy consumption to existing technologies, such as CMOS. However, as indicated in preceding sections the technology suffers from the need for large bias currents and high static power consumption in bias resistors. Attempts have been made to reduce the bias currents and also remove the resistors in the bias lines completely. However, only current recycling has shown to reduce the required bias currents in SFQ circuits. Energy-efficient circuits, such as LR-biased circuits [36–38], Reciprocal Quantum Logic [39], ERSFQ [40] and eSFQ [9] have been proposed and demonstrated. Of these, ERSFQ and eSFQ hold the most promise, in which the bias resistors are replaced by Josephson junctions to limit the bias current

being fed to gates [8, 9, 40]. ERSFQ is characterized by bias current feeding JTLs and large averaging inductance, eSFQ on the other, hand uses smaller inductance and eliminates the need for feeding JTLs. It is impossible to ignore the tremendous potential that eSFQ has in achieving the ultimate energy-efficient regimes for digital superconductive circuits. An eDFF and eTFF [41] and shifts register were successfully designed and tested for eSFQ technology. It has also been noted that both ERSFQ and eSFQ do not reduce the total bias requirement of SFQ circuits but rather seek to eliminate static power losses in the bias approaches. [32].

Magnetic field tolerant design of SFQ circuits could be dictated by several issues. These include layout design of specific circuit elements to limit coupling and hence increase a circuit's immunity to external magnetic fields, lowering or increasing parameters to increase to decrease loop currents to counter the effect of resultant coupled currents. Such layout designs could also be used to determine a circuit's vulnerability towards specific magnetic field orientations. Thereafter, specific layout changes could be made against the magnetic field orientations.

1.3 Research Aim

Against the background of the challenges the SFQ technology currently faces, work reported here sought to develop effective on-chip magnetic field shielding mechanisms for SFQ based electronic circuits and to propose circuit design approaches that increase a circuit's immunity to unwanted magnetic fields. The objective is split into three elements. Firstly, to develop simulation models for analysing magnetic field patterns and methods that could be used to generate uniform magnetic fields on SFQ cells. Secondly, to design on-chip magnetic shields for these circuits. Lastly, to consolidate solutions and techniques that can enhance magnetic field tolerance of SFQ circuits before shielding is incorporated. The developed solutions are meant to address these challenges across most SFQ based electronics technologies. Gates and interface circuits were used in simulating the various aspects of designs presented in this document. It is envisaged that this work will provide a design benchmark towards magnetic field tolerant SFQ circuits.

1.4 Contribution to Knowledge

This work presents a novel way of simulating and analysing magnetic fields in SFQ based digital circuits for purposes of designing and incorporating the best possible shielding mechanisms on-chip. In addition, a new shielding approach is suggested and analysed using magnetic fields of varying magnitudes and orientation. Lastly, layout designs that improve a circuit's magnetic field immunity have been suggested.

1.5 Document Layout

The thesis document has six chapters. In Chapter 2, a method of analysing and modelling magnetic fields in SFQ circuits is presented. The proposed shielding approaches that can be implemented with SFQ circuits to make them more tolerant to magnetic fields are presented in Chapter 3. Chapter 4 contains a presentation of on-chip shielding design considerations that could be followed when designing SFQ circuit shields. Also presented in Chapter 4 is an in-depth analysis of circuit's vulnerability to various orientations of magnetic field. In Chapter 5, various magnetic field tolerant layout designs are

presented with comprehensive performance analyses against multi-oriented magnetic fields. Conclusions and recommendations are presented in Chapter 6.

Chapter 2

Modelling of Magnetic Fields in SFQ Circuits

The concept of modelling magnetic fields for purposes of design and analysis of SFQ circuits is a vast and quite convoluted exercise. Firstly, superconducting circuits are highly vulnerable to very low magnetic fields. Therefore, simulation and test fields need to be of very small magnitudes. Secondly, during simulations, a perfect external virtual magnetic field generator is required to analyse superconductive circuits, on-chip. Therefore, a method that generates uniform magnetic fields, even minute ones, is vital for on-chip magnetic field analyses. In this chapter, a background to the analysis is given through simulations and thereafter a method of generating almost uniform magnetic fields on chip through the use of virtual coils is presented. Thereafter a validation of the coil method is presented along with a comparison of analytically obtained coupling coefficients to those calculated by *InductEx* [42–44].

In order to design effective solutions towards the magnetic field problem in SFQ circuits, several simulations were conducted. Specifically, the simulations were conducted to establish the following: how magnetic fields from different sources couple to SFQ circuits; which areas on the specific SFQ circuits are most affected by magnetic fields; which orientation of a magnetic field has the most effect on SFQ circuits; how strip lines can be modelled to produce uniform magnetic fields to act as external sources of magnetic fields and how SFQ circuits are affected by fields from all three orthogonal directions.

2.1 General Simulations Procedure

Firstly, a consideration was given to magnetic fields that can emanate from current carrying strip lines, such as bias lines. Secondly, effects of external magnetic fields on SFQ circuits were investigated. The following tools were used throughout the work presented in this document: GNU's Electronic Design Automation (gEDA) [45] for schematic capturing and netlisting, Josephson Simulator (JSIM) [46] and its derivatives for circuit simulations, Layout System for Individuals (LASI) [47] for making layouts and *InductEx* for inductance extraction (self and mutual) and modelling of coil constructs for the simulated generation of external magnetic fields. MATLAB [48] and *GNUplot* [49] were used for generating plots. Other visualisation tools that are bundled together with *InductEx*, such as *idensity* and *Magix*, were used for on-chip current density and magnetic field plotting, respectively. Files generated by these visualisation tools are viewable in open source tools, such as *Paraview* [50].

The work presented throughout this document follows a procedure that is streamlined and easy to follow. The circuits used throughout this work were simulated before and have well established parameter and

bias margins [51]. The schematics were further captured and changes, if any, made in gEDA's **gschem** before simulations. The following is a brief methodology for analysis that has been used throughout this work. In this case, a Josephson transmission line (JTL) has been used as an example. The JTL's schematic, captured in **gschem** and file created as **jt1.sch**, is shown in Fig. 2.1(a) and its layout, made in LASI, shown in Fig. 2.1(b).

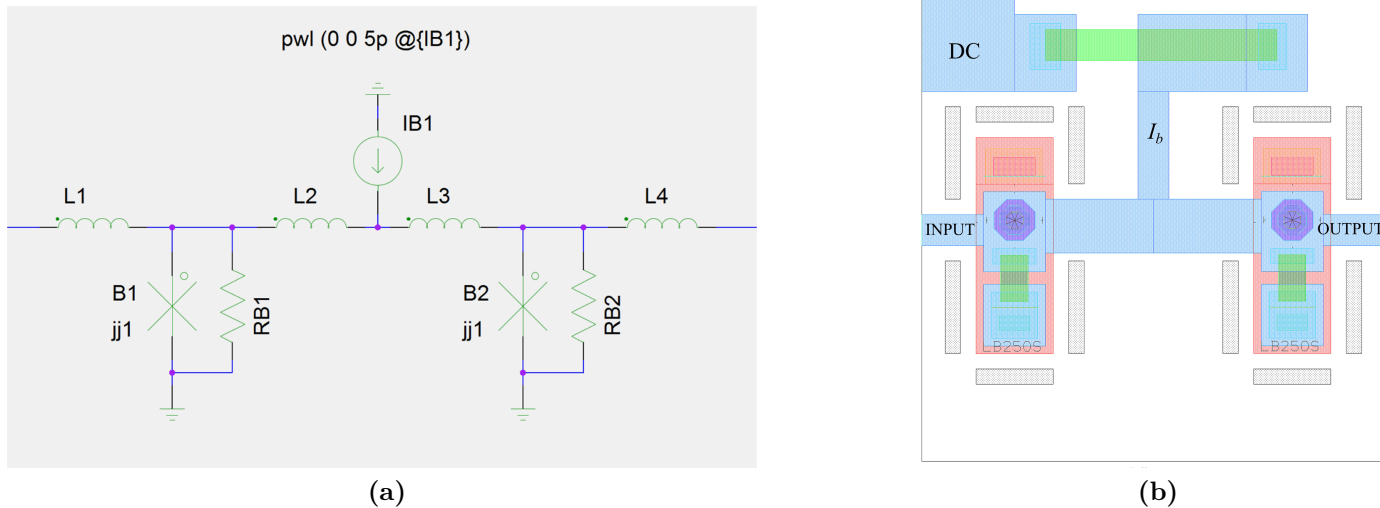


Figure 2.1: Josephson Transmission Line (a) schematic captured in **gschem** with $B1 = B2 = 250 \mu A$, $L1 = L2 = L3 = L4 = 2 pH$ and $IB1 = 350 \mu A$ and (b) layout made in LASI according to the IPHT process design rules.

To simulate the JTL with JSIM, a netlist is generated with the netlister, **gnetlist**, available and packaged with gEDA. The following command:

```
>gnetlist -g spice-sdb -o jsim -0 -v -o jt1.js jt1.sch
```

is used to generate a SPICE netlist as either **.js** or **.cir** from the schematic file, **jt1.sch**. At this stage, the netlist needs to be manually verified to ensure that all circuit elements are included as intended. A detailed description of the commands and associated parameters is available in [52].

A population file is manually created. It contains all the parameters with their nominal values, parameters that need to be varied for margin and yield analysis simulations, calculations of secondary variables, such as shunt resistance for Josephson junctions and a declaration for the number of runs for both margin and yield analyses. The SPICE netlist can include parameters that have no fixed values in the schematic, for such stages as margin analysis. However, JSIM cannot use these for transient simulations as it needs numerical parameter values. The parameters in **jt1.js** can be fixed using the nominal values in the population file by using the following command:

```
>apply jt1.js jt1.pop jt1-t.js
```

The schematic file **jt1-t.js** contains fixed nominal parameter values only. At this stage, **jsim** is executed to perform transient simulations as follows:

```
>jsim_n -m jt1.dat jt1.js
```

which produces a data file, **jt1.dat**, that can be used to make plots with either MATLAB or *GNUplot*. If noise sources were added at the time **apply** was executed, then **jsim_n** is appropriate at this stage. **jsim_n** is a modified version of JSIM that accepts circuit files that include virtual noises sources. Plots for the JTL's switching phase transitions are shown in Fig. 2.2.

In order to get operating margins a program called **analyse** is executed by the following command

```
>analyse -ma jtl.js jtl.sp jtl.pop
```

where the `jtl.sp`, shown in Table 2.1, is a text file that contains Josephson junction switching instances at the nominal operating point. They are indicated as the number of times the junction switches as multiples of 2π phase shift. These values are obtained from the JTL's phase plots shown in Fig. 2.2 at the specific simulation times shown in Table 2.1. When the parameters in `jtl.js` are varied according to the specifications in `jtl.pop`, the junction switching instances are compared to the ones defined in the `jtl.sp` file. A sample of the JTL's calculated margins is shown in Fig. 2.3. Most of the components have very wide margins, a typical occurrence in simple circuits, such as the JTL. However, it is good practice to pick the narrowest margins as the overall parameter or bias current margins (or simply bias margins). Therefore, the JTL has a bias margin of $-85.8\% \sim 73.8\%$, as observed from Fig. 2.3.

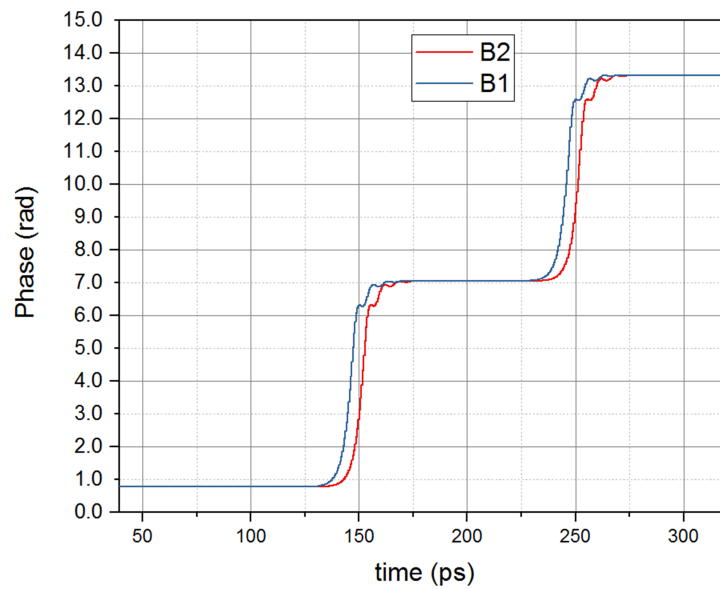


Figure 2.2: Phase plots for the JTL simulated with two SFQ pulses (not shown).

time(ps)	B1_P	B2_P
0	2	2
100	0	0
200	1	1
300	2	2

Table 2.1: Josephson junction switching instances. The values under B1_P and B2_P are the number of times the junction made 2π phase shifts. At time =0 the values are only for initialisation.

B1	[..=====]	=====	-85.8,	83.0
B2	[..=====]	=====	-85.8,	83.0
IB1	[..=====]	=====	-85.8,	73.8
L1	[=====]	=====	-90.0,	90.0
L2	[=====]	=====	-90.0,	90.0
L3	[=====]	=====	-90.0,	90.0
L4	[=====]	=====	-90.0,	90.0

Figure 2.3: Bias and parameter margins for the JTL

The addition of any other circuit parameter, such as external conductors or coils, requires modification in the circuit layout and hence the circuit files. Furthermore, these additional parameters have to be taken into account at each stage in the simulation process. Specific additional stages in the simulation chain are explained later at each particular stage and also in Appendix A. Some of the tools presented here, such as *apply* and *analyse*, are unique to the Stellenbosch University toolchain introduced and reported in [52].

D-Flip Flop (DFF) and Direct Current to SFQ (DC-SFQ) were cells of choice in the simulations presented here due to their relative simplicity and wide usage in SFQ circuits. These cells were laid out for both the Institute of Photonic Technology's (IPHT) $1kA/cm^2$ and Hypres' $4.5kA/cm^2$ processes [51, 53, 54]. The former was only applicable in the initial analysis because it has only two wiring layers. This shortcoming is further explored in the forthcoming sections. However, it is known that other researchers have been working on the implementation of shielding solutions with the IPHT process [34].

2.2 Preliminary Simulations: Delay Flip-Flop (DFF) in proximity of strip line sources

The aim of the simulations presented in this section was to establish how very low magnetic fields from external sources or bias lines can affect SFQ based circuits. Coupling was assumed to occur between the field producing conductor and one inductor in the DFF circuit. This assumption was made to emphasize that even a small external field in a localised area has the potential to affect circuit operation. Three configurations were considered and are presented next [55]¹.

2.2.1 A strip line run close to the DFF - Single circuit inductor coupling

A 5-junction RSFQ DFF, designed and laid out for the Institute of Photonic Technology (IPHT) $1kA/cm^2$ process [56], was used to ascertain the effect an imaginary current carrying inductor, $L_p = 2pH$ shown in Fig. 2.4, can have on all the inductors on the gate. With only inductor L_x considered, it was observed that with a coupling coefficient $k = 0.4$, and a current of $I_p = 450\mu A$, margins for L_x , shifted from an initial $-44\% \sim 64\%$ to $-63\% \sim 2.1\%$. Only inductor L_x was chosen at this point because it is the most critical inductor in the DFF as observed through simulations. The overall critical margins on the junctions shifted from $-29\% \sim 40\%$ to $-15\% \sim 3.5\%$. At $I_p = 500\mu A$ through L_p , there was enough coupling, with $L_x = 6.6pH$ to cause complete malfunction in the circuit. The DFF margins shrunk quicker if either the coupling k_{px} between L_p and L_x or I_p were increased. A current of $I_p = 500\mu A$ creates a critical field of $\Phi_c = L_p I_p = 2.8fWb$.

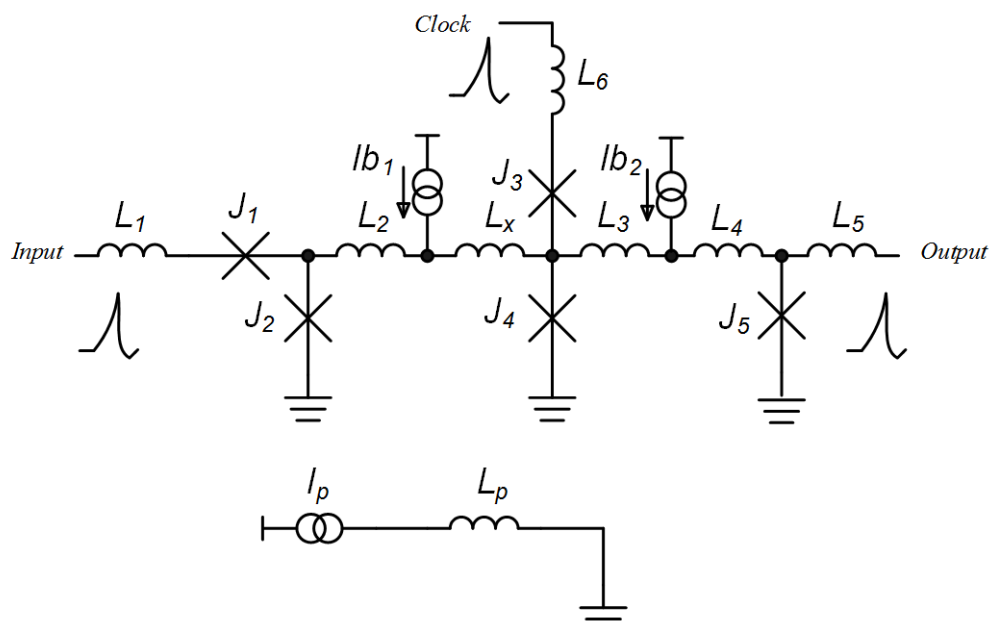


Figure 2.4: A Schematic of a 5-Junction DFF with an adjacent bias line, L_p . Parameters: $L_1 = 1.8pH$, $L_2 = 1.8pH$, $L_x = 6.6pH$, $L_3 = 1.8pH$, $L_4 = 1.2pH$, $L_5 = 2.0pH$, $L_6 = 1.4pH$, $L_p = 2pH$, $R_L = 1\Omega$, $J_1 = 175\mu A$, $J_2 = 200\mu A$, $J_3 = 150\mu A$, $J_4 = J_5 = 250\mu A$, $Ib1 = 230\mu A$ and $Ib2 = 135\mu A$.

¹Material presented in this section is part of already published work by the author [55].

2.2.2 A strip line run round the DFF: Single circuit inductor coupling

To investigate the same effect in Section 2.2.1, a layout of the DFF was done in LASI [47] for the IPHT 1 kA/cm^2 process, as shown in Fig. 2.5. Thereafter mutual inductances between circuit elements and an external inductor loop were extracted with *InductEx*. The calculated coupling coefficients were significantly lower because the external loop could not be brought any closer to the DFF gate, without violating process design rules. The coupling coefficient obtained between L_p and L_x was 0.0047, sufficient to cause a significant shift in operating margins depending on the amount of current flowing in L_p . Through the calculation of mutual inductance with *InductEx* and transient analysis in JSIM and margin analysis, it was established that the circuit had a critical field produced by L_p of $\Phi_c = 742.2\text{ fWb}$ that represents $I(L_p) = 1.7\text{ mA}$ flowing through the external inductor loop. At this stage, the simulations were done considering the coupling between L_p and all the inductors in the DFF. This is a more realistic approach unlike the simplified approach depicted in Section 2.2.1, suffice to say both indicate the effect of external magnetic fields on SFQ circuits.

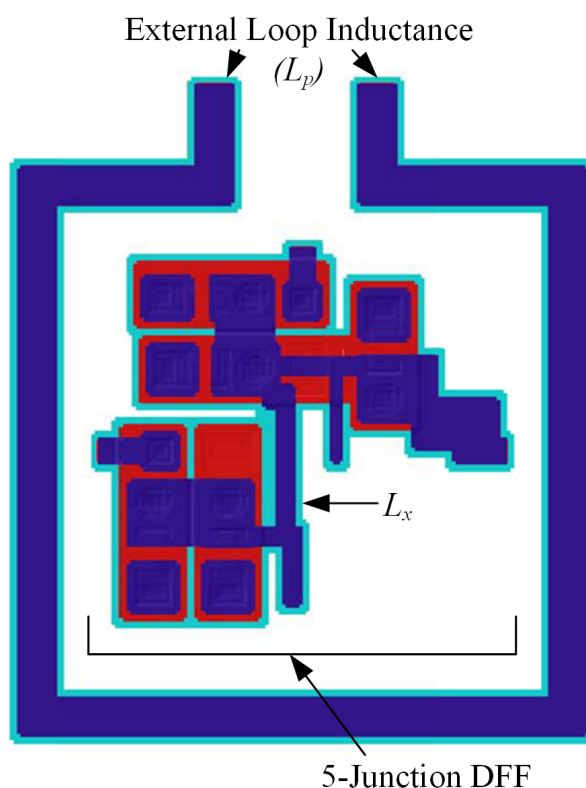


Figure 2.5: A 5-Junction DFF with an external inductor loop L_p around it - Laid out in IPHT 1 kA/cm^2 process

2.2.3 A strip line run over the DFF: Single circuit inductor coupling

The effect of running bias lines over an RSFQ circuit was also investigated with a DFF, designed and laid out for the *Hypres'* 4.5 kA/cm^2 fabrication process [54]. The aim was to simulate the effect a current carrying conductor laid out in an upper or lower layer would have on an SFQ cell. This fabrication process was more suited for this exercise because it has three wiring layers: $M1$, $M2$ and $M3$. The third layer ($M3$) was used as the virtual external current carrying line while the other two layers, $M1$ and $M2$, were primarily used for wiring and making Josephson junctions. The final layout of the DFF with an external current line, in $M3$, is shown in Fig. 2.6.

With a virtual bias line L_o (in $M3$) running over the DFF, the coupling to the inductor L_x was $k_{ox} = 0.13$. This coupling was sufficient to cause a shift in operating margins or cause malfunction depending on

the amount of current flowing through L_o . It was established that operating margins narrowed to a point of malfunction at $I(L_o) = 175 \mu A$ representing a critical field of $\Phi_c = 3.3 fWb$. Therefore, it is good design practice to avoid running bias lines or any current carrying layers over SFQ circuits, unless separate layers are available to act as shields. Large coupling, as high as 0.5 occurs between in-cell bias lines and circuit inductance. However, this is insignificant as the current through in-cell bias lines are usually small. The coupling between the current line L_x and the DFF inductor varies as L_x is swept across the DFF. It clearly shows that the location of a current carrying line with respect to critical circuit components has a huge bearing on overall circuit performance. In practice, magnetic field sources may not be positioned as close the DFF as depicted here, but they could still produce damaging magnetic fields to SFQ circuits.

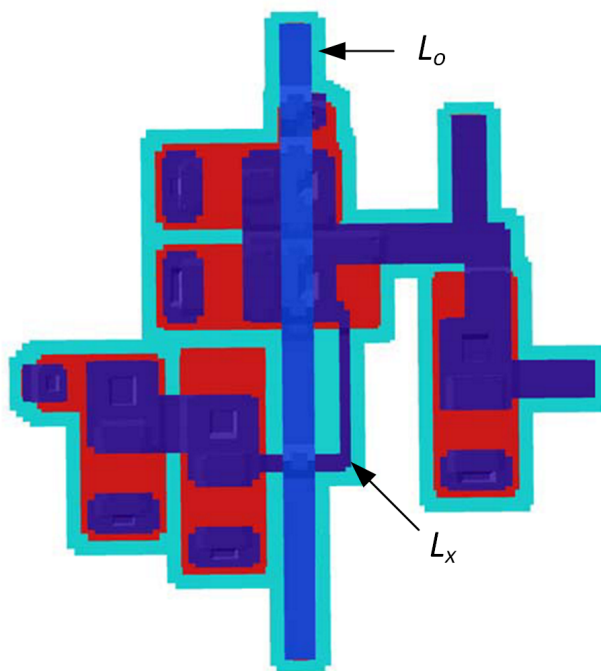


Figure 2.6: A 5-Junction DFF a conductor in M3 run over it - Laid out in Hypres $4.5kA/cm^2$ process

The three scenarios presented in this section and in Sections 2.2.1 and 2.2.2, serve the purpose of revealing how magnetic fields in small quantities can affect SFQ circuit operation and looks at instances where the external fields are generated by bias lines nearby. However, the magnetic field does not segregate, in terms of coupling to circuit elements. Therefore, all circuit inductance need to be used in a more practical analysis. If the field is produced by a relatively distant entity, It is accurate to represent the magnetic field on the surface of the SFQ circuit as uniform. Such a field cannot be estimated using the strip lines presented so far. To address this, arbitrary strip lines in the form of coils, that can deliver uniform magnetic fields are presented next.

2.3 Modelling of magnetic fields using coils

The simulation procedure discussed in Section 2.1 was extended to an automated approach for better and faster calculation of margins and failure points. The additional procedure is explained in detail in Appendix A and it enables the calculation of margins and failure points of SFQ cells in external magnetic fields. The discussion also includes MATLAB scripts that were used to automate the processes.

In most known experiments, external magnetic fields can be produced and projected onto a test circuit buy using a coil energised by either AC or DC current or through the use of Helmholtz coils as in [6].

However, the process becomes rather challenging when the magnetic field has to be projected on-chip. A system of coils is hereby introduced, that had been verified to produce uniform magnetic fields onto an SFQ cell. A DFF was used as a test cell with the coils in all three orthogonal directions, one coil at a time.

2.3.1 A Hypres DFF Cell as a Test Circuit

In this case, the DFF layout was made in accordance with the *Hypres*' $4.5kA/cm^2$ process design rules [54]. As indicated earlier, the process has 3 wiring layers : $M1$, $M2$, and $M3$. The DFF circuit, shown in Fig. 2.7, was first simulated and optimised without any external magnetic field (i.e. No external coil constructs) to determine the best working parameters and margins. The optimised DFF was used at each stage in the simulations. Initial optimized parameters are indicated in Fig. 2.7 in the absence of external magnetic fields and correspond to bias margins of $-59\% \sim 40\%$.

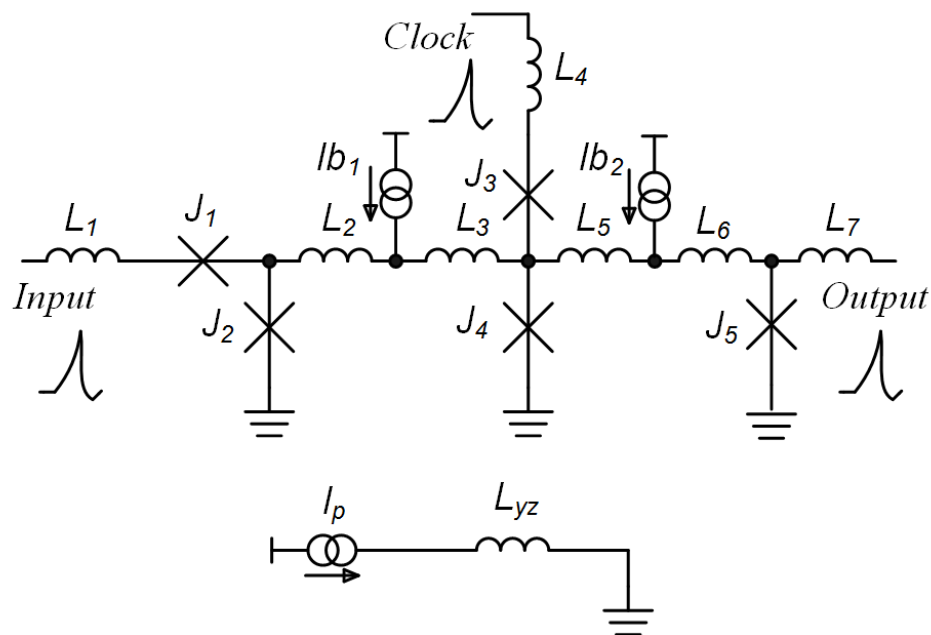


Figure 2.7: A 5-Josephson junction DFF shown with one coil L_{yz} . Coil coupling to DFF inductances not shown. Parameters: $L_1 = 1.86$ pH, $L_2 = 1.59$ pH, $L_3 = 7.73$ pH, $L_4 = 1.5$ pH, $L_5 = 2.13$ pH, $L_6 = 1.3$ pH, $L_7 = 1.91$ pH, $L_{yz} = 920.8$ pH at radius $R = 125$ μm , $J_1 = 175$ μA , $J_2 = 200$ μA , $J_3 = 150$ μA , $J_4 = 200$ μA , $J_5 = 250$ μA , $I_{b1} = 220$ μA and $I_{b2} = 135$ μA .

2.3.1.1 Naming of Coils

The coils are named from the conventional equation of a circle. A circle that extends into two axes, x and y with radius r , has a circle equation of $r^2 = x^2 + y^2$. Therefore, a circular coil created in the same axes is hereby named xy -coil. The other two coils are named in a same manner, such that the coil in the y and z axes is called the yz -coil and the one in the x and z , the xz -coil. The xy -coil produces magnetic fields that are perpendicular to the plane of the cell in Fig. 2.8, while the yz produces parallel fields in the x plane. The xz -coil produces fields that are also parallel to the plane of the cell, but in the y orientation.

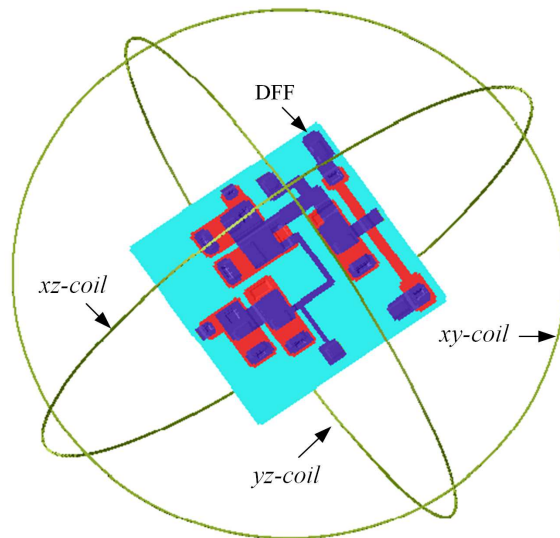


Figure 2.8: Coils around the DFF laid out for Hypres 4.5 kA/cm^2 process, DFF size is $100 \mu\text{m}$ by $100 \mu\text{m}$. Radii of $R = 125 \mu\text{m}$, $130 \mu\text{m}$ and $135 \mu\text{m}$ were chosen for each coil to prevent them from touching each other.

2.3.2 Generation of Uniform Magnetic Fields

On a cell layout, it is not straight forward to generate and simulate a uniform magnetic field across the entire cell through the use of strip lines. The *Biot – Savart* Law (2.1) shows that the magnetic field weakens as the radius or distance away from the magnetic field source increases. A system of circular strip lines or coils was considered and adopted. The coil system was developed and incorporated in *InductEx*. Within *InductEx*, circular structures called coil constructs were created to generate a fairly uniform field on the entire cell area. The coils can be simulated in the orientations described in Section 2.3.1.1.

A system of three orthogonal coils, that do not appear on the physical layout nor in the final fabrication plots, was used to generate an external magnetic field on the DFF cell. In *InductEx*, the coils can be modelled with current injection ports, finite radius and segment size. Like any current carrying strip line, as described in the previous sections, a current flowing in the coil produces a magnetic field that could couple to and hence affect the DFF circuit (the coils are depicted in Fig. 2.8).

With the coil system, the cell in the centre of the coil is assumed to be a point. However, an SFQ cell occupies a defined area and that has to be taken into consideration. In any case, the magnetic field cannot remain uniform across the cell. An approximation is necessary to ensure a uniform distribution of magnetic fields. Accordingly, a relationship between the coil radius and cell dimensions was deemed instrumental. A specific minimum coil radius with respect to cell dimensions can produce a uniform magnetic field across the entire cell being simulated. The following is a derivation towards establishing such a radius [57, 58]².

The flux density B_0 at the centre of a coil can be solved from the *Biot Savart* Law as:

$$B_0(x = 0, y = 0, z) = \frac{\mu_o I R^2}{2(R^2 + z^2)^{\frac{3}{2}}} = \frac{\mu_o I}{2R} \quad (2.1)$$

where R is the coil radius, I is the amount of current through the coil, and z is the position from the centre in the z – axis. R and I determine the amount of flux density experienced by the circuit. The DFF is located at position $z = 0$, where the magnetic field experienced is at maximum according to (2.1).

²Material presented in this section is part of already published work by the author [58]

To ensure that the magnetic field is fairly constant on all the elements of the DFF circuit, a detailed analysis was carried out. In practice, the magnetic field varies along the coil axis and also radially from its value at the centre of the coil. The axial field, created by the yz -coil for instance, varies with the distance x from the centre according to

$$B(x) = B_0 \left(1 + \left(\frac{x}{R} \right)^2 \right)^{-3/2} \approx B_0 \left(1 - \frac{3}{2} \left(\frac{x}{R} \right)^2 \right) \quad (2.2)$$

for $x \ll R$. Though several (I, R) combinations of constant ratio I/R generate the same flux density at the centre of the coil according to (2.1), all do not lead to a satisfactory flux density uniformity over the size of the chip. This is depicted in the red plot in Fig. 2.9 that shows the plot of (2.2). Only (I, R) couples for which R is sufficiently high with respect to x , allow to neglect the spatial variations of the flux density (see (2.2)), as depicted in the black plot Fig. 2.9. The variations in magnetic field density are insignificant for $x \ll R$.

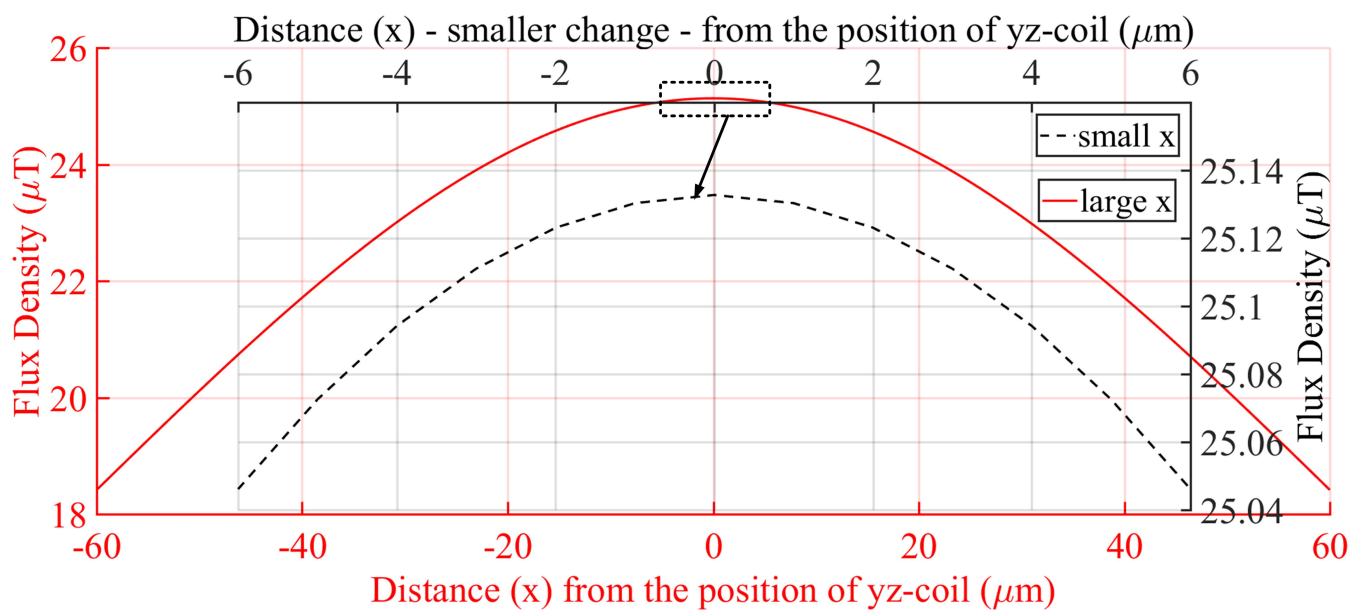


Figure 2.9: Magnetic flux density variation with distance (x) for (red) from the centre of a DFF for the extremes as expressed in (2), (black) for a small distance change from the centre of a DFF. In the plots $R = 125 \mu\text{m}$, $I = 5 \text{ mA}$ and $\mu_o = 4\pi \times 10^{-7}$.

Ideally the coils should have a very large radius in comparison with the chip size. A compromise to optimize computing power and speed of the 3-D simulations was found by gradually increasing the current I through the coil until the DFF test circuit failed, for several radii R ranging from $75 \mu\text{m}$ to $150 \mu\text{m}$. The failure point was determined by monitoring margins of the DFF cell until they reached 0%, for each coil radius: the corresponding maximum acceptable current is $I_{\text{max}}(R)$. The simulation results for yz -coil are shown in Fig. 2.10. The $I_{\text{max}}(R)/R$ begins to stabilize above $R = 120 \mu\text{m}$. This means that the DFF circuit under test is exposed to mostly the same magnetic flux density conditions over its area when the coil radius is higher than $R = 120 \mu\text{m}$, corresponding to the same homogeneous field. The results are confirmed with magnetic field plots in Fig. 2.11, in which (a) is a plot for a coil radius is $R = 50 \mu\text{m}$ and (b) with coil radius of $R = 125 \mu\text{m}$. From the colour plot, the colour and hence the strength of the field is non-uniform in Fig. 2.11(a) across the SFQ circuit. Upon a much closer inspection, the strip line representing a SFQ circuit in Fig. 2.11 can be seen to interfere with field lines in both cases, because of the presence of a solid ground plane. However, magnetic field uniformity, at the centre of the coil, is evident in Fig. 2.11(b), represented by the colour of the arrows. This confirms the results obtained before, that the coil radius needs to be large enough, to get uniform magnetic fields on the cell.

The other xy - and xz -coils showed similar results, but it took slightly larger coil radii for stability to be attained (Fig 2.10). This can be attributed to cell orientation in reference to the xy and xz coils. These two coils have less effect on the DFF as depicted by high $I_{\max}(R)/R$ values in Fig. 2.10, as the fails at higher magnetic field densities.

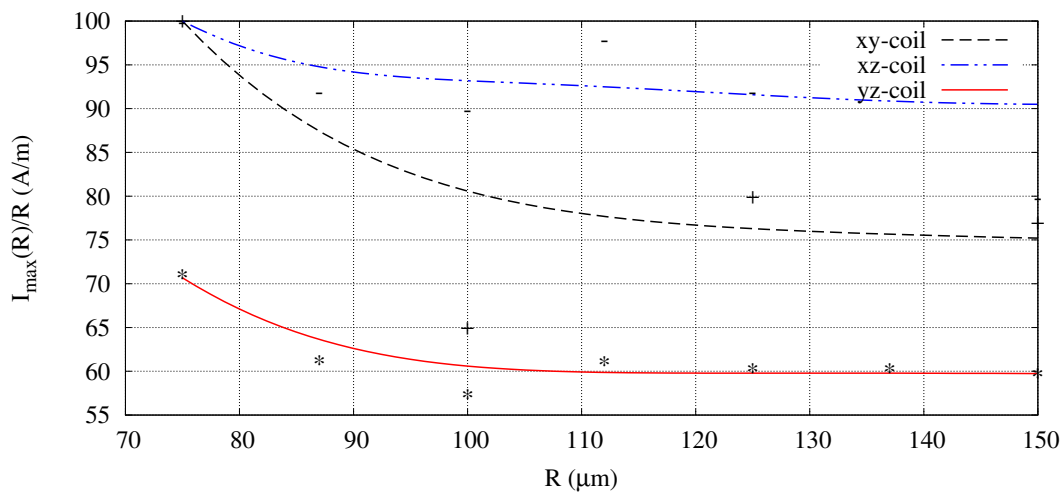
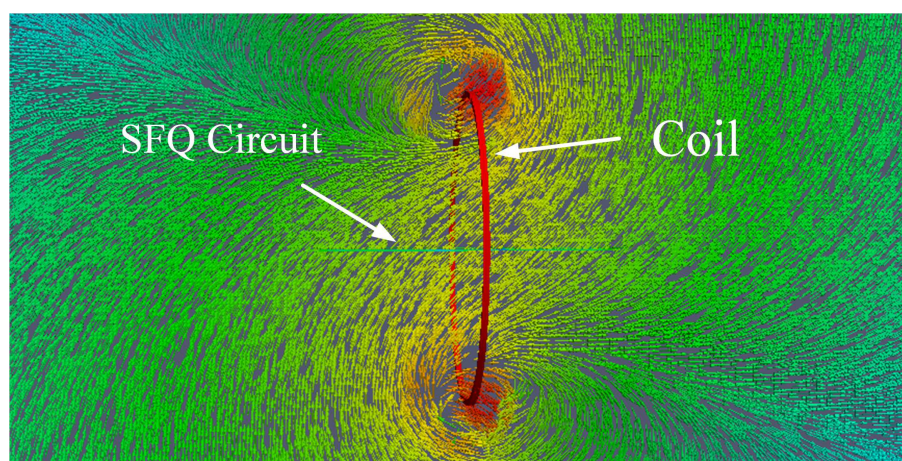
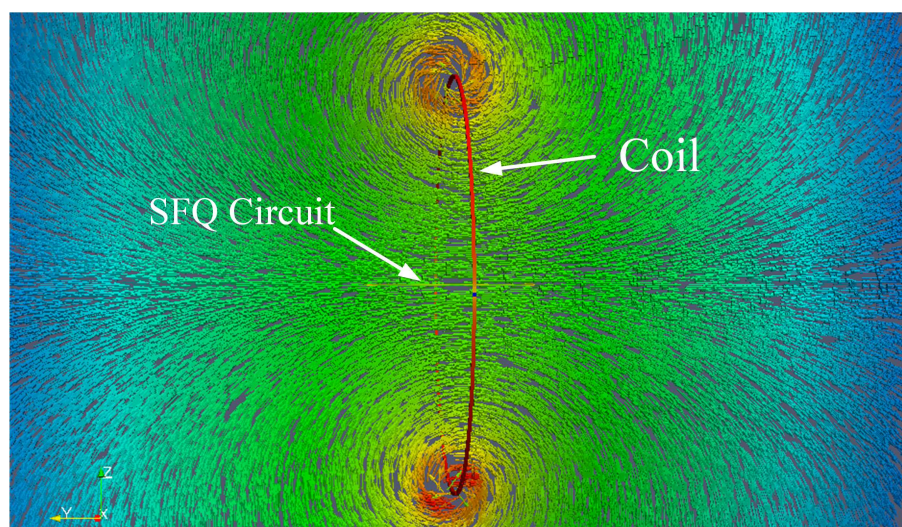


Figure 2.10: A plot of $I_{\max}(R)/R$ against R for the yz , xz and xy coils each with a radius $R = 125 \mu\text{m}$ around a DFF of $100 \mu\text{m} \times 100 \mu\text{m}$ size



(a)



(b)

Figure 2.11: Magnetic field plots of a simple SFQ circuit (strip line) with (a) a coil with radius $R = 50 \mu\text{m}$ which results in a non-uniform field distribution in its centre and (b) coil with radius $R = 125 \mu\text{m}$ confirming the homogeneity of the magnetic field at the centre. The disparity in the two figures can be judged by the colour distribution and magnetic field pattern in the centre of the coils. The SFQ circuit (strip-line) has the same dimension in both cases: $100 \mu\text{m} \times 5 \mu\text{m}$.

2.3.3 Simulations with the DFF under the influence of a single coil

A layout for these simulations, depicted in Fig. 2.12, shows the DFF layout with a coil in the yz orientation. With a current $I_{yz} \approx 12.9 \text{ mA}$ in the yz -coil of radius $R=125 \mu\text{m}$ and inductance $L_{yz} = 920.8 \text{ pH}$, used to couple the magnetic field to the inductors in the JSIM transient simulation model, the magnetic field at the centre of the coil is $65 \mu\text{T}$, to simulate the maximum magnetic field of the Earth. The magnetic field at the centre of the coil is calculated using (2.1). At an external field interference of $65 \mu\text{T}$, the bias margins dropped to $-48.5\% \sim 14.1\%$. For the yz -coil orientation, the produced magnetic field is parallel to the DFF gate. Parallel fields are more detrimental to the operation of SFQ circuits than perpendicular ones [6]. The DFF completely malfunctions at $I_{yz} \approx 13.5 \text{ mA}$ ($68 \mu\text{T}$).

Nevertheless, the DFF can be re-optimized to work in an ambient field of $68 \mu\text{T}$ by reducing bias current I_{b1} to $100 \mu\text{A}$ and increasing the value of inductances, such as L_3 . This approach works because it is understood that the external magnetic field inductively contributes to an extra biasing current, thereby causing the DFF circuit to fail, among other factors. By making the inherent parameters, such as L_3 , stiffer to this additional biasing, circuit operation can be restored with reasonable working margins. However, this only works if the magnetic field is oriented along the x -axis in the same direction as that used in the simulations. Therefore, margin optimization, at a known magnetic field, requires that circuits be placed in a specific orientation.

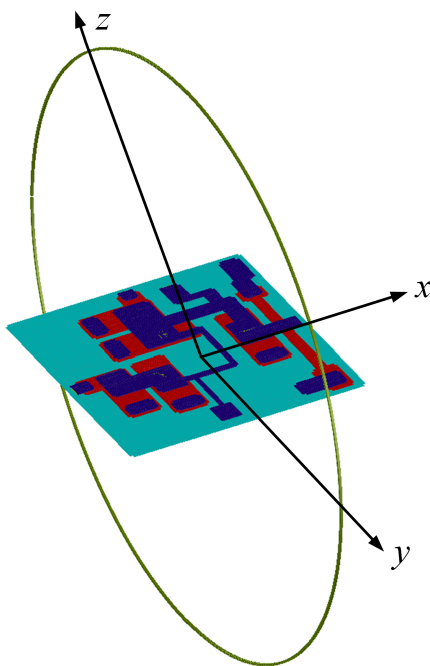


Figure 2.12: A 5 junction DFF simulated with the yz -coil that generates magnetic fields in the x direction with respect to the cell

2.3.4 Simulations of the DFF under the influence of 3-D Coils

A 3-D coil system provides a good estimate of multi-dimensional fields, in an environment where the orientation of magnetic is unknown or keeps varying. Fig. 2.8 shows the 3 orthogonal coils with their radii as shown. If each coil was injected with a current, the total magnetic field density that could affect the DFF is expressed as:

$$B_T = r = \sqrt{(B_{0(xy)}^2 + B_{0(xz)}^2 + B_{0(yz)}^2)} \quad (2.3)$$

In spherical coordinates, the resultant fields, as shown in (2.3), can take any orientation depending on the magnitude and polarity of the coil currents in each of the coils. Fig. 2.13, adapted from [59], shows a spherical coordinate example, with the coils' currents equal in magnitude, hence $B_{xy} = B_{xz} = B_{yz}$. The resultant field, B_T , has an angle of inclination, $\theta = 55^\circ$, an azimuth angle, $\phi = 45^\circ$ and a magnitude as defined in 2.3. The following equations give the relationship between the angles and the coil fields.

$$\theta = \arctan \left(\frac{\sqrt{B_{yz}^2 + B_{xz}^2}}{B_{yz}} \right) \quad (2.4)$$

$$\phi = \arctan \left(\frac{B_{xz}}{B_{yz}} \right) \quad (2.5)$$

By using the spherical coordinate systems, the resultant magnetic field can be rotated to realise a specific field orientation and magnitude. Therefore, a SFQ cell can be analysed for vulnerability against such vector field in any plane over 360° . The representation in Fig. 2.13 can be viewed using magnetic field vector glyph plot as shown in Fig. 2.14. The magnetic vector fields were obtained by plotting along the x -axis or $y = 0$. The vector field can be seen to agree with the theory in Fig. 2.13, marked by the dashed rectangle in Fig. 2.14. The change in direction outside the box is due to magnetic field interference at a point where one of the coils penetrates the vector plotting plane.

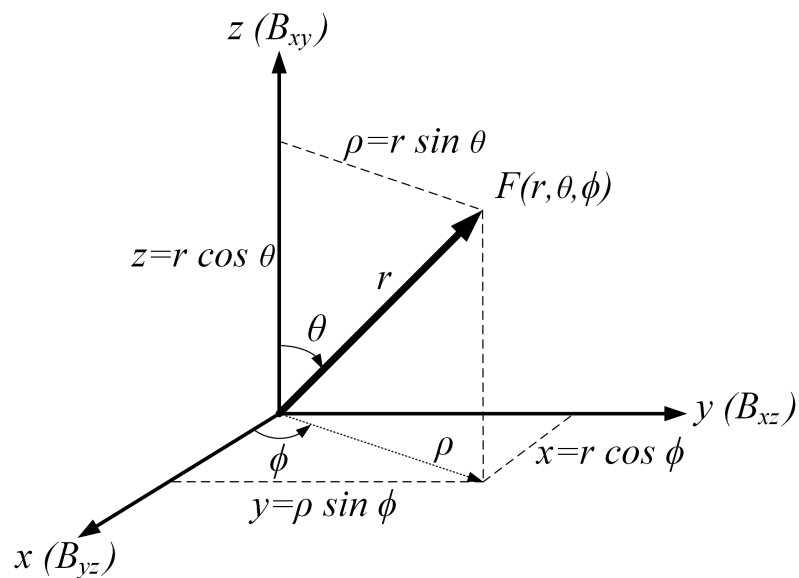


Figure 2.13: The resultant magnetic field in spherical coordinates

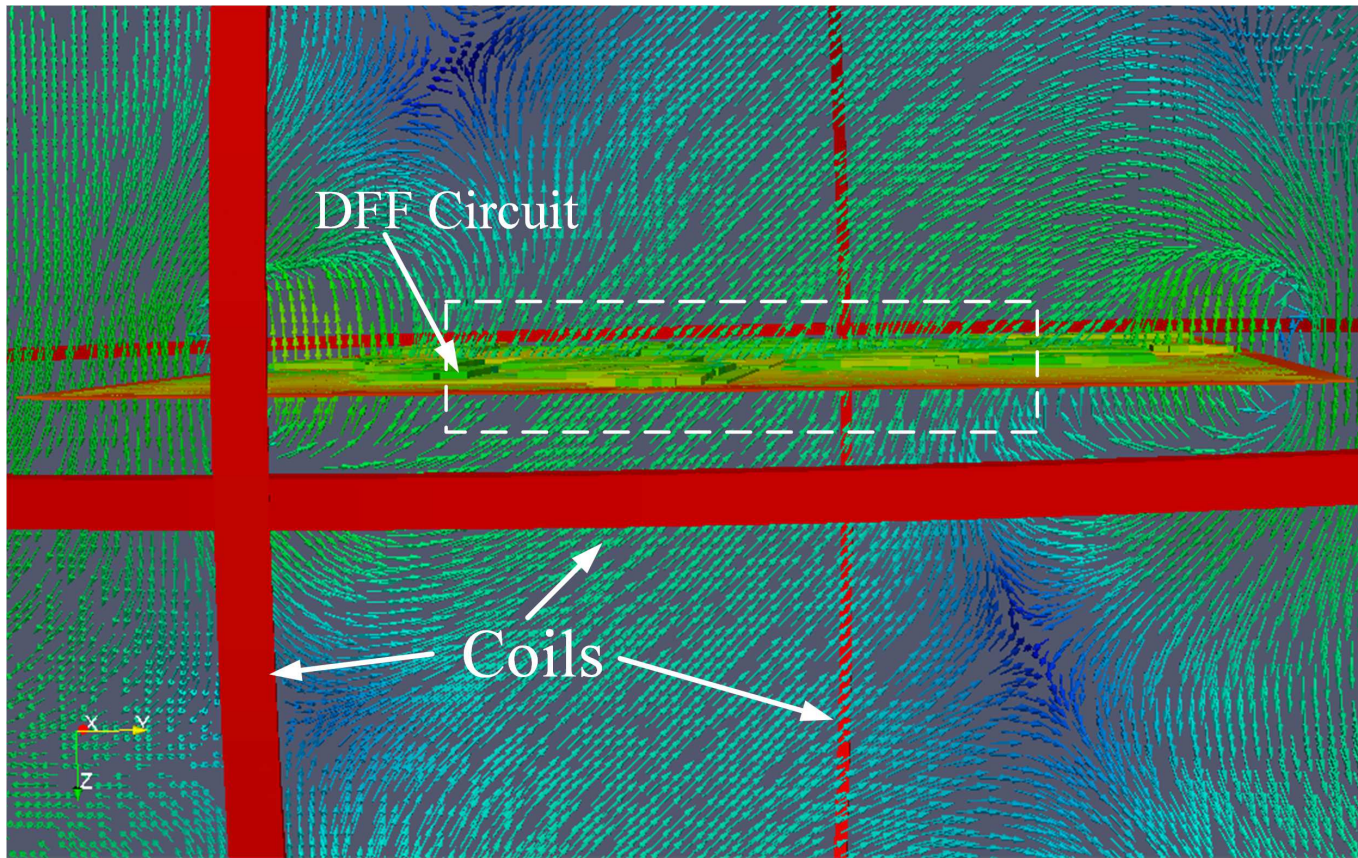


Figure 2.14: A magnetic field vector plot of the DFF surrounded by 3 coils that produce approximately an equal amount of magnetic field each. The resultant is a magnetic field that penetrates the DFF at an angle, as shown by the arrows inside the dashed box.

For instance, if a current of 4.5 mA is injected in each coil, the DFF malfunctions with 0% margins in 3 out of 5 Josephson junctions, including margins skewed to positive or negative from the 0% on the rest of the components, as shown in Fig 2.15. Magnetic fields on the DFF, from each coil are summarised in Table. 2.2. The total critical field for the DFF, according to (2.3) is $37.4 \mu\text{T}$. The coil fields in Table 2.2 are not the same because the coils do not have the same radius to aid separation between them (Fig. 2.8). The resultant vector has a fixed orientation angles of $\theta \approx 55^\circ$ and $\phi \approx 45^\circ$ that can be varied through the manipulation of magnitude and polarity of the current in each coil.

Name	Margins		
B#	[..... =====]	0.0,	22.5
B1	[..... =.....]	0.0,	0.0
B2	[..... =.....]	0.0,	0.0
B3	[..... =.....]	0.0,	0.0
B4	[..... =====]	0.0,	90.0
B5	[..... =====]	0.0,	20.4
I#	[..... =====]	-32.3,	0.0
IB1	[..... =====]	-34.5,	0.0
IB2	[..... =====]	-57.0,	0.0
L#	[..... =.....]	0.0,	0.0
L1	[..... =.....]	0.0,	0.0
L2	[=====]	-90.0,	0.0
L3	[..... =====]	0.0,	90.0
L4	[=====]	-90.0,	0.0
L5	[=====]	-90.0,	0.0
L6	[..... =.....]	0.0,	0.0
L7	[=====]	-90.0,	0.0

Figure 2.15: DFF bias and parameter margins with a current of 4.5 mA injected in each of the three coils. The distribution signifies failure of the DFF operation. At this stage, the DFF exhibits wrong switching patterns.

Table 2.2: Magnetic fields produced by the 3-D coils - the total magnetic field acting on the DFF is a vector summation of the three i.e. $37.4 \mu\text{T}$.

Coil	Radius (μ)	$B_0(\mu\text{T})$
xy	125	22.6
xz	130	21.75
yz	135	20.44

2.4 Simulations with the DC-SFQ cell

Interface cells, such as the DC-SFQ, are among the most sensitive units in most SFQ circuit variants. This section discusses how the 3-D coil system was used to generate uniform magnetic fields on the cell. The DC-SFQ was simulated and laid out according to the *Hypres'* 4.5 kA/cm^2 process. The results obtained at this stage were used to design shielding solutions that are reported in Chapter 3.

The schematic for the DC-SFQ is shown in Fig. 2.16 and a layout in Fig. 2.17. Simulations with the yz -coil showed that the unshielded DC-SFQ failed at a magnetic field density of $211 \mu\text{T}$ (for -42 mA coil current) or $200 \mu\text{T}$ (for 39.7 mA coil current). Further, a 3-D coil system caused total circuit malfunction at a magnetic field density of $37.4 \mu\text{T}$ (for -4.5 mA current in each coil) or $63 \mu\text{T}$ (for 7.5 mA current in each coil). For the 3D coils, the quoted magnetic field densities are vector sums of fields produced by all 3 coils, similar to those indicated in Table 2.2. Just like in the DFF, the DC-SFQ shows sensitivity to external magnetic fields that eventually causes the it to fail. This is a common occurrence in SFQ based digital circuits that rely on SQUID loops. The orientation of the magnetic field produced by the 3-D coils causes failure even at low strengths. However, with the in-plane field orientation produced by the yz -coil the DC-SFQ is quite immune to such fields and could operate in an ambient field exceeding the Earth's, without comprising functionality and operating margins, if properly aligned.

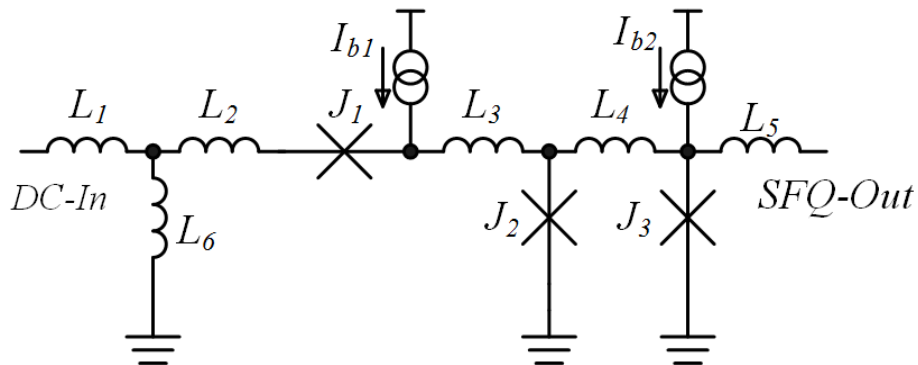


Figure 2.16: A DC-SFQ with parameters: $L_1 = 0.56 \text{ pH}$, $L_2 = 0.52 \text{ pH}$, $L_3 = 1.0 \text{ pH}$, $L_4 = 4.78 \text{ pH}$, $L_5 = 2.2 \text{ pH}$, $L_6 = 4.1 \text{ pH}$, $J_1 = 225 \mu\text{A}$, $J_2 = 225 \mu\text{A}$, $J_3 = 250 \mu\text{A}$, $I_{b1} = 275 \mu\text{A}$ and $I_{b2} = 175 \mu\text{A}$. Optimised bias margins: $-56\% \sim 34\%$.

2.5 Conversion from Webers (Wb) to Tesla (T)

An electrical current flowing through a superconducting loop causes a magnetic field, $\Phi = LI$ in *Webers* (*Wb*). Where L is the inductance of the loop. Due to flux quantization, the total magnetic flux is the multiples (n) of the magnetic flux quantum, i.e. $\Phi = n\Phi_0$. In the case of virtual circular coils made around cells, as it has been shown in the previous sections, it becomes imperative to employ *Biot-Savart* Law to estimate the total magnetic field density on a cell. The cell is situated very far away from the

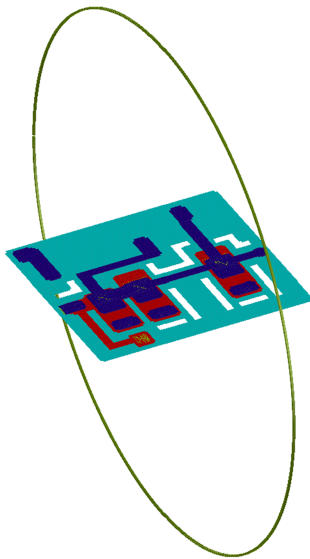


Figure 2.17: The DC-SFQ simulated with the yz -coil that generates magnetic fields in the x direction with respect to the cell

coil and the magnetic field degrades as the distance away from the coil increases. Fig. 2.18 depicts a simplified scenario with a SFQ cell in the centre and a current I , flowing through a coil of radius R . A simplified version of the *Biot – Savart* Law indicates that the magnetic field at the centre of the coil will be given as:

$$B_0(x = 0, y = 0, z) = \frac{\mu_o I R^2}{2(R + z^2)^{\frac{3}{2}}} \quad (2.6)$$

$$B_0 = \frac{\mu_o I}{2R} \quad (2.7)$$

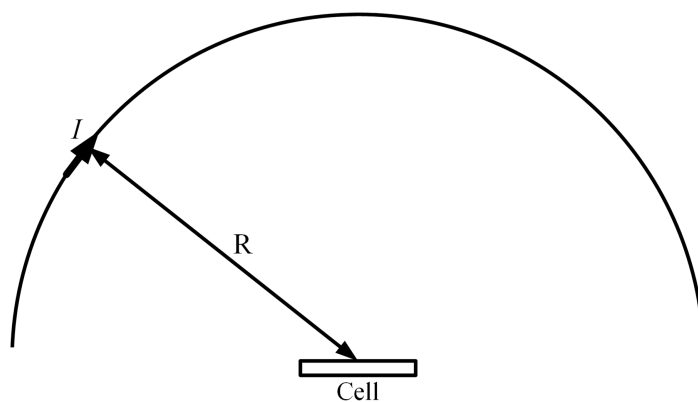


Figure 2.18: An illustration of a circular current carrying coil with an SFQ cell at its centre

The quantity B_0 (in Tesla, T), is the magnetic field calculated over a specified area. Therefore, any calculation of B_0 from a specific point on the coil needs to have an effective area defined. In this case, it is estimated that if the coil is large enough with respect to the cell, then the cell lies within this effective area. This, at best, is an approximation as depicted in Section 2.3.2. To ensure that the magnetic field is uniform over the entire cell, the coil has to be made larger with respect to the cell area. For instance, the explanation given in Section 2.3.2 used a cell with area $A = 1 \times 10^{-8} \text{ m}^2$ (i.e. A DFF cell of $100 \times 100 \mu\text{m}$) and a minimum coil area of $4.52 \times 10^{-8} \text{ m}^2$ (i.e. A coil with $R = 120 \mu\text{m}$). This results in a coil to cell area ratio of 4.52. The ratio is specific to the conditions stated, otherwise, the cell dimensions dictate the required minimum coil size and the ratio could be different. The rule of thumb is to make sure that the coil is made much larger, with respect to the cell.

2.6 Validation of coupling coefficients

2.6.1 Concentric Coils

Coupling coefficients between coils and circuit inductance are calculated by algorithms in *InductEx*. Since this work depends entirely on these coefficients, a validation had to be carried out to ensure the values are accurate. Mutual inductance between two elements is defined by the following expression:

$$M = k\sqrt{L_c L_i} \quad (2.8)$$

where k is the coupling coefficient, L_c the self inductance of the coil and L_i the self inductance of any of the inductors on the SFQ cell. An example of two concentric coils, with radii $R_1 > R_2$, is hereby considered. This setup, adapted from [60] is shown in Fig. 2.19. Analytical results can be obtained using proper formulae already available. The analytical results are then compared with the ones extracted by *InductEx*. This approach can confirm and validate the results obtained by this tool.

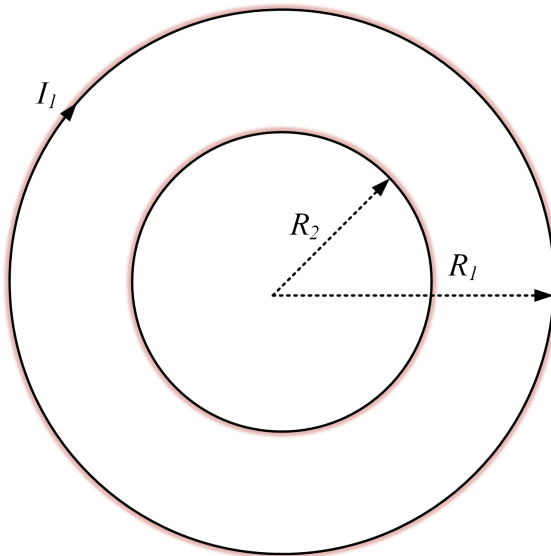


Figure 2.19: An illustration of concentric coils, with a current I_1 flowing through the larger coil

The magnetic field produced by the larger coil, with radius R_1 , for a current I_1 is $\Phi = L_1 I_1$, where L_1 is the self inductance of the coil. However at the centre of this coil, the magnetic field density degrades according to the *Biot – Savart* Law. As such the magnetic field density is expressed as follows;

$$B_1 = \frac{\mu_0 I_1}{2R_1} \quad (2.9)$$

If $R_1 \gg R_2$, then the flux linkage between the coils, which also depends on the area inside the smaller coil, can be approximated as [60]

$$\Phi_{12} = B_1 A_2 = \left(\frac{\mu_0 I_1}{2R_1} \right) \pi R_2^2 = \frac{\mu_0 \pi I_1 R_2^2}{2R_1} \quad (2.10)$$

Therefore, the mutual inductance is given by

$$M_{12} = \frac{\Phi_{12}}{I_1} = \frac{\mu_0 \pi R_2^2}{2R_1} \quad (2.11)$$

which clear independence of the mutual inductance M_{12} on the current in the coil that produced the coupled magnetic flux. From this, the coupling coefficient can be calculated as in (2.8).

Coils of different radii were chosen and coupling coefficients for both analytical and calculated (extracted with *InductEx*) were obtained and compared. The results are shown Table 2.3. The results in the table reveal two fundamental factors that are vital in using coils to generate magnetic fields. Firstly, the coupling coefficients become more accurate if $R_1 \gg R_2$ and secondly, the coupling coefficients calculate numerically with *InductEx* are quite accurate.

R_1 μm	R_2 μm	Analytical	<i>InductEx</i>	Difference
150	75	0.0977	0.1086	11.2%
150	60	0.0714	0.0759	6.3%
200	75	0.06198	0.0653	5.36%
200	60	0.0453	0.0464	2.43%

Table 2.3: Comparison of analytical and extracted coupling coefficients

2.6.2 Coils and Circuit Inductors

A separate analysis was considered for a coil with a rectangular inductor in the centre of the coil. The inductor has length l and width w and the setup is illustrated in Fig. 2.20. If the analysis in Section 2.6.1 is used, the area that is covered by the smaller circle is represented by the area of the rectangular inductor, the extracted values do not match with the analytical ones. However, there is always a factor of ≈ 19 (or $\approx 2\pi^2$) between the two coupling coefficients as shown in Table 2.4. This is a special case and only applied when the rectangular inductor is in the same plane as the coil. The rectangular inductor can be considered as being made up of different smaller coils with radii equal to w .

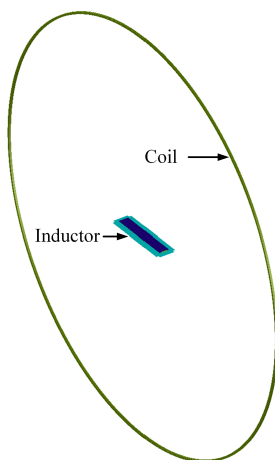


Figure 2.20: A coil with a co-axis rectangular inductor in the centre. The length of the inductor extends equally in both directions towards the coil

Coil Radius (μm)	Analytical k_A	Extracted k_E	k_A/k_E
50	0.03940	0.00215	18.349
75	0.02068	0.00105	19.695
100	0.01305	0.000668	19.537
125	0.00915	0.000485	18.872
150	0.00686	0.000365	18.785
175	0.00537	0.000286	18.781
200	0.00434	0.000232	18.707

Table 2.4: Analytical and extracted coupling coefficients between a coil and an in-plane rectangular inductor

The approach presented here does not give the exact values because the area used resembles that of a small coil with a radius that gives an area $A = l \times w$. A more accurate expression with which to calculate the mutual inductance and hence coupling for the representation in Fig. 2.20 is [60],

$$M = \frac{\mu_0 A}{4\pi^2 R} \quad (2.12)$$

where $A = l \times w$ being the area of the rectangular inductor and R is the radius of the coil. This method in (2.10) was drawn up through observation and using the results obtained in Table 2.4 and it is specific to the orientation of the coil and rectangular inductor depicted in Fig. 2.20. Other orientations reveal different relationships. Nonetheless, the analysis confirms the reliability and consistency of the coupling coefficients calculate by *InductEx*.

2.7 Chapter Conclusion

The vulnerability of SFQ circuits against unwanted magnetic fields has been established through simulations. Even low magnitude fields, in a specific orientation, have a potential to cause a significant shift in operating margins or even circuit failure. In this chapter, a method for generating uniform external magnetic fields on-chip has been presented and validated through simulations and visualization. In addition, since this work depends on coupling coefficients, a comparison of analytically obtained coupling coefficients and extracted ones, by *InductEx*, have been compared. It has been established that the coupling coefficients obtained by *InductEx* are indeed accurate. Further analysis and modelling is continued throughout the document. Having established a method for generating external magnetic fields on-chip using coils, mitigating approaches in the form of shields can be explored and analysed as presented in the next chapter.

Chapter 3

On-Chip Shielding of SFQ Circuits

3.1 Introduction

SFQ circuits need to be shielded from external magnetic fields, especially from the Earth and bias lines. Unlike in high frequency semiconductor electronics, SFQ circuits need to be shielded because magnetic fields in small quantities can cause complete malfunction. SFQ circuits are based on the propagation, switching and storage of the SFQ pulse. The SFQ is the smallest quantity of magnetic field and only one can be stored in a superconducting loop that has a Josephson junction. Any additional magnetic field to this loop will cause unwanted circuit switching and oscillations, which in turn would result in circuit's complete malfunction. The external magnetic fields are usually much larger than the SFQ. Therefore, SFQ circuits have to be shielded from unwanted magnetic fields, at all times. In SFQ circuits, shielding is as crucial as the cooling process initially needed to realise the superconducting state. Without cooling, the superconducting state cannot be attained, similarly, adequate shielding is mandatory for proper functioning of SFQ circuits.

3.1.1 Shielding Background

Shielding can be defined as any means used to reduce electromagnetic fields in a specified area [61]. The assumption is that there is an area B that needs to be protected from electromagnetic (EM) fields produced in area A . The analogy of shielding is captured in Fig. 3.1.

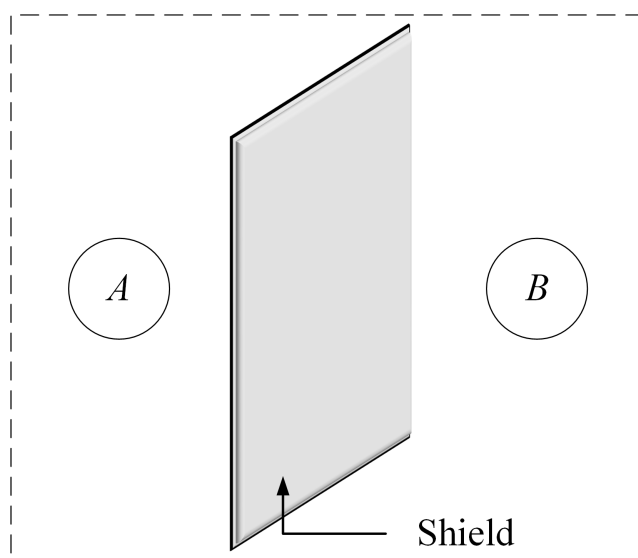


Figure 3.1: A simplified view of a shield placed between Areas A and B to reduce EM interaction between the two areas.

Ideally, the interference produced in area A should be entirely absorbed and guided away by the shield. Such a shield is expensive and almost impossible to attain and a compromise is always accepted.

Shielding effectiveness (SE) is a term that is used as a figure of merit for a shield. SE is expressed in decibels (dB) and can take any of the two forms owing to the basic components of an EM field, which are electric and magnetic, hence we have [62, 63]:

$$SE_E = 20 \log \frac{E_0}{E_1} \quad (3.1)$$

where SE_E is SE expressed in terms of electric field E , E_0 is the electric field measured before a shield is installed and E_1 is the electric field measured at the same point after a shield is installed. Alternatively,

$$SE_H = 20 \log \frac{H_0}{H_1} \quad (3.2)$$

where SE_H is SE expressed in terms of magnetic field H , H_0 is the magnetic field measured before a shield is installed and H_1 is the magnetic field measured at the same point after a shield is installed. Measurements for the E and H parameters are done at the affected or protected area, such as area B in Fig. 3.1, assuming area A is the source of interference. In general the SE of a shield is affected by three parameters namely the thickness of the shielding material, the frequency of the incident magnetic field, shielding material and distance from field source to the shield [62, 63]. For the shielding material, any EM field can be affected by and propagation factor expressed as follows [61]:

$$\gamma = \sqrt{j\omega\mu + (\sigma + j\omega\varepsilon)} = \alpha + j\beta \quad (3.3)$$

where the medium's conductivity is σ , permittivity is ε , permeability is μ , α is the attenuation constant and β is the phase change. The attenuation constant should always be high to realise better shielding effectiveness. A good shield has a good combination of σ , ε and μ , that yields a high attenuation. Alternatively, SE of a shield can be determined from three properties namely; reflection (R), absorption (A) and multiple reflection factor (B). Therefore, SE can also be expressed as:

$$SE = R + A + B \quad (3.4)$$

The three terms in (3.4), all expressed in dB , account for reflection, (R), of some of the incident wave on the shield surface, absorption, (A), of some of the field within the shield and multiple reflection, (B), that can occur within the shield, thereby creating a secondary source that could still affect the shielded area. If the absorption is large enough (typically $A > 10dB$ [63]), the multiple reflection factor, B can be neglected and (3.4) becomes $SE = R + A$.

In Electromagnetic Compatibility (EMC) applications, several types of materials and configurations are used. These include, ferromagnetic and ferrimagnetic materials, and many variations of conductive, reflective or absorptive materials. These shields can be configured as cylinders, rectangular enclosures or simply perforated flat sheets depending on the application. In EMC, the concern is that an electrical or electronic circuit or system should not emit electromagnetic interference (EMI) that may cause disturbance resulting into malfunction in another system. However, the EMI problem in SFQ electronic systems is usually one sided. The SFQ circuit might not produce EMI that would affect nearby systems to the

point of malfunction, but it has to be protected from other EMI sources. So the shielding challenge is not compliance, but rather protection. However, due to reciprocity, a shield designed to keep EMI from the SFQ circuit should prevent emission of EMI into the circuit's environment.

3.1.2 Superconductor Material Based Shields

The use of superconductors in the implementation of shields is not new. Simulations and further analysis for implementation can be found in [64, 65], among others. Superconductors make a good shield because of the infinitely high conductivity, σ , available when the superconducting state is attained [66, 67]. Two types of superconductors exist: Type I and Type II. Type I superconductors are diamagnetic in that they are able to expel magnetic fields from their core once the superconducting state is attained through cooling beyond their critical temperatures. However, Type II superconductors do not exhibit diamagnetic behaviour. According to Maxwell's equations,

$$\nabla \times \mathbf{E} = -\frac{\partial \mathbf{B}}{\partial t} \quad (3.5)$$

therefore,

$$\mathbf{E} = \frac{\mathbf{J}}{\sigma} = \mathbf{0}, \text{ for } \sigma = \infty \quad (3.6)$$

for

$$\nabla \times \mathbf{H} = \mathbf{J} \quad (3.7)$$

where \mathbf{E} is the electric field, \mathbf{H} is the magnetic field, \mathbf{B} is the magnetic field density and \mathbf{J} the current density in the superconducting material due to the external magnetic fields. From (3.5) to (3.6) to (3.7), it can be seen that \mathbf{B} must be a constant for \mathbf{E} to be zero. This phenomenon is fundamental to the development of screening currents that could form on the superconductor surface to oppose any change in \mathbf{B} . The magnetic field will then be excluded from the core of the superconductor in what is called the Meissner effect [68, 69], defined by the London equation:

$$\nabla^2 \mathbf{B} = \lambda^{-2} \mathbf{B} \quad (3.8)$$

where λ is the London penetration depth, signifying the decay of the magnetic field in the superconductor material by a factor, $\frac{1}{e}$, as per one of the solutions of (3.8), that is

$$\mathbf{B}_z(x) = \mathbf{B}_z(0) \exp\left(-\frac{x}{\lambda}\right) \quad (3.9)$$

where x is the distance into the bulk of the superconductor from the surface [70].

Meissner effect is only applicable to Type I superconductors under specific conditions. Some of the fields penetrate the superconductor to the extent determined by the London penetration depth (λ) [69] of the superconducting material. For most shielding applications, the penetration depth is insignificant except when the magnetic field frequency exceeds 100 GHz [66]. At that frequency, the normal and supercurrents co-exist in the superconductor, thereby limiting the skin effect to the penetration depth.

At that point the superconductor behaves like a normal metal. The superconducting state in Type I materials can also be lost if the applied magnetic field exceeds a critical field H_c , beyond this point, normal metal shielding analysis would apply.

In Type II superconductors, the Meissner effect exists only up to the lower critical field, H_{c1} (equivalent to H_c of Type I materials) beyond which, a mixed state exists up to the upper critical field, H_{c2} . The mixed state is characterised by increased penetration of the magnetic flux. Therefore, total expulsion of magnetic field is impossible in Type II materials [67]. The upper critical field, H_{c2} is greater than H_{c1} and comparatively also greater than H_c for Type I materials. Therefore, Type II superconductors can withstand higher magnetic fields without losing their superconducting state.

The theory presented so far applies to shielding applications that use thick superconducting samples and does not directly apply to SFQ circuits. However, niobium, the main superconductor in low-Tc SFQ circuits, is a Type II superconductor and perfect diamagnetism is non-existent. It is universally agreed that for effective shielding, the thickness of the shielding superconducting material must be large, much larger than its penetration depth. This is impossible to achieve with the thin films used in SFQ circuits. An infinite ratio of the film thickness, d , to the London penetration depth, λ , is required for an ideal shield. However, the films used in SFQ circuits are very thin, hence, the ratio is always finite. For instance, the $M3$ layer in the *Hypres'* 4.5 kA/cm² process, has a thickness of $d = 600$ nm and penetration depth of $\lambda = 90$ nm [54]. The ratio $\frac{d}{\lambda} = 6.67$. This reveals that shielding in SFQ is never perfect as $\approx 10\%$ of the magnetic field will still find its way through the shield [71–74]. Nonetheless, thin superconducting films can still be used to make on-chip shields to cut coupling between external magnetic fields and circuit inductors.

3.1.3 Factors that determine shielding effectiveness (SE)

SE of superconducting shields are expressed in the same way as in normal shields as explained in Section 3.1.1, by simply measuring the amount of magnetic field that crept through the shielding and compare it to the original. However, there are a number of factors that can determine the SE or attenuation factor. Such factors include the material used, the shape of the shield, conductivity of the shield, frequency of the magnetic field to be shielded, the orientation of the shield with respect to magnetic field direction and thickness of the shield and the presence of apertures of any form on the shield as these might allow stray fields to leak through the shield [66].

3.2 Simple Superconducting Shields for Strip-lines in SFQ Circuits

Simple analyses and simulations are usually important in predicting behaviour that could easily be extrapolated to complex ones. Narrow superconducting elements or strip lines were used to analyse shielding on a small and conceptual scale. The layout in Fig. 3.2 was used to determine the shielding behaviour one strip line has on another and the effect of grounding on the effectiveness of such simple shields, adapted from [20, 75]. The layout was made in the *Hypres'* 4.5 kA/cm² using $M2$ as the shielding layer and $M3$ and $M1$ as the coupled strip lines. A circuit equivalent of the shielding analogy is shown in Fig. 3.3.

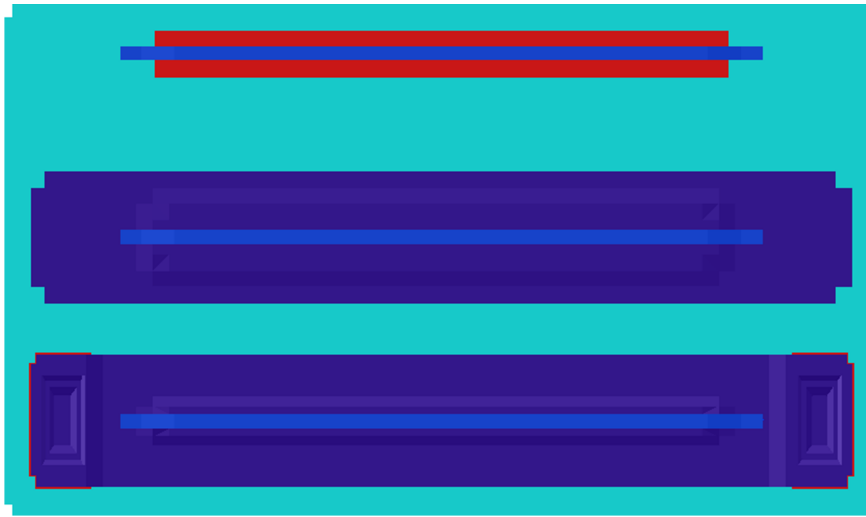


Figure 3.2: Layout of three scenarios: Top: $M1$ (red) under $M3$; Middle: $M1$ and $M3$ separated by a wide shielding layer in $M2$ and at the bottom $M1$ and $M3$ separated by a shield in $M2$, grounded at both ends.

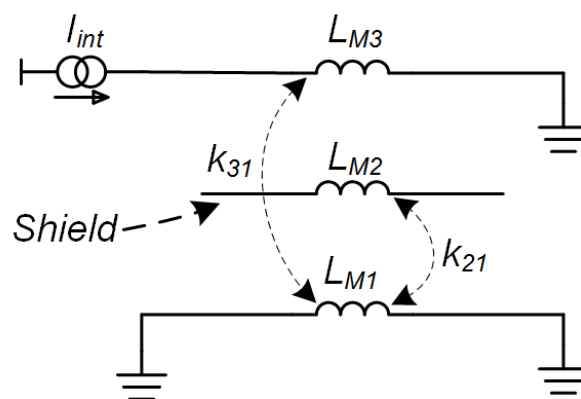


Figure 3.3: An equivalent circuit of the stripline shielding implementation. I_{int} is the equivalent current that causes magnetic field interference ($\Phi = L_{M3}I_{int}$). L_{M3} , L_{M2} and L_{M1} are the inductance of the respective layers. k_{31} and k_{21} are coupling coefficients as shown by the arrows.

Coupling coefficients were used to determine if shielding had taken place since reduced coupling between two structures indicates the occurrence of shielding of some form. Table 3.1 shows the coupling coefficients between strip lines and between shielded line and shield in both ungrounded and grounded setups. As indicated in Table 3.1, the coupling (k_{31}) between $M3$ and $M1$ layers reduces with shielding and is lowest if the shield is grounded at both ends. It was noted that grounding the shield layer at one end had no effect on the coupling, as it was the same as in the ungrounded case. This indicates that a single grounding does not provide a sufficient increase in the flow of induced surface currents that are key to the shielding process. The inductance of the $M1$ layer covered by the ungrounded shield dropped from 4.95 pH to 4.15 pH , while in the grounded shield case, its inductance dropped to 3.14 pH . The phenomenon was observed throughout, whereby the in-circuit inductance reduces when an SFQ circuit is covered by a shield. The coupling between the shield in $M2$ and the layer underneath ($M1$), k_{21} , is also recorded in Table 3.1. An ungrounded shield couples more to the $M1$ layer thereby providing less shielding because different current paths exist and the shield inductance is normally high. The values of k_{21} suggest that an ungrounded shield offers no protection to the SFQ circuit as any surface currents on the shield could couple to the circuit inductance, easily. However, if the shield is grounded, only one path exists and surface currents are easily channelled to ground, thereby providing less coupling between $M1$ and the shielding. Therefore, a grounded shield provides better shielding. However, a grounded shield, results in the reduction of inductance of the shielded circuit structure.

	Unshielded	Shielded	Shielded+Grounded
k_{31}	0.3061	0.1621	0.0732
k_{21}	-	0.3494	0.0454

Table 3.1: k_{31} - Coupling between $M3$ and $M1$; k_{21} Coupling between $M2$ and the shield in $M1$

3.3 Preliminary Analysis of New Shielding Implementations

The shielding example shown in Section 3.2 employs a continuous superconducting layer in $M2$ to cover the entire strip line in $M1$ layer. This type is hereby referred to as the solid shield. The solid shield, a continuous superconducting layer, was the only current effective way to keep out external magnetic fields on-chip, at the beginning of this work [20,33]. However, such an approach results in the circuit inductors being reduced since the magnetic field lines are constrained by the presence of the shield. It also makes input/output and bias lines difficult to place. This requires that all circuit inductors be redesigned and possibly some circuit elements relocated. Therefore, a grid-patterned shield with minimal effect on the values of inductances was also investigated and presented here.

In this work, the solid shield was investigated along side the novel grid type shielding. From the start, the grid shield was discovered to have less effect on circuit inductance, even though this is not a measure of shielding effectiveness. In the shielding analysis simulations, external magnetic fields were modelled using 3-D coils as reported in Section 2.3. Solid and grid shields were laid on top of the DFF and these implementations are shown in Fig. 3.4. Fig. 3.5(a) and Fig. 3.5(b) show 3-D coils around the solid and grid shielded DFF, respectively. The shields were first investigated, through simulations, in the absence of external magnetic field - no current in the coils. The grid shield was made with $2.5 \mu m$ strips with a spacing of $5 \mu m$. Table 3.2 shows the values of DFF inductances when grid and solid shields are implemented. Both shields were grounded at identified positions on the cell for more effective shielding [20]. It can be observed that a solid shield leads to a higher reduction of inductances than a grid shield.

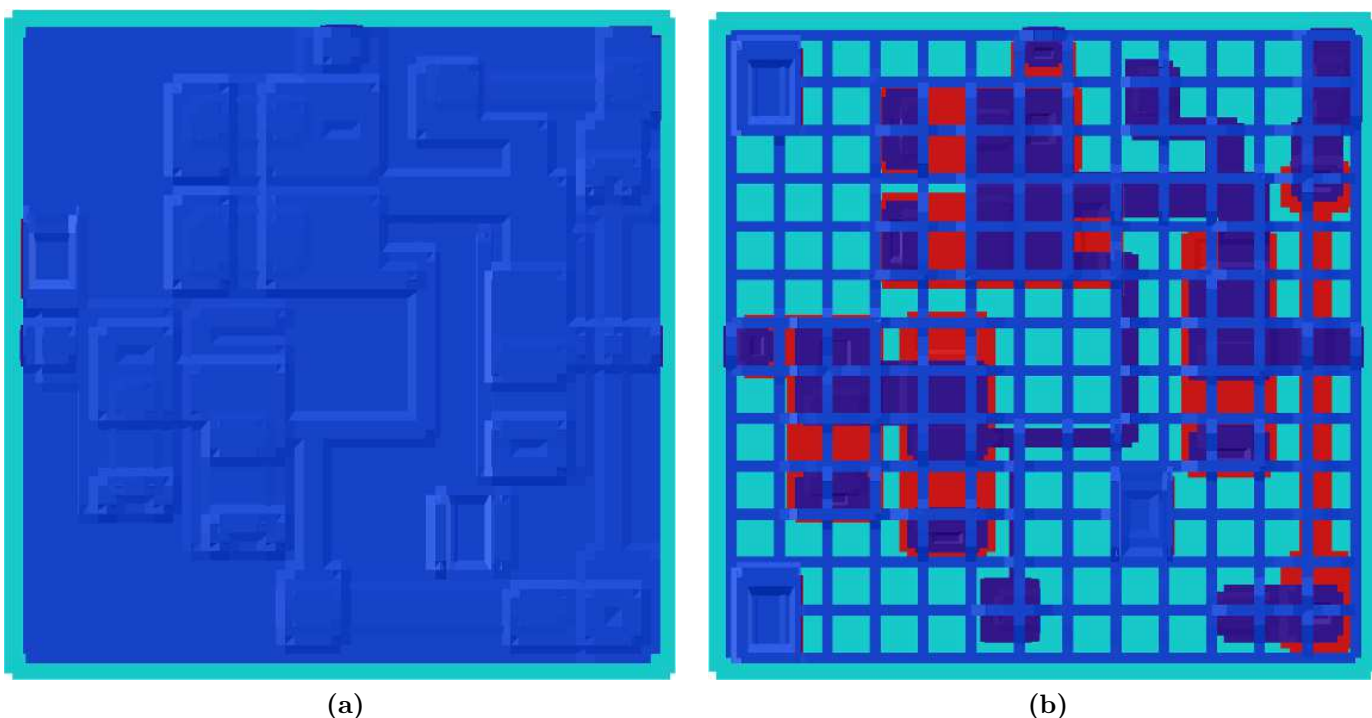


Figure 3.4: The DFF covered in (a) a solid shield and (b) A grid patterned shield made with $2.5 \mu m$ strips and a spacing of $5 \mu m$

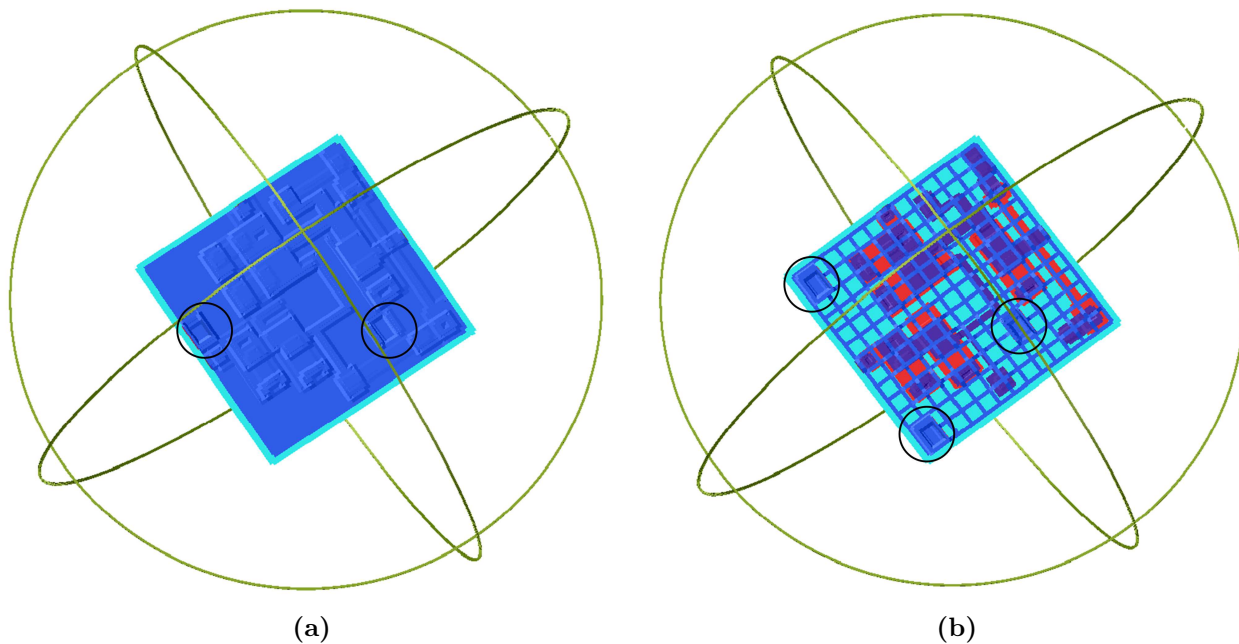


Figure 3.5: A DFF covered in (a) solid shield and (b) grid shield. The circled position indicate ground contacts. It was observed that a minimum of two contacts improved the shielding. Ideally, ground contacts should be positioned roughly in the same line axially. However, layout constrains may not accord the design such a privilege as such positions could be occupied by interface and bias lines.

The effectiveness of these shielding approaches can be viewed through our in-house magnetic and current density visualization tool as shown in Fig. 3.6. The DFF is much smaller compared to the coil diameter. Therefore, it was easier to visualize the fields within the DFF. Furthermore, if a shield keeps an externally applied field out, it would keep an internally generated field in, due to reciprocity. Hence, a port on the DFF (circled in Fig. 3.6) was excited with a sinusoidal voltage of $1v$ at a frequency of 10 GHz. The magnetic patterns reveal that the solid shield is marginally more effective than the grid one. In Fig. 3.6(a), the DFF is unshielded and magnetic fields freely spread out from the injection point within the DFF. The DFF covered with a solid shield is shown in Fig. 3.6(b) and most of the magnetic field is spread within the DFF because the solid shield provides a continuous flow of surface currents that in turn generate other fields. However, the grid shield in Fig. 3.6(c) is able to interrupt the magnetic field lines without providing a continuous flow of surface currents. From the simulations shown in Fig. 3.6, a field of $46 \mu\text{T}$ is found at points marked X for the unshielded DFF, $0.387 \mu\text{T}$ for the solid shield and $0.0178\mu\text{T}$ for the grid shield. At the point marked X, It shows that the grid shield is better at containing fields than the solid shield. However, more points are required to ascertain the overall effectiveness of a shield when using the visualization approach [58]¹.

Table 3.2: Values of DFF circuit inductances in presence of grid and solid shields- regardless of coil type used

L	$L(\text{Original}) - pH$	$L(\text{Grid}) - pH$	$L(\text{Solid}) - pH$
L_1	1.86	1.65	1.46
L_2	1.59	1.42	1.06
L_3	7.73	7.19	5.69
L_4	1.50	1.34	1.25
L_5	2.13	1.79	1.44
L_6	1.30	1.11	0.88
L_7	1.91	1.72	1.48

¹Material presented in this section is part of already published work by the author [58]

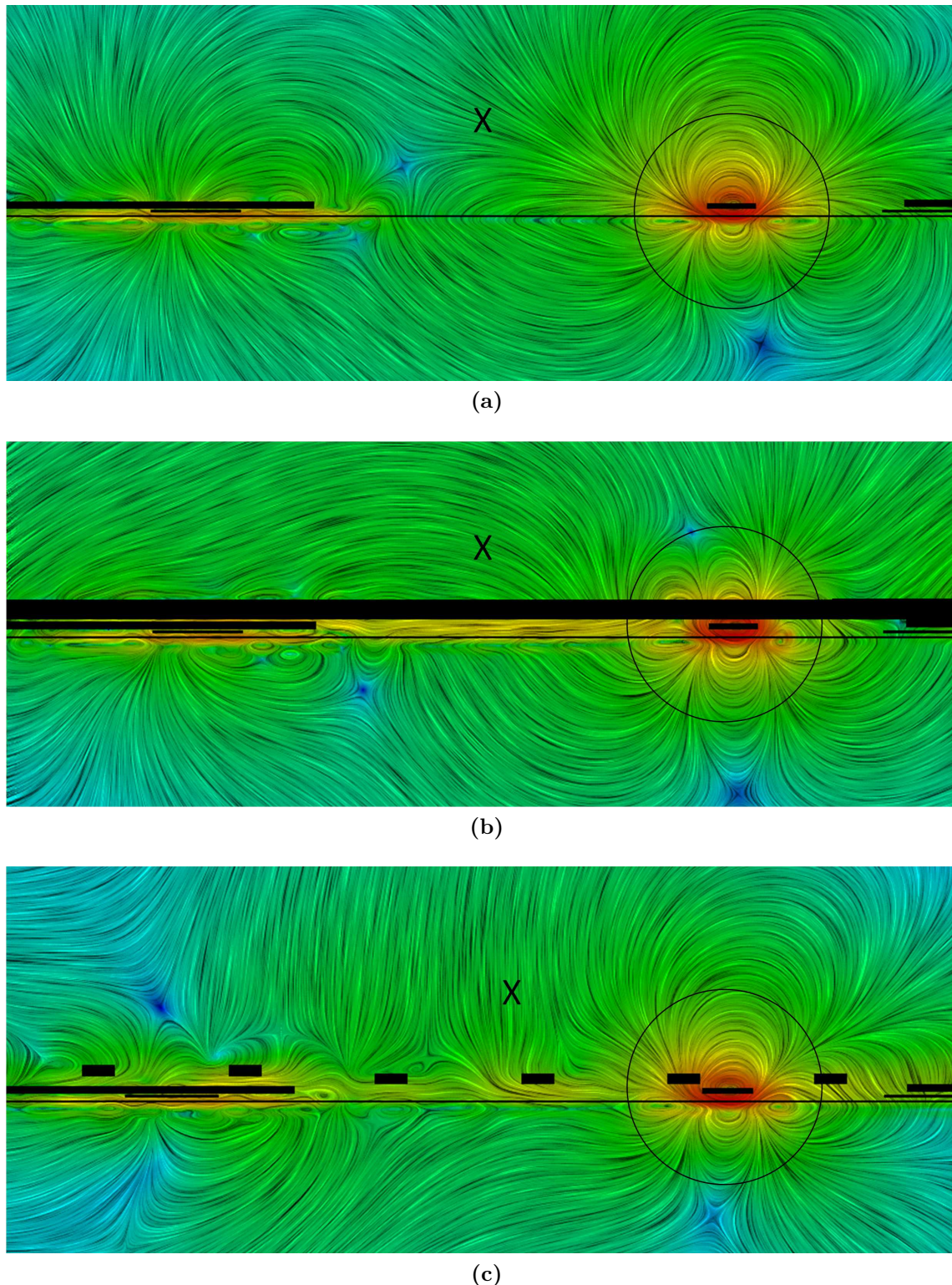


Figure 3.6: Magnetic field images with cross-section of the DFF and a test current injected at the encircled points - no external fields. (a) unshielded DFF - cross-section, (b) with solid shielding, (c) with grid shielding. Point X was chosen arbitrarily.

3.4 Grid-patterned Shield Concept

The grid patterned (or simply grid) shield is essentially a mesh of superconducting strips or a solid shield that has carefully and uniformly placed apertures (or moats). In shielding theory, a shield that is perfectly closed, has the highest shielding effectiveness, as there are no apertures that could permit stray magnetic fields to creep through. In this case, in theory, the solid shield should report a better shielding effectiveness than the grid. However, in SFQ circuits, the solid shield has a tendency of reducing the inductance of circuit strip lines. In some cases, extra work is required to redesign the circuit inductance to original optimized values. Fig. 3.7, shows an outlook of a section of a typical grid shield.

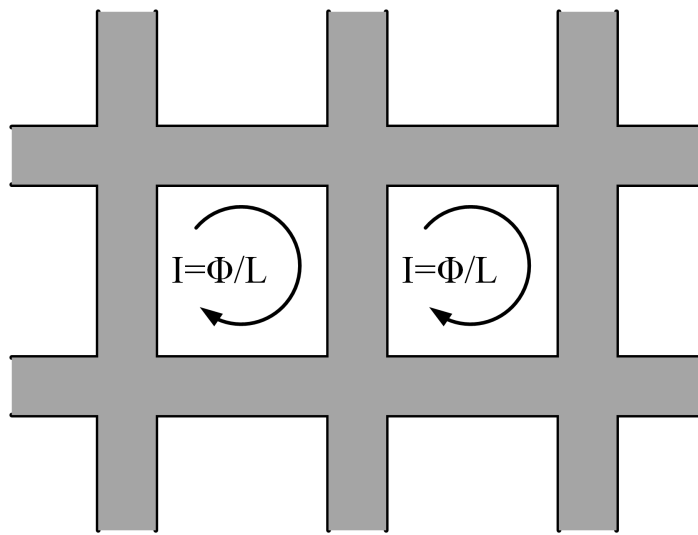


Figure 3.7: The Grid shield showing the superconducting loop created by each aperture.

Each aperture in the grid forms a superconducting loop that can carry a current equivalent to the coupled external magnetic field. Due to flux quantization, the flux $\Phi = n\Phi_0$, where Φ_0 is the flux quantum and n is an integer. The flux causes circulating currents around each loop, thereby contributing to the overall surface current for the shield. If the loop becomes large (i.e. bigger apertures), low loop currents indicate a weaker barrier that fails to prevent magnetic fields from permeating through. Hence, a grid with wider apertures creates a weaker barrier against magnetic fields. The density of the apertures reduces if wide apertures are used. Further, the bigger the superconducting loop, the smaller the circulating currents. Therefore, less shield circulating aperture currents ($I = \Phi_0/L$), because of the increase in loop inductance. In Fig. 3.8, It is shown that the wider the aperture, the more external fields it can let through [63]. A detailed analysis of the effect of grid spacing is reported in the upcoming sections.

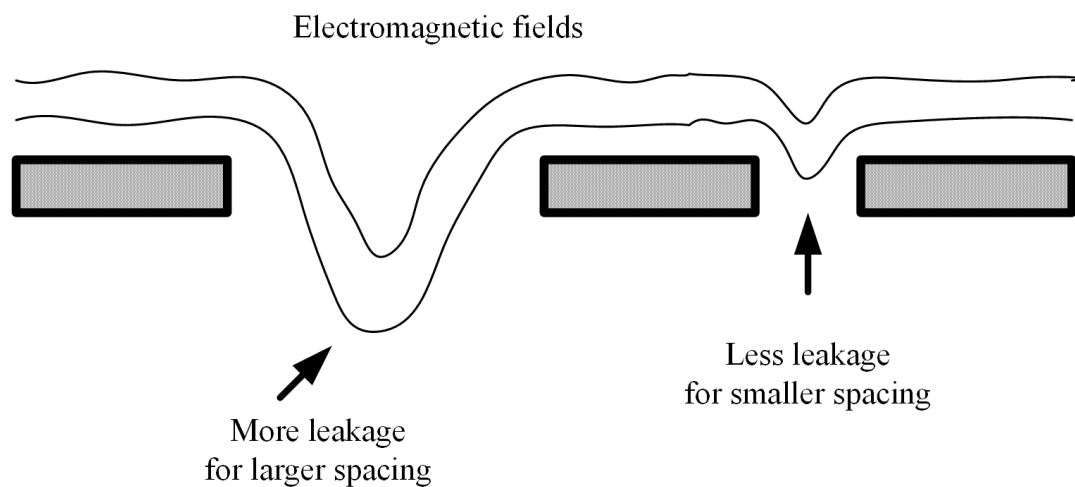


Figure 3.8: A cross section of a grid shield with different width of aperture - More stray field creep through wider apertures.

3.4.1 A Comparative Analysis of the Grid and Solid Shields

The analysis at this stage was done with magnetic fields from the xy , xz or yz coils and the 3-D coil setup reported in section 2.3. The orientation of the magnetic field was fixed and then reversed by changing the polarity of the currents in the coils. All three coils were injected with approximately the same amount of current, to compensate for slight differences in coil radii, and then varied simultaneously.

Due to the asymmetrical nature of most cell layouts, failure points were dependent on the direction of the magnetic field. Therefore, both positive and negative coil currents were used to reverse the produced

Table 3.3: Comparison of failure points of the DFF for the two on-chip shields with different sources of external magnetic field. The unshielded case is shown as a reference.

Coil(s)	Unshielded		Solid Shielded		Grid Shielded	
	-OFM	+OFM	-OFM	+OFM	-OFM	+OFM
<i>yz</i> -Coil	$90\mu T$	$68\mu T$	$121\mu T$	$146\mu T$	$171\mu T$	$126\mu T$
3-D Coils	$38\mu T$	$46\mu T$	$50\mu T$	$86\mu T$	$50\mu T$	$98\mu T$

Table 3.4: Comparison of failure points of the DC-SFQ for the two on-chip shields with different sources of external magnetic field. The unshielded case is shown as a reference

Coil(s)	Unshielded		Solid Shielded		Grid Shielded	
	-OFM	+OFM	-OFM	+OFM	-OFM	+OFM
<i>xy</i> -Coil	$47\mu T$	$39\mu T$	$464\mu T$	$321\mu T$	$96\mu T$	$84\mu T$
<i>xz</i> -Coil	$108\mu T$	$74\mu T$	$21\mu T$	$35\mu T$	$63\mu T$	$61\mu T$
<i>yz</i> -Coil	$211\mu T$	$200\mu T$	$340\mu T$	$171\mu T$	$381\mu T$	$237\mu T$
3-D Coils	$38\mu T$	$63\mu T$	$59\mu T$	$113\mu T$	$67\mu T$	$117\mu T$

magnetic fields. Consequently, two failure points were realized, of which the lower one was flagged as critical. For each SFQ cell, there is a point at which the shielding no longer offers protection, called an operating field margin (OFM) or failure point. The OFM of an SFQ cell is hereby defined as the point where the circuit parameter and bias margins diminish to 0%.

A grid shielded DFF, with current through the *yz*-coil, failure occurred at a magnetic field density of $171\mu T$ (or -34 mA) or $126\mu T$ (or 25 mA), while for the solid shield, it was at $121\mu T$ (or -24 mA) or $146\mu T$ (or 29 mA). The negative coil currents, in parenthesis, represent reversed direction of current flow. In a practical setup, external magnetic fields can take any orientation. To accommodate this, the DFF was simulated with 3-D coils as shown in Fig. 2.8, first the unshielded DFF and then the ones covered with grid and solid shields. Without shielding, the DFF failed at $38\mu T$ (or -4.5 mA) or $46\mu T$ (or 5.5 mA). The quoted currents, also in parenthesis, are injected into each of the coils. A grid shielded DFF failed at $50\mu T$ (or -6 mA) or $98\mu T$ (or 11.7 mA), while the solid shielded one failed at $50\mu T$ (or -6 mA) or $86\mu T$ (or 10.3 mA). In this case, the magnetic field densities are vector sums of fields produced by the 3 coils at the quoted current. The positive and negative OFMs are summarized in Table 3.3 for a better comparison of the shields along with the unshielded case of the DFF.

OFMs were also calculated for the DC-SFQ in the unshielded, grid-shielded and solid-shield cases. For the DC-SFQ, magnetic fields from the *xy* and *xz*-coils were also included. Calculated OFMs for the DC-SFQ are shown in Table 3.4.

In the DFF, both the grid and solid shields show improved shielding effectiveness against magnetic fields from the *yz* and 3-D coils. However, in the DC-SFQ, the solid shield performs poorly against magnetic fields from the *xz*-Coil. This shortcoming is explored further in the upcoming chapters. For best shielding, SFQ chips need to be aligned correctly against specific magnetic field vectors. In the results shown in Table 3.3 and Table 3.4, the OFMs under 3-D coil fields are lower than those for separate coils because of the orientation of the resultant field produced by the 3-D coils. Therefore, better shielding would be required against magnetic fields in that orientation.

3.5 Further Analysis of Grid Shield

3.5.1 Background

The shielding analysis presented here was done with layouts made with the *Hypres'* 4.5 kA/cm^2 process design rules [54]. The process's topmost layer, M3, which has technology fixed thickness $d = 600 \text{ nm}$ and penetration depth $\lambda = 90 \text{ nm}$, was used to implement on-chip shields. The use of orthogonal coils, shown in Fig. 3.9, envisages that magnetic fields, as vectors, can take any orientation. Therefore, the circuit needs to be protected against that. The magnetic field orientation, dictated by the direction of coil currents, remains constant and fixed for each simulation described here. Although the field vector was not swept over all directions, which could be time intensive for small sweep steps, it does contain equal components in each axial direction and thus permitting calculation of shielding efficiency in the presence of all axial components. The grid patterned shield was further simulated with Delay Flip-Flop (DFF), as before, and Direct Current to Single Flux Quantum (DC-SFQ) converter cells. The grid shield offers similar shielding protection to the normal solid shield, with an added advantage that it has less effect on circuit inductance. In our earlier simulations, only a grounded grid shield (in Fig. 3.11) of $2.5 \mu\text{m}$ grid bar width and spacing of $5 \mu\text{m}$ was considered and hereby referred to as the standard grid shield. In order to obtain the best possible grid configuration, seven grid spacing configurations were considered. All coupling coefficients between coils and circuit inductance were recorded and used in margin analysis simulations while the coil currents were gradually increased, at each stage. The varied currents represent different magnetic field density magnitudes the circuit could be exposed to.

In addition, the SFQ cells were simulated with field coil currents that vary both negatively and positively, thereby effectively reversing the magnetic field orientation in each coil and fix it for each simulation. This approach produced two OFMs, one for the positive field and the other, for the negative field. These OFMs cannot be necessarily the same as the circuit inductance orientation and position can influence the results. This is a thorough approach and remains indicative at best, but a good shield has to provide protection from all possible field vectors. At any given time, all coils have the same amount of current. Consequently, the vector sum of the resulting fields has an inclination, $\theta \approx 55^\circ$ and azimuth, $\varphi \approx 45^\circ$ in a spherical coordinate system, as also shown in Section 2.3.4.

The current density calculations, shown in Fig. 3.9 were done all around the cell, however, only the top part is shown here. The current density is highest in the coils (red) and affects the cell due to coupling. The current density plots were generated with *Magix*, a visualization tool for *InductEx* that produces files viewable with *ParaView* [50]. In the simulations, a 1 volt sinusoidal voltage at 10 GHz is applied to each coil, resulting in a maximum current density of $\approx 1.75 \times 10^{+10} \text{ A/m}^2$. Radii of coils are $R_{xy}=125 \mu\text{m}$, $R_{yz}=130 \mu\text{m}$ and $R_{xz}=135 \mu\text{m}$. To further validate the effectiveness of the grid shield, current densities were calculated at the indicated points shown in Fig. 3.9 [76].

Fig. 3.9 shows current density plots of a DC-SFQ cell surrounded by 3 orthogonal coils, for both the unshielded and standard grid shielded cases. The results reported in Fig. 3.9 brings up a more quantifiable approach towards the calculation of shielding effectiveness than the one reported in Fig. 3.6. The red colour shows the highest current density, while blue is lowest. With the aid of the colour field magnitude key in Fig. 3.9, the colour variations show that the grid shield reduces the density on the DC-SFQ cell that occurs due to coupling with the 3 coils. By calculating current densities at the nine points shown in Fig. 3.9, on both the unshielded and shielded DC-SFQ cells, the grid shield reduces the current density on the DC-SFQ. The results for the calculated current densities are graphically shown in Fig. 3.10. Comparatively, the grid shield reduces the current density $\approx 40\%$. The grid shield was only

implemented in the topmost layer of the *Hypres'* 4.5 kA/cm^2 fabrication process for all the simulations presented. This approach leaves the ground plane unmodified to avoid other design challenges that might arise because of additional changes of circuit inductances.

The ground contacts in Fig. 3.11, marked GND, were placed to provide the best possible shielding and lowest drop on circuit inductance. It was observed that grounding contacts laid out in a line that crosses circuit inductance at 90° resulted in lower drop in circuit inductance, while those laid out in parallel to circuit inductance resulted in a higher drop. A detailed analysis on shield grounding is reported in Chapter 4.

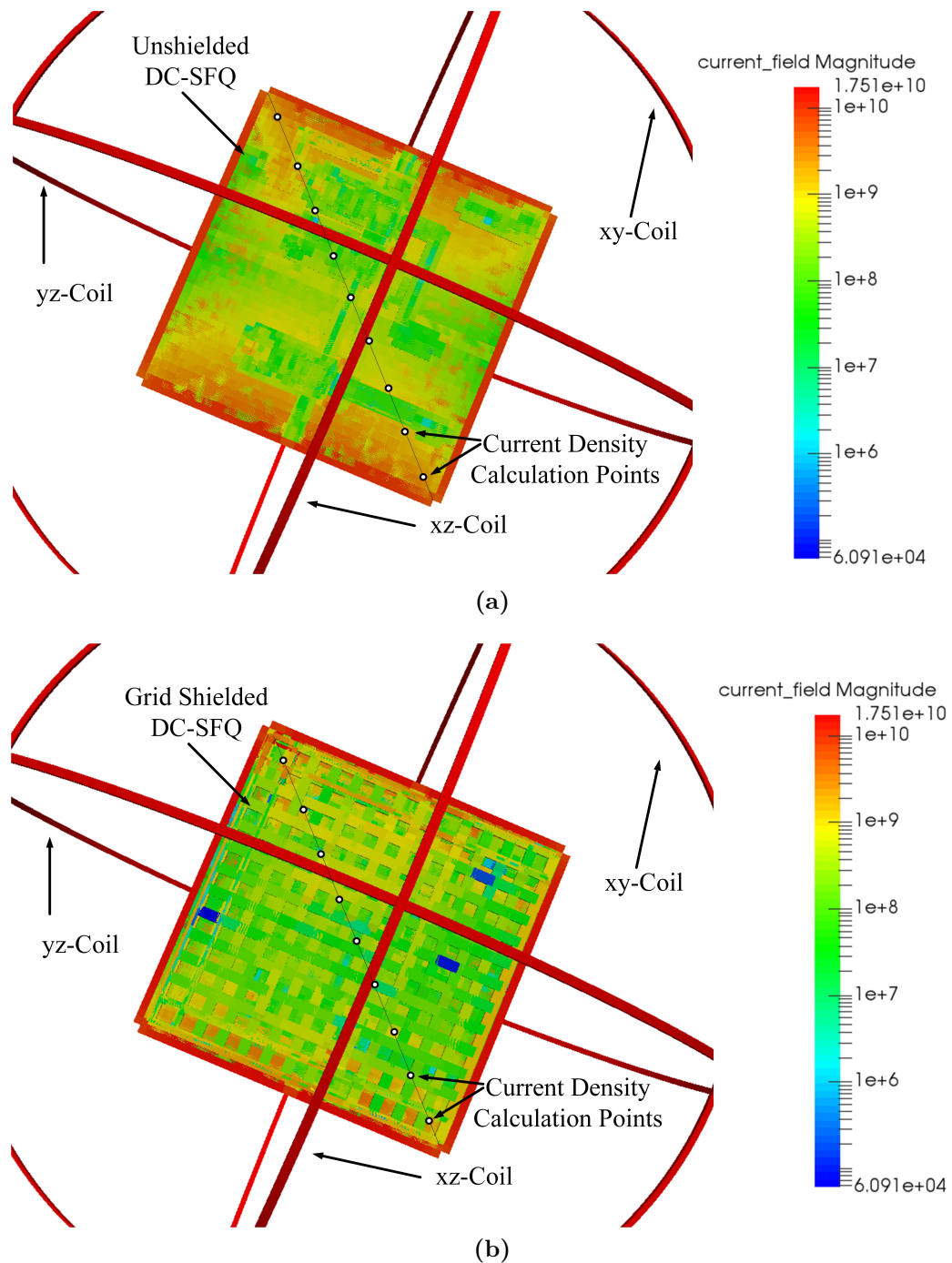


Figure 3.9: Current density plots of a DC-SFQ surrounded by 3 orthogonal coils, (a) unshielded and (b) under a standard grid shield

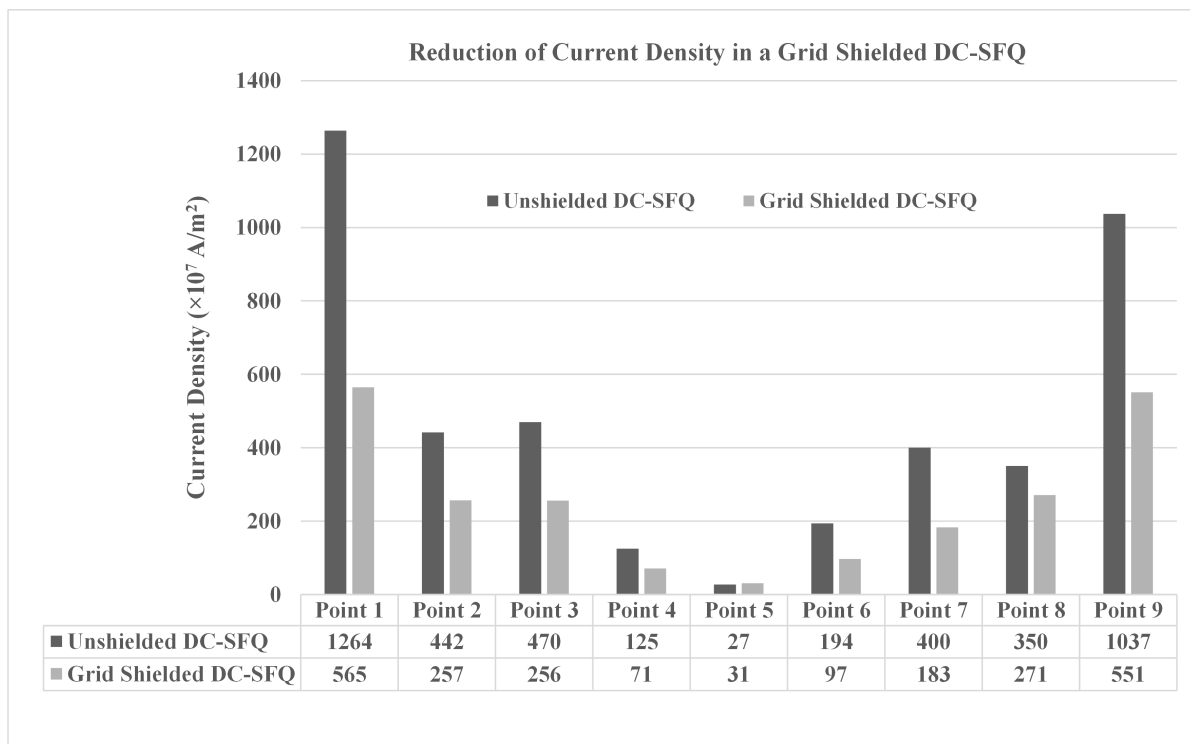


Figure 3.10: A bar graph showing the reduction of current density, due to external magnetic field, in a shielded DC-SFQ Cell, compared to the unshielded case

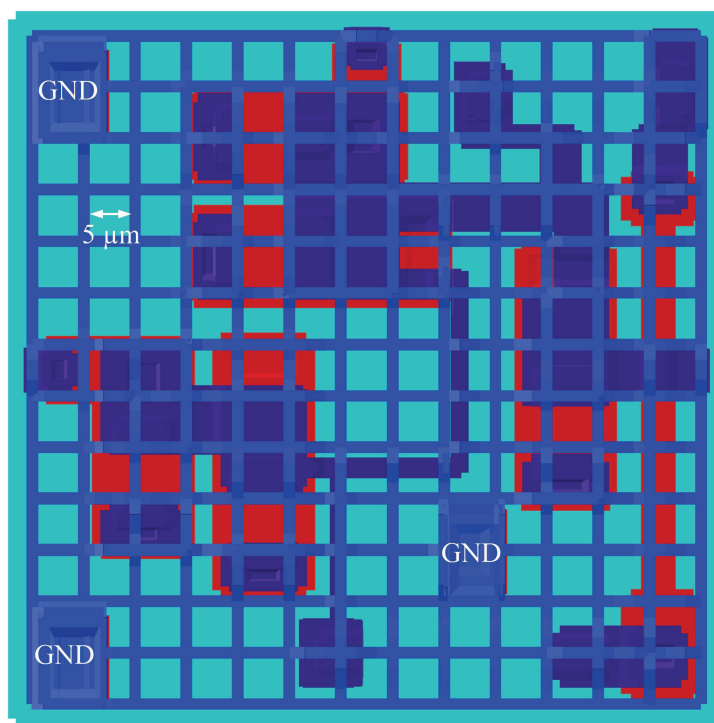


Figure 3.11: A DFF covered in a grid patterned shield - each grid bar is $2.5 \mu\text{m}$ wide and are spaced $5 \mu\text{m}$ from each other. The layout was done in the *Hypres'* $4.5 \text{ kA}/\text{cm}^2$, in which the layer, M3, with fixed thickness $d = 600 \text{ nm}$ was used to make the grid shield.

3.5.2 Effect of Grid Spacing on Shielding Effectiveness and Circuit Inductance

In this analysis, simulations for both the DFF and DC-SFQ were conducted to determine the effect of grid bar spacing on shielding effectiveness [76]². Grid bar spaces of 0, 2.5, 4, 5, 6, 7.5, 9 and $10 \mu\text{m}$ were used in the analysis. The bar width of each grid was fixed to $2.5 \mu\text{m}$ for all grid spaces. An example of grid shield is shown in Fig. 2.4. At this point, each grid shield configuration was simulated and

²This discussion is part of already published material by the author [76]

OFMs recorded for each cell. The results are summarised in Fig. 3.12, where it shows that the shielding effectiveness reduces with increase in spacing between grid bars. The smaller the spaces, the better the shield. As the spaces become wider, coupling between circuit and external coils increases, leading to poorer shielding. However, it can also be noted from Fig. 3.13, that the overall influence on circuit inductance reduces when increasing the spacing of the grid bars from 0 to $7.5 \mu\text{m}$. Any further increase in the spacing beyond $7.5 \mu\text{m}$ produces no further drop in circuit inductance. It shows that even the widest possible grid bar spacing can cause a drop in circuit inductance of about 10% (observable in Fig. 3.13). It is at the discretion of the circuit designer on how much magnetic shielding can be applied without sacrificing parameter and bias margins due to the drop in circuit parameter values.

The OFMs in Fig. 3.12 can be compared to unshielded cases for both cells. The OFMs for the unshielded DFF were $46 \mu\text{T}$ and $38 \mu\text{T}$ [58] for positive and negative currents, respectively, while for the unshielded DC-SFQ the OFMs were $63 \mu\text{T}$ and $38 \mu\text{T}$ for positive and negative currents, respectively.

A grid shield of $2.5 \mu\text{m}$ wide bars and $5 \mu\text{m}$ spacing offers the best compromise at OFMs of $98 \mu\text{T}$ for positive current and $50 \mu\text{T}$ for negative current (refer to Fig. 3.12(a)) in the DFF. Whereas for the DC-SFQ under the same grid shield dimensions produced OFMs of $117 \mu\text{T}$ and $67 \mu\text{T}$ for positive and negative current respectively (see Fig. 3.12(b)). In comparison, the OFMs for solid shield covered cells were $86 \mu\text{T}$ and $50 \mu\text{T}$ [58] in the DFF and $113 \mu\text{T}$ and $59 \mu\text{T}$ in the DC-SFQ.

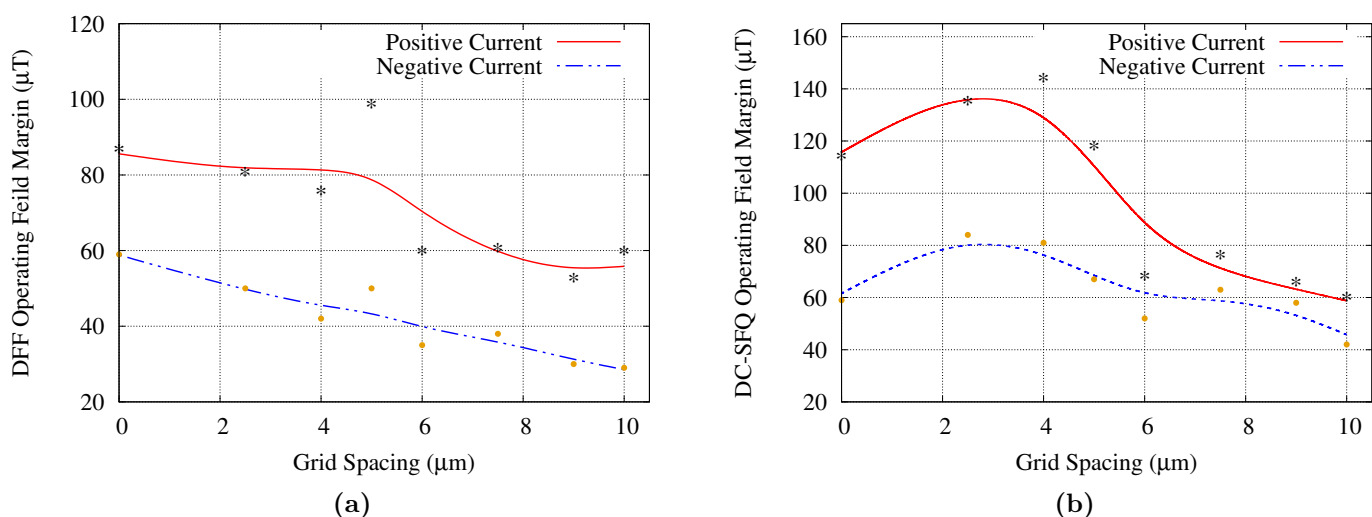


Figure 3.12: The variation of shielding effectiveness with changing grid spacing - A grid shield with smaller spaces offers better shielding, but the downside is that the circuit inductance are affected to the point that re-optimisation of the entire circuit might be necessary and vice-versa. Positive and negative currents refer to fields from coils.

The percentage inductance drop for the grid shield with $2.5 \mu\text{m}$ grid bar width and $5 \mu\text{m}$ spacing are 8 % and 11 % for the DC-SFQ and DFF respectively, as shown in Fig. 3.13. In comparison, the drop is quite high when a solid shield is used with 21 % in the DC-SFQ and 25 % in the DFF. Such high variations can negatively impact operating margins if redesigning and optimization are not done. However, the parameter variations for the grid shield with $2.5 \mu\text{m}$ grid bar width and $5 \mu\text{m}$ spacing showed to have minimal effect on operating margins of the cells. Another advantage of the grid shield is that the bar width has been chosen narrow enough to limit flux trapping, which is the origin of some noise and digital malfunctions in SFQ circuits. Unlike in the case of the solid shield, flux trapping is unlikely to occur in the bars or the grid holes (as also shown in [77] Section 5.4, pp. 43-45).

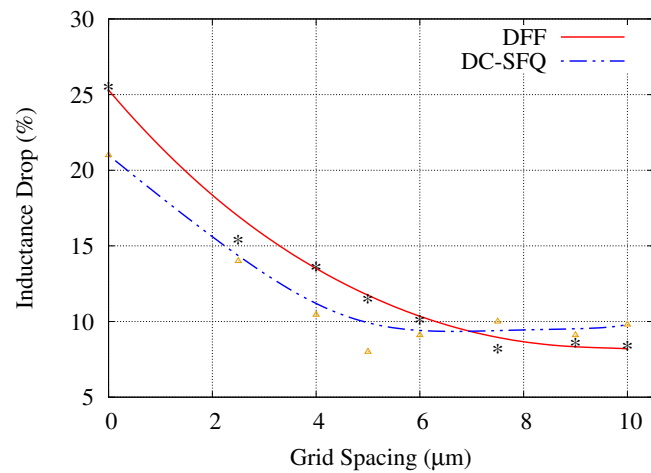


Figure 3.13: Percentage inductance drop against variations in grid spacing in both the DFF and DC-SFQ

3.6 Chapter Conclusion

The theory behind shielding is a window into the possibility of using superconductors as shields in SFQ circuits. However, the challenge with SFQ circuit shielding is that only superconducting thin films can be used as shields. Shielding works better if the shielding material is thick enough and yet the films in SFQ circuits are very thin and fabrication technology dependent. Nonetheless, two shielding approaches were discussed and analysed: the conventional solid shield and the novel grid shield. Fundamental design issues related to the two types shields were presented. The spacing between grid bars has shown to affect the shielding effectiveness and that there is still a notable drop in circuit inductance when a grid shield is used. However, the drop in inductance is less, in the grid, than what the solid shield imposes.

Chapter 4

On-Chip Shielding Design Considerations

4.1 Introduction

This chapter presents three design issues that affect the effectiveness of an on-chip SFQ shield. The discussion presented here focuses on the following three issues:

1. The effect of grounding contact positions on shielding effectiveness, in which both the grid and solid shield are analysed with magnetic fields from all three coils, one at a time.
2. The effect of grid bar spacing on the shielding effectiveness of a uniformly and sporadically grounded SFQ cell.
3. The effect of a rotated magnetic field, produced with 3-D coils, on the operation of an unshielded, grid or solid shielded DFF and DC-SFQ cells.

The analysis has yielded design figures that can aid in the design of suitable shields for SFQ circuits. Though specific to the DFF and the DC-SFQ cells used, the analysis approach can be adopted to aid in the shielding design for any SFQ cell.

4.2 Effect of ground contact positioning on shielding effectiveness

In this section, both the grid and solid shields were investigated to determine the best possible placement of shield layer to ground plane contacts. In the grid shield, the bars were fixed to a width of $2.5 \mu\text{m}$ and spacing of $5 \mu\text{m}$. Four configurations of the ground contacts were considered and hereby named *Grid1*, *Grid2*, *Grid3* and *Grid4*. The grounding configurations were defined as depicted in Fig. 4.1 and Fig. 4.2. The configurations are shown with the grid shield only, but the same configurations were used in the simulations with the solid shield. In this case, the shields are called *Solid1*, *Solid2*, *Solid3* and *Solid4* and they correspond to the ones in the grid shield.

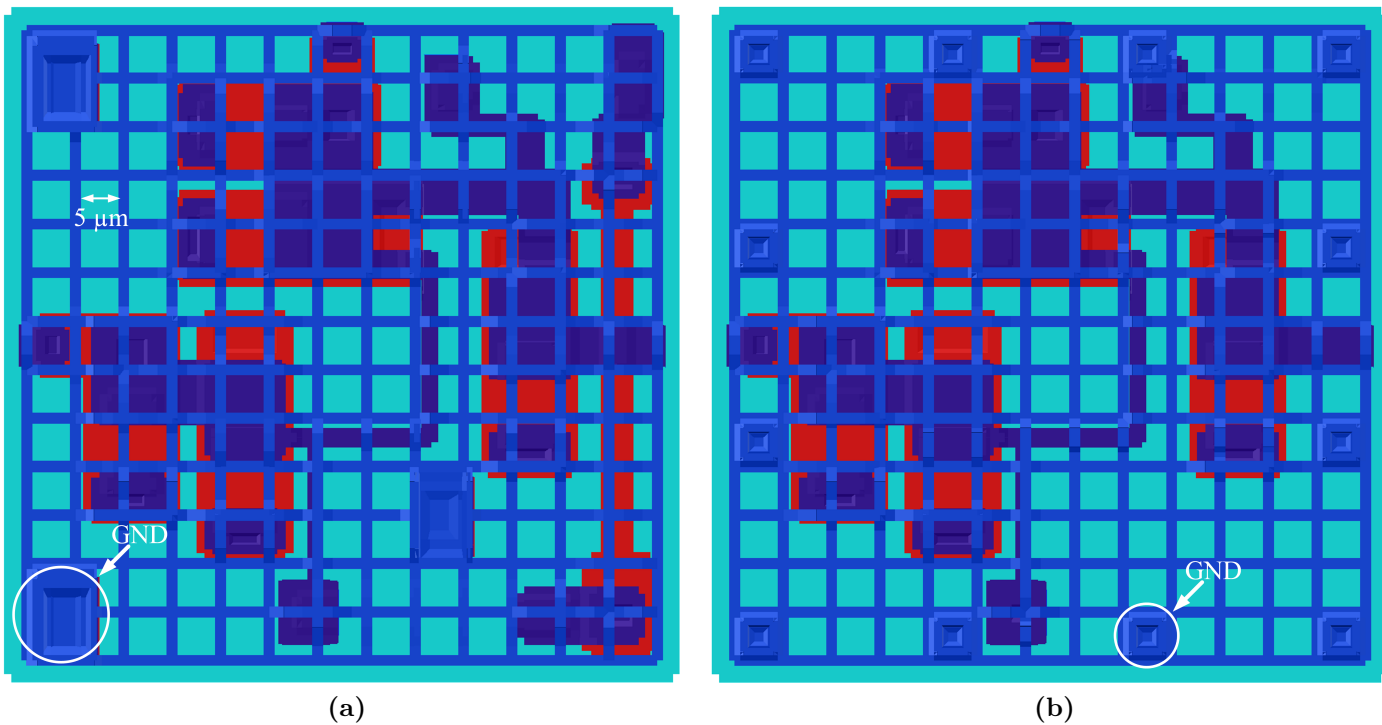


Figure 4.1: (a) *Grid1* grounded at 3 points only by taking advantage of the available spaces after initial layout and (b) *Grid2* with 12 ground contacts at specifically chosen positions. For *Grid2*, some circuit elements had to be moved around to accommodate the uniform ground contact placement.

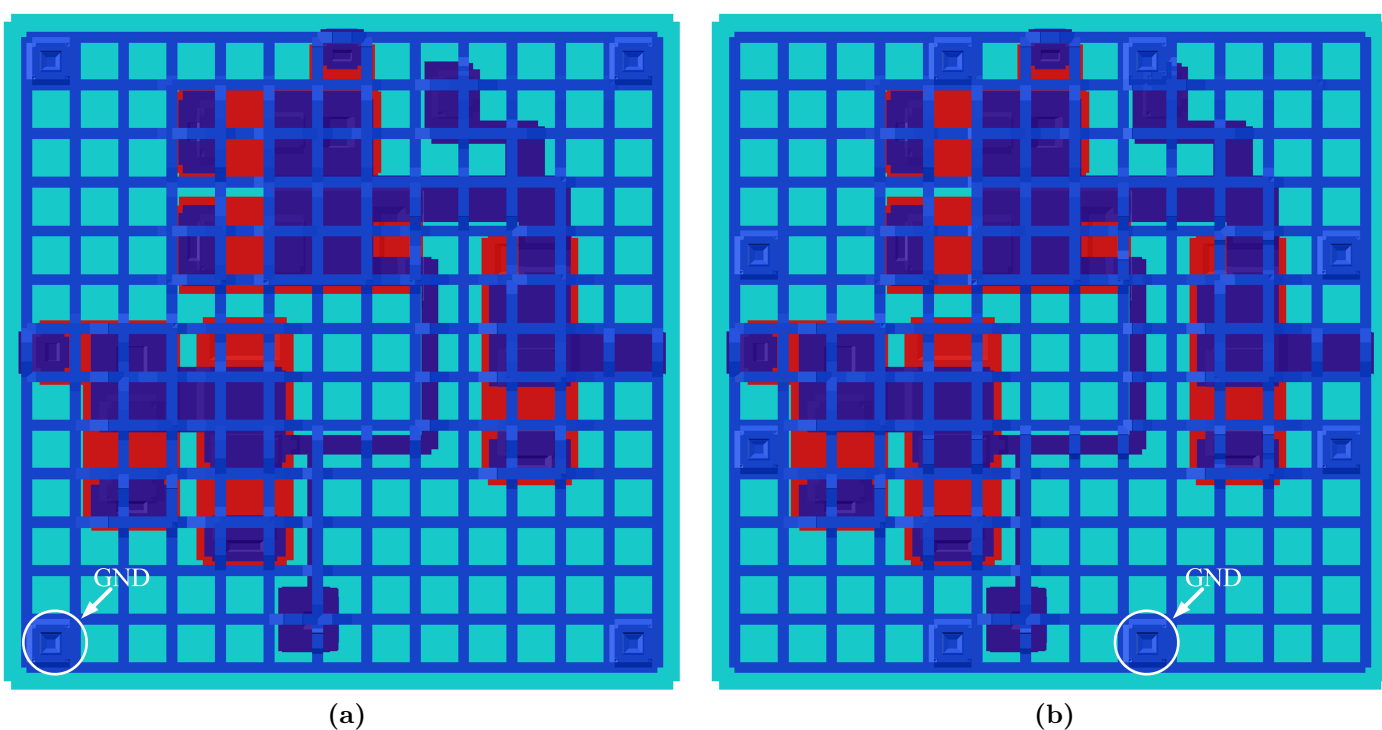


Figure 4.2: (a) *Grid3* grounded at 4 points, one at each corner of the cell, (b) *Grid4* with 8 ground contacts at positions close to and in-line with input/output locations on the cell.

4.2.1 Simulations and Results

For each grid grounding type, the OFMs were obtained for each coil, one at a time. As a result, each grounding type has six OFMs reported, of which three are for +OFMs and another three for -OFMs. To obtain a better comparison, the simulations were also done for the solid shield using the same grounding types. Each of the 3 coils was fixed to a diameter of 125 μm. The process used in the calculation of OFMs is the same as reported in Chapter 2, Chapter 3 and Appendix A. The simulations were done for both negative and positive coil currents, resulting in both -OFMs and +OFMs. In the simulation

results, the unshielded DFF case was incorporated as a reference to show if the shields improved the OFMs of the cell.

4.2.1.1 Grid Shield

The simulation results for the grid shielded DFF are summarized in Table 4.1. The simulation results show that the *Grid4* layout offers the best and widest OFMs, closely followed by *Grid2*. The grounding configuration in *Grid4* and *Grid2* create a strong virtual shield layer that aids good flow of surface currents, especially because the ground contacts are located very close to the circuit elements. The implication is that there is a slightly larger drop in circuit inductance compared to the other grounding configurations. These results are similar to those reported in [20, 74], even though the reported results were based on less complex circuits that included strip lines and two Josephson junction superconducting quantum interference devices (SQUIDs). On the overall, the grid shield performs lowly against perpendicular fields from the *xy* coil, due to the gaps that are inherent in the grid.

Coil	Operating Field Margins (OFMs) (μT)									
	Unshielded		<i>Grid1</i>		<i>Grid2</i>		<i>Grid3</i>		<i>Grid4</i>	
	-OFM	+OFM	-OFM	+OFM	-OFM	+OFM	-OFM	+OFM	-OFM	+OFM
xy	28	30	57	69	69	71	62	67	68	71
xz	87	80	172	146	177	360	234	180	190	389
yz	90	68	168	125	216	290	184	134	209	289

Table 4.1: OFMs for each ground type in the grid shield

4.2.1.2 Solid Shield

The solid shield showed superior performance against perpendicular fields, those from the *xy*-coil as summarized in Table 4.2. The continuous superconducting layer significantly reduces coupling between the *xy*-coil and circuit inductances. In return the shield, coupled with ground contacts of any configuration provides easy flow of shielding currents, thereby improving shielding for fields of perpendicular orientation. The overall performance of the grounding configurations shows that *Solid1* and *Solid3* have higher OFMs compared to the rest. It was also noted that the solid shield provides better protection if the ground contacts are few and no particular pattern is requisite as shown in *Solid1*.

Coil	Operating Field Margins (OFMs) (μT)									
	Unshielded		<i>Solid1</i>		<i>Solid2</i>		<i>Solid3</i>		<i>Solid4</i>	
	-OFM	+OFM	-OFM	+OFM	-OFM	+OFM	-OFM	+OFM	-OFM	+OFM
xy	28	30	745	462	633	429	557	531	665	420
xz	87	80	111	213	63	90	142	178	67	93
yz	90	68	126	165	81	75	141	242	86	80

Table 4.2: OFMs for each ground type in the solid shield

Comparatively, the solid shield is suited for keeping out perpendicular magnetic fields, while the grid shield provides superior protection against in-plane magnetic fields. In some cases, such as *Solid2* and *Solid4*, the solid shield's OFMs against in-plane fields were worse than in the unshielded case. The solid shield, though superior against perpendicular fields, may not be suited for some applications as it introduces a high reduction in circuit inductance as reported earlier. However, this drawback could be averted by re-designing the circuit inductances affected. If the shielding required is only against the

Earth's ambient magnetic field, both the grid and solid shields, with the most superior grounding method, would be adequate. The results in Table 4.1 and Table 4.2 show that these shields meet the minimum requirement, since the reported maximum magnetic field of the Earth does not exceed $65 \mu\text{T}$ [10].

4.3 Effect of Grid Bar Spacing on Uniformly and Sporadically Grounded Shields

The effect of grid bar spacing on shielding effectiveness was investigated in Section 3.5.2. In that analysis, a 3-D coil system, that integrates the fields from all three coils, was used. The orientation of the resultant magnetic field, from the 3-D coil system, was fixed by the currents in each of the three coils. At that stage, it was still unknown how grid bar spacing could affect the shield's effectiveness, against fields from the fundamental x , y and z directions. Hence, the investigation into the effect of spacing between grid bars on the shielding effectiveness using magnetic fields from the three coils, one at a time, had to be done. In this case, two shield grounding techniques were used: uniform and sporadic grounding. Hence, the analysis also served as a way to assess the effect of grid bar spacing on each of the DFFs with the aforementioned grounding types. A DFF covered by a grid shield with uniform grounding as reported in Section 4.2 was investigated first, followed by another with a sporadically grounded grid shield.

4.3.1 Uniformly grounded grid shield for a DFF

The DFF was laid out under a grid shield with uniform grounding as shown in *Grid4* (as explained in Section 4.2). The uniformly grounded shield has shown to provide a consistent flow of return and shielding currents on both the bottom, solid shield (ground plane) and the top shield (the grid). Here, the effect of varying the spaces between grid bars on the shielding effectiveness in a uniformly grounded shield is presented. The challenge is that even though superior shielding can be realized, there is a significant resultant drop in circuit inductance as the shielding effectiveness improves. This requires that the affected circuit inductances be altered in the original layout.

Fig. 4.3(a) shows the OFMs of the DFF when exposed to magnetic fields from the xy -coil. It was observed that the shielding is very good at a spacing of $0 \mu\text{m}$ (i.e. Solid shield). However, the actual variation in OFMs is observed as the grid bar spacing is varied, as shown in Fig. 4.3(b). As shown in Section 3.5.2, the OFMs are lower than those for the solid shield. The OFMs for both negative and positive currents are almost identical. This is due to the perpendicular nature of the xy -coil fields and the uniform placement of ground contacts that result in the uniform distribution of currents in the ground plane and the shield.

The OFMs of the DFF against xz -coil fields are shown in Fig. 4.4. In this case, the DFF has much lower OFMs compared to those against the xy -coil fields at spacing of $0 \mu\text{m}$. The xz -coil produces fields that are parallel to the plane of the DFF. Therefore, more detrimental to its operation as also established in [6]. In Fig. 4.4(b), the dependency of the OFMs on the spacing between grid bars can still be observed. For fields from the yz -coil, depicted in Fig. 4.5, the DFF has fairly uniform OFMs for the grid, with the exception when the grid bars become much wider apart, at $10 \mu\text{m}$ for the negative current. Like the response to xz -coil fields, the solid shield has the lowest OFMs. Therefore, the solid shield is unsuitable to shield SFQ circuits against in-plane (parallel) external magnetic fields. However, apart from the disadvantage of reducing the values of circuit inductance, the solid shield is well suited against perpendicular external magnetic fields, such as those produced by the xy -coil.

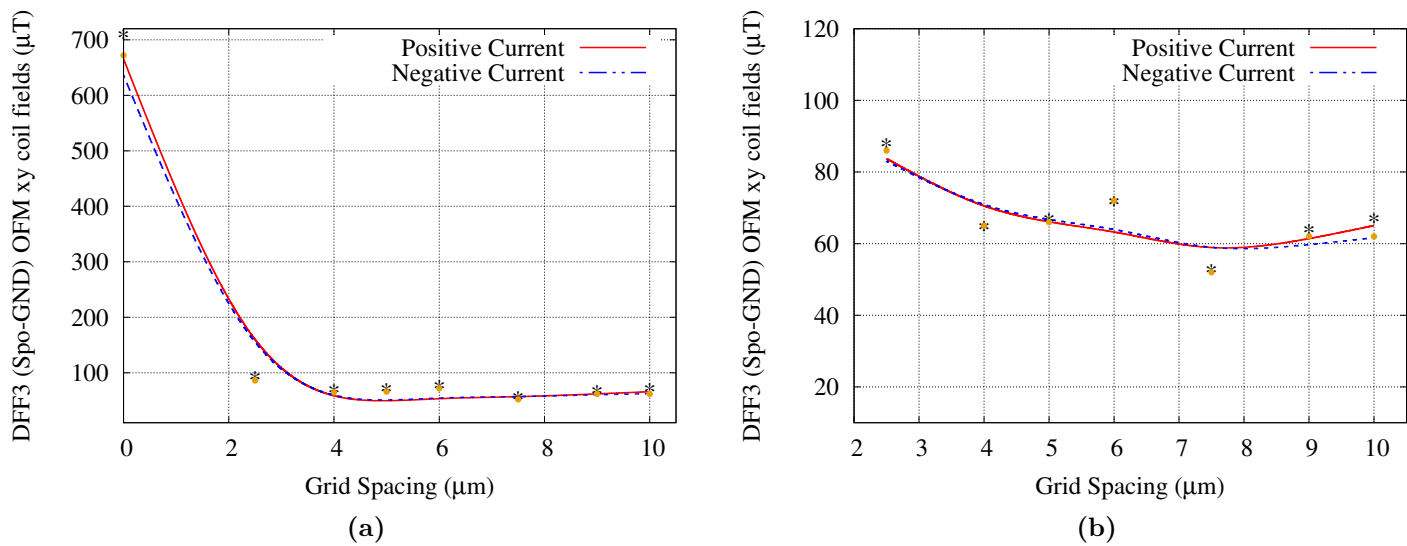


Figure 4.3: OFMs of a uniformly grounded DFFs against grid bar spacing for magnetic fields from the xy -coil, (a) from 0 μm spacing and (b) from 2.5 μm spacing.

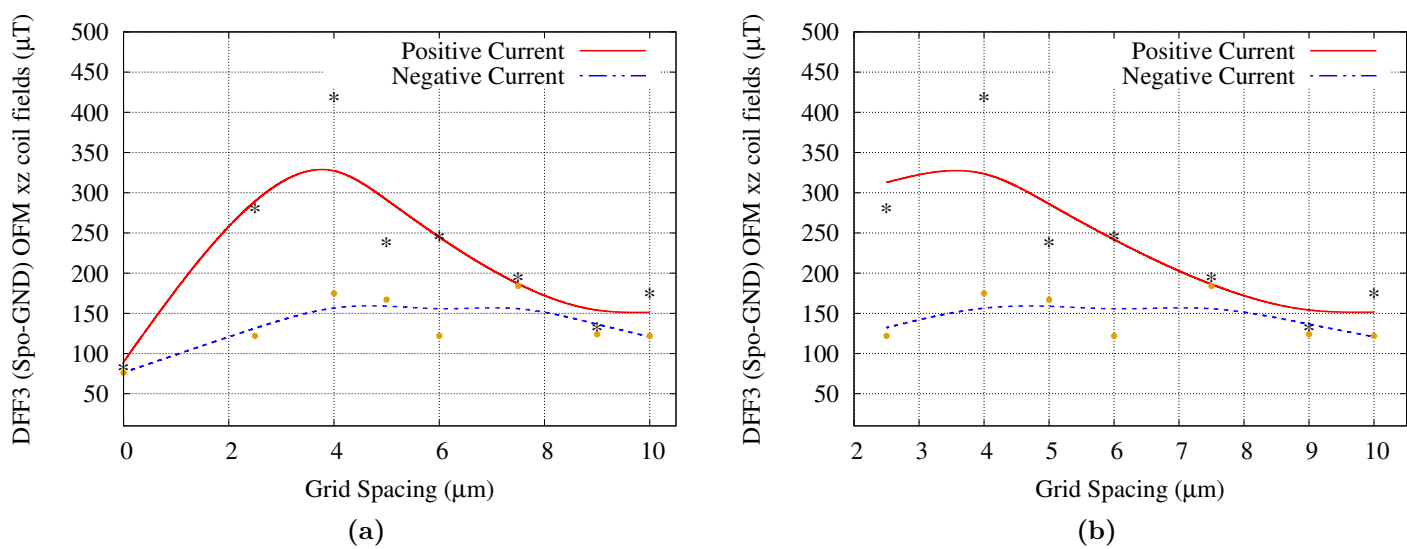


Figure 4.4: OFMs of a uniformly grounded DFFs against grid bar spacing for magnetic fields from the xz -coil, (a) from 0 μm spacing and (b) from 2.5 μm spacing.

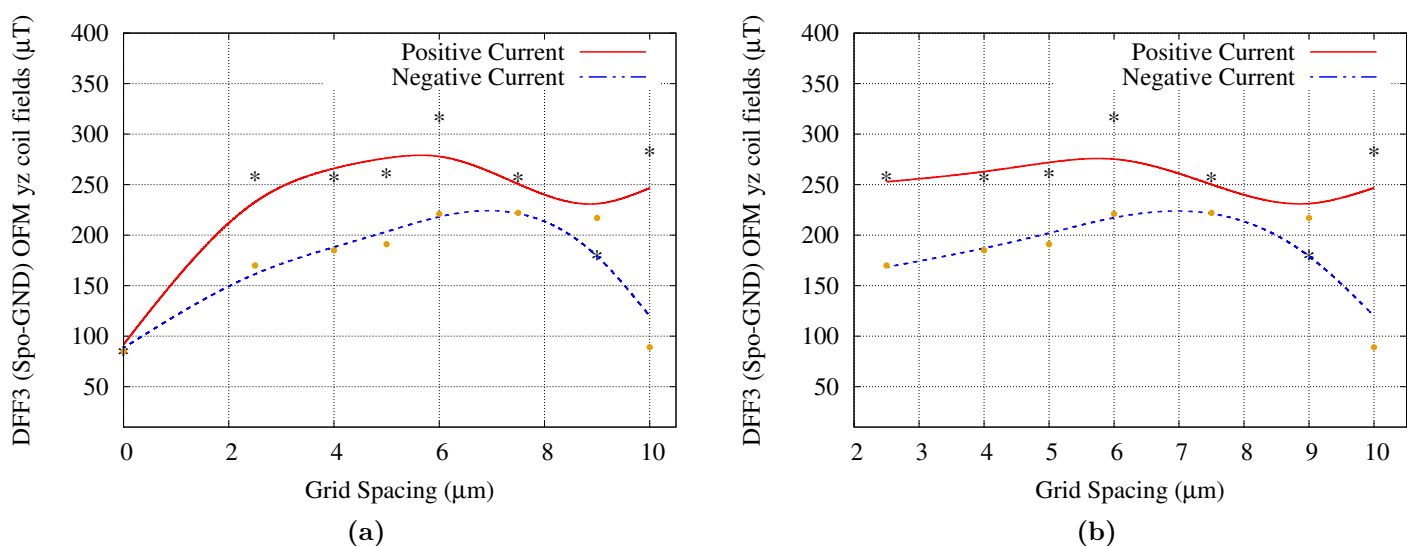


Figure 4.5: OFMs of a uniformly grounded DFFs against grid bar spacing for magnetic fields from the yz -coil, (a) from 0 μm spacing and (b) from 2.5 μm spacing.

A further analysis of the results shows that the magnetic field from the xy -coil places an upper bound on the uniformly grounded grid shield's OFMs. As such, regardless of orientation, the grid shielded DFF

can withstand magnetic fields of up to $88 \mu\text{T}$ at a grid bar spacing of $2.5 \mu\text{m}$. However, if the xy -coil field is excluded or unavailable by proper positioning of the cell, the critical OFM is determined by the xz and yz -coil fields at about $250 \mu\text{T}$ for positive current generated fields and $150 \mu\text{T}$ for negative generated fields. The difference in the figures is due to the asymmetrical layout of the DFF and the finite ground plane, only at the bottom of the cell, that provides a return path for both shielding and return currents. For the uniformly grounded solid shield, at a space of $0 \mu\text{m}$ in Fig. 4.3, Fig. 4.4 and Fig. 4.5, the overall OFM is about $90 \mu\text{T}$ dictated by the fields in xz and yz -coils. The solid shield is superior against xz -coil field with an OFM of about $650 \mu\text{T}$.

4.3.2 Sporadically grounded grid shield for a DFF

The number of ground contacts can be reduced and laid out sporadically to reduce the return current in the shield layer, in the grid or solid form. The grid shield grounding scheme used for this work is similar to *Grid1* (illustrated in Fig. 4.1). In Fig. 4.6 the OFMs for the solid shield are slightly lower than those shown in Fig. 4.3 for the uniformly grounded DFF. However, there is a remarkable difference between the OFMs for negative and positive coil currents. This is the case because the uniformly grounded shield improves shielding effectiveness through the many current loops that aid the efficient flow of shielding currents.

Variations in OFMs for both xz and yz -coils are depicted in Fig. 4.7 and Fig. 4.8, respectively. In both cases, the solid shield has higher OFMs than those for the uniformly grounded DFF reported in Section 4.3.1. In addition, negative coil currents have higher OFMs than the ones for the positive coil currents in the uniformly grounded case. This can be attributed to the reduced currents that flow on the shields due to the fewer and sporadically laid out ground contacts. However, on the overall, the uniformly grounded DFF has higher OFMs, which makes it a better shield. The accompanying challenge is that there is a higher reduction in circuit inductance when the uniformly grounded shield is used. Reduction in OFMs with increased spacing between grid bars is observed in both the uniformly and sporadically grounded DFFs.

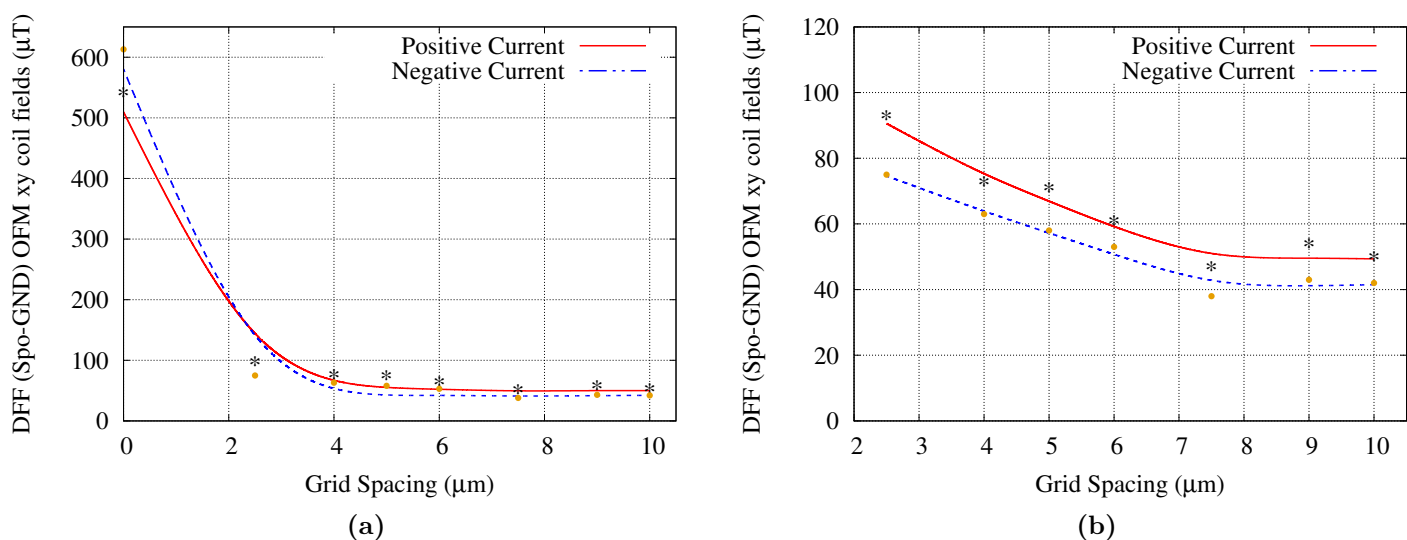


Figure 4.6: OFMs of a sporadically grounded DFFs against grid bar spacing for magnetic fields from the xy -coil, (a) from $0 \mu\text{m}$ spacing and (b) from $2.5 \mu\text{m}$ spacing.

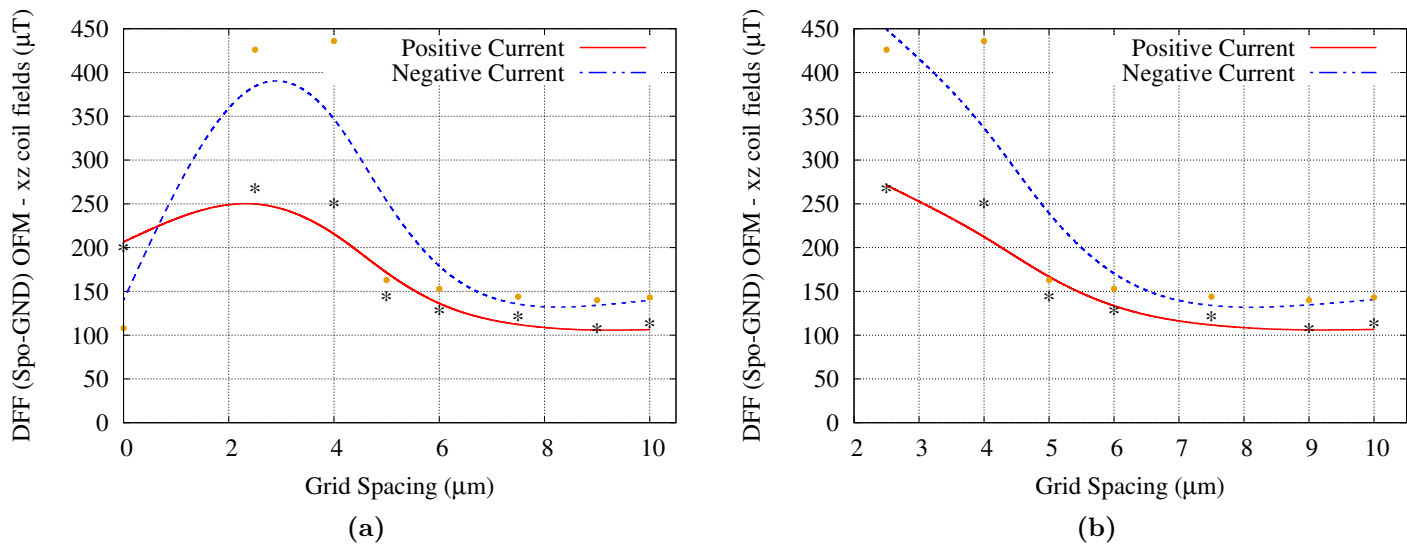


Figure 4.7: OFMs of a sporadically grounded DFFs against grid bar spacing for magnetic fields from the xz -coil, (a) from 0 μm spacing and (b) from 2.5 μm spacing.

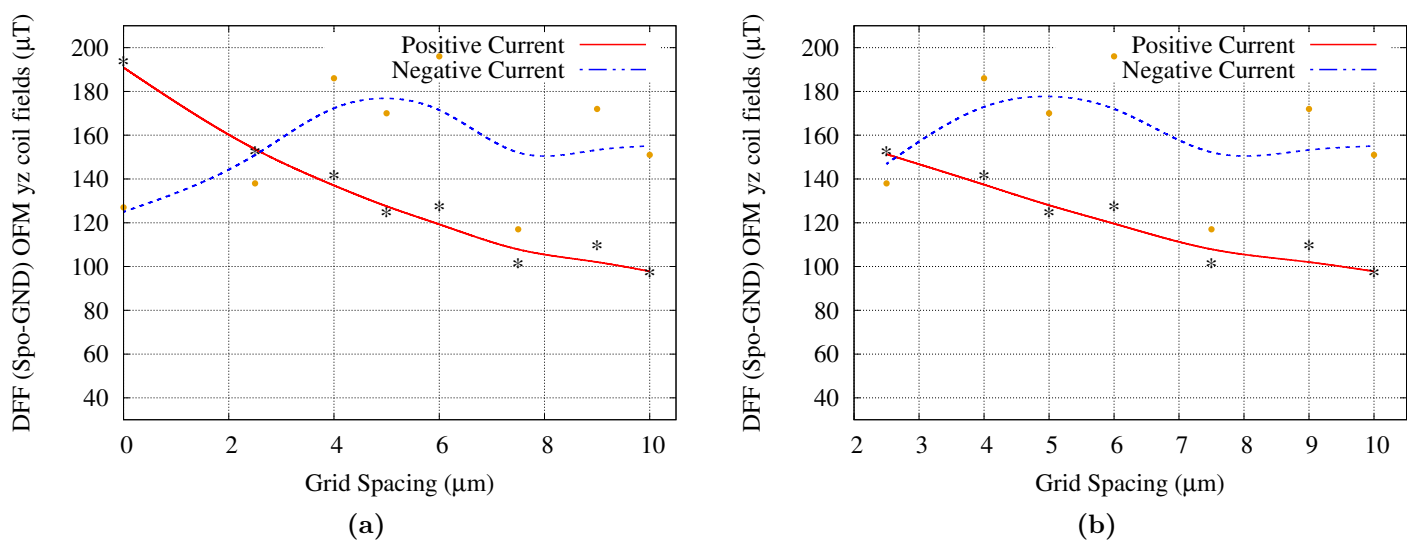


Figure 4.8: OFMs of a sporadically grounded DFFs against grid bar spacing for magnetic fields from the yz -coil, (a) from 0 μm spacing and (b) from 2.5 μm spacing.

Similar to the uniformly grounded case, the sporadically grounded DFF's overall OFMs, regardless of field orientations, are limited by the OFMs in the xy -coil case at about 80 μT . However, the OFMs from the xz and yz field orientations vary without a definitive pattern.

If the OFMs in the uniform and the sporadic grounding case were compared, it can be concluded that a uniformly grounded shield provides more predictability in the performance of the shield. With the uniform grounding, it becomes easier to predict how the shield could perform in different magnetic field densities, at a specific grid bar spacing.

4.3.3 Shield and Ground Plane Current Distribution

Sporadic grounding ensures that the currents on the shield surface and ground plane are unequal. This has a double implication, that is if more current flows on the shield, then a larger reduction in circuit inductance occurs. However, if more current flows in the ground plane, then larger magnetic fields could be created that could eventually affect circuit operation. As suggested in [11] and inferred in [78], the effects can be reduced by drawing out the return currents from the ground plane at strategic positions

that enable a reduction in the magnetic fields at the most vulnerable elements of an SFQ circuit. Shielding provides another return path for circuit's bias currents. Therefore, it has the potential to reduce the currents in the ground plane. Contrary, uniformly grounded shields provide equal distribution of such currents. The circuit designer has to decide on the compromises required and the subsequent effect on circuit operation, both primary (bias margins) and secondary (magnetic field tolerance).

4.3.4 Points To Consider

The ground contacts used in Section 4.3.1 are of $140 \mu\text{m}^2$ size while those used in Section 4.3.2 have a $25 \mu\text{m}^2$ size. Even though the size of the ground contact has minimal effect on OFMs, the smaller contacts are preferred because there would be less flux trapped in them unlike when they are made larger.

The layout of the grid is in such a way that it could be looked at as a series of square moats in the shielding layer. In some cases, the grid layout would expose an inductor at a lower grid spacing while covering the same at a higher grid spacing. The implication is that, the sparsely laid out grids would give a slightly higher OFM than the closely laid out grid bars. In addition, the inductor under a grid bar would report a higher reduction in its inductance even at a wider grid bar spacing. This can be corrected by laying out a grid shield that is irregular and made not only from squares, but also other rectangular shapes according to the designer's requirements. An illustration for this is shown in Fig. 4.9.

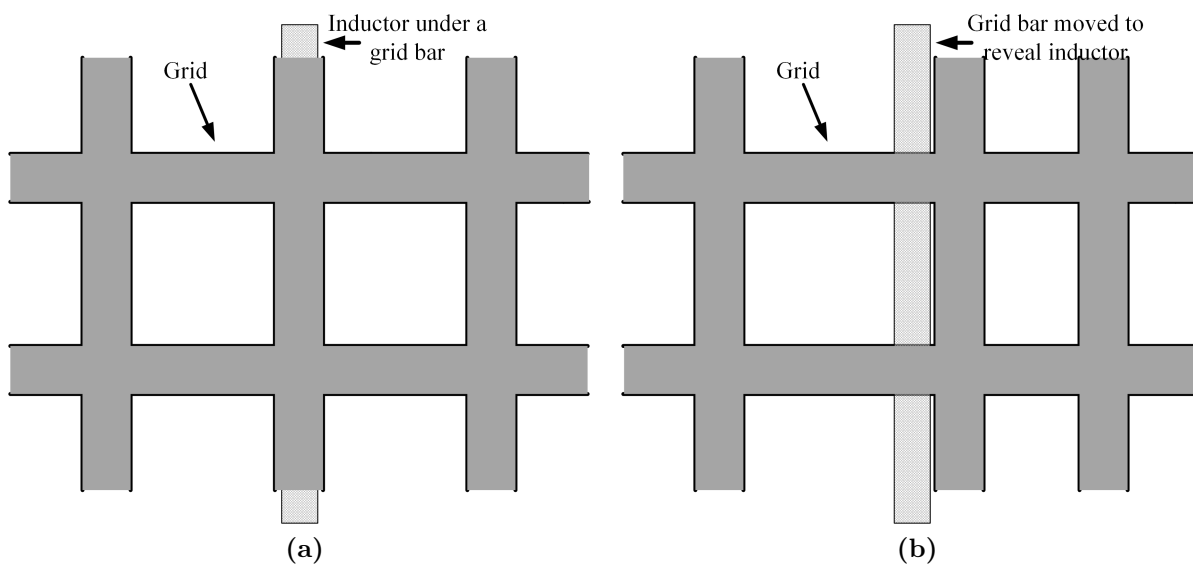


Figure 4.9: Different grid shield scenarios (a) a circuit inductor laid out under a bar for a uniform grid shield and in (b) a non-uniform grid shield created specifically to remove the inductor from under a grid bar. The effect on the shielding efficiency is very small, but the inductor's value is restored to the design value.

4.4 Further Shielding Analysis with Inclined Magnetic Fields in 3-D

In the preceding chapters, analysis and validation of both the novel grid shield and solid has been done with either a 3-D coil system or each orthogonal coil separately. This gives us a finite number of options regarding the orientation of the external magnetic fields. The magnetic field can be rotated, in terms of predefined orientation angles in 3-D space. By altering the direction or magnitude of current in each

coil, the resultant magnetic field from the three coils can be rotated as a result. In this chapter, seven predefined orientations were used to analyse both the DFF and DC-SFQ for unshielded, grid and solid shielded variants. These predefined directions are shown in Table 4.3. All coil currents are meant to be of equal magnitude, however, this does not happen as the coil sizes are not equal to provide isolation between them. Hence, coil diameters of 125, 130 and 135 μm were used in the simulations. I_{xy} , I_{xz} and I_{yz} are simulation currents that flow in the xy , xz and yz coils, respectively. Due to the slight differences in the coil diameters, the produced magnetic fields are not exactly the same. However, this can be rectified by changing the magnitudes of coil currents in line with the coil radii. By making one or two of the coil currents negative, the orientation of the resultant magnetic field changes. The shields in both cells were sporadically grounded as depicted in Fig. 4.1(a). The orientation of *Type 1* has been shown before in Fig. 2.14.

Type	xy	xz	yz
1	I_{xy}	I_{xz}	I_{yz}
2	$-I_{xy}$	I_{xz}	I_{yz}
3	I_{xy}	$-I_{xz}$	I_{yz}
4	I_{xy}	I_{xz}	$-I_{yz}$
5	$-I_{xy}$	$-I_{xz}$	I_{yz}
6	I_{xy}	$-I_{xz}$	$-I_{yz}$
7	$-I_{xy}$	I_{xz}	$-I_{yz}$
8	$-I_{xy}$	$-I_{xz}$	$-I_{yz}$

Table 4.3: Types of magnetic field orientations determined by the directions of coil currents in the xy , xz and yz coils.

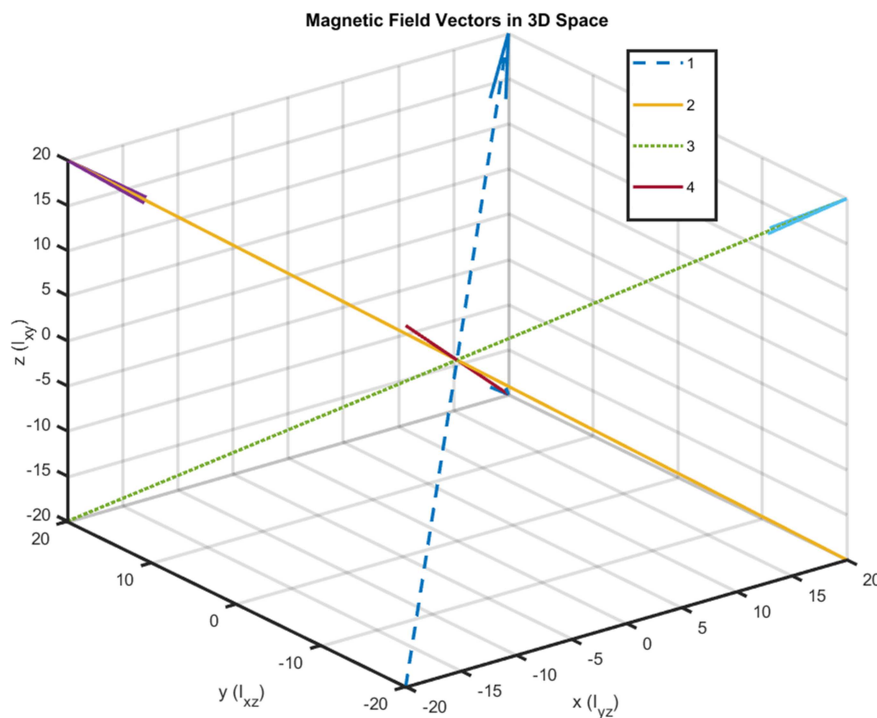


Figure 4.10: Magnetic field vectors in 3-D space corresponding to Type 1, 2 3 and 4 in Table 4.3. The other orientations are simply 180° phase shift versions of the vectors here, as follows: Type 5(is -4), Type 6(is -2), Type 7(is -3) and Type 8(is -1).

The grid shields in both the DFF and DC-SFQ used the standard configuration with a grid bar width of 2.5 μm and spaced at 5 μm . The coil currents depicted in Fig. 4.3 are then loaded into a MATLAB script, shown in Appendix A, to calculate the OFMs for each cell at those coil current conditions. The simulation results for the DFF are summarised in Table 4.4, while those for the DC-SFQ are shown in

Table 4.5. In both the DFF and DC-SFQ, unshielded OFMs have been included as references. The numbers under "Type" correspond to the magnetic field orientations defined in Table 4.3.

4.4.1 Performance of the DFF in a rotated magnetic field

The grid shield's performance, shown under the negative OFMs, is low as expected. Comparatively, the solid shield performs better than the grid shield if the actual OFM values are considered. Both the grid and solid shields showed improvement in OFMs in all the 16 cases as shown in Table 4.4. The rotated fields have a significant perpendicular field contribution, and as presented earlier the grid shield's performance is not good against such fields. This explains the low OFMs for the DFF, especially for negative coil currents for *Types* 1 to 4. Here, magnetic field rotation shows how a specific shield can be effective against one field orientation and become vulnerable to another. The *Types* 5 to 8 are inversions of the *Types* 1 to 4 as indicated in the caption of Fig. 4.10, and the OFMs alternate as the magnetic field orientation is reversed in corresponding cases.

Type	Unshielded		Grid Shielded		Solid Shielded	
	-OFM	+OFM	-OFM	+OFM	-OFM	+OFM
1	38	46	50	98	50	86
2	19	46	37	108	44	74
3	25	60	34	177	37	149
4	54	20	93	29	153	40
5	20	54	29	93	40	153
6	46	19	108	37	74	44
7	60	25	177	34	149	37
8	46	38	98	50	86	50

Table 4.4: DFF OFMs (μT) after the orientation of external magnetic fields was changed. Bold figures show improvement in OFMs compared to the unshielded case.

4.4.2 Performance of the DC-SFQ in a rotated magnetic field

In the DC-SFQ, the grid shield performed better than the solid shield. The grid showed improved OFMs 14 out of 16 cases, shown in Table 4.5, while the solid shield showed improved OFMs only 6 out of the 16 cases. If exposed to an ambient magnetic field, exceeding the Earth's, of $65 \mu\text{T}$, the DC-SFQ could operate properly, unshielded, for most of the stated magnetic field orientations (Table 4.5). However, shielding becomes necessary with increased ambient magnetic fields. On the overall, the OFMs in both the DFF and DC-SFQ show that shielding could improve or in some cases, degrade the magnetic field tolerance of SFQ circuits against selected magnetic field orientations.

Type	Unshielded		Grid Shielded		Solid Shielded	
	-OFM	+OFM	-OFM	+OFM	-OFM	+OFM
1	73	75	95	140	52	109
2	69	71	85	188	49	99
3	54	50	142	64	67	37
4	104	108	69	124	38	71
5	108	104	124	69	71	38
6	71	69	188	85	99	49
7	50	54	64	142	37	67
8	75	73	140	95	109	52

Table 4.5: DC-SFQ OFMs (μT) after the orientation of external magnetic fields was changed. Bold figures show improvement in OFMs compared to the unshielded case.

The performance of the shields in the DFF and DC-SFQ presents another dimension of circuit design for magnetic field immunity. The orientation of circuit elements can be very crucial. In addition, circuits that have storage loops, such as the DFF, are more vulnerable to external magnetic fields. The analysis shown in these results does not necessarily prove which shield is better between the two. However, the OFMs show what shield is suitable for a specific orientation of external magnetic fields.

4.5 Rotated Magnetic fields and Bias Margin Analysis

An alternative analysis and validation of shield implementation can be done by steadily rotating a magnetic field and determining the bias margin at each angular interval for the entire 360° rotation. With this approach, the performance of a shield can be judged by looking at the bias margin at that external magnetic field orientation. In the simulations, a 5-Junction DFF was used and exposed to a constant magnetic field density with a magnitude of 65 μT . In Fig. 4.11, the DFF is shown with the magnetic fields rotated. In experiments, the rotation can be achieved by rotating the DFF attached to a cold head of a cryo-cooler, while keeping the magnetic field's orientation fixed.

In order to effect rotation as shown in Fig. 4.11 using the 3 orthogonal coil approach, the following calculations are done. The three coils have radii $R_{xy} = 125\mu\text{m}$, $R_{xz} = 130\mu\text{m}$ and $R_{yz} = 135\mu\text{m}$ and by using (2.1), the required coil currents are 12.931 mA, 13.449 mA and 13.966 mA for the xy , xz and yz coils, respectively. However, for a rotation depicted in Fig. 4.11, only the xy and xz coils are required, and the current in the yz coil can be tied down to zero for the entire simulation run. To cause the rotation of the magnetic field, the coil currents had to be expressed as follows:

$$I_{xy} = 12.931 \cos \theta \quad (4.1)$$

$$I_{xz} = 13.449 \sin \theta \quad (4.2)$$

where θ is the magnetic field's angle of rotation with respect to the DFF chip as shown in Fig 4.11.

Sixteen (16) equally spaced angles were used for the simulations, resulting in angular increments of 22.5° as indicated in Fig. 4.12. Bias margins for each angle of orientation of the magnetic field were calculated for the three cases of unshielded, grid shielded and solid shielded DFF. The results are presented graphically in Fig. 4.13. The plots were produced manually in AutoCAD™ 2017. The bias spread for each angle is plotted as a line, from the lower to the upper extents as shown in Fig. 4.12. Thereafter, all lower bias margins are then connected together, and so are upper margins for each angle. The effective area under the joined extents are then hatched (shaded) as in Fig. 4.13. Therefore, bias margins for the intermediate angles are approximated by the joining of margins of adjacent angles. This gives an approximate picture of a seamless bias margin distribution for rotated magnetic fields from 0 to 360°.

The results for the unshielded case, depicted in Fig. 4.13(a), show the DFF performs relatively well for angles between 270° and 90°, anticlockwise, but performs poorly on the rest of the angles. The DFF completely fails at angles from 157.5° to 202.5° clockwise, where the magnetic field is almost at 90° with respect to the cell area from the top. At this point, there is substantial coupled current, especially in the storage loop inductance, L_3 , in Fig. 2.4, of the DFF.

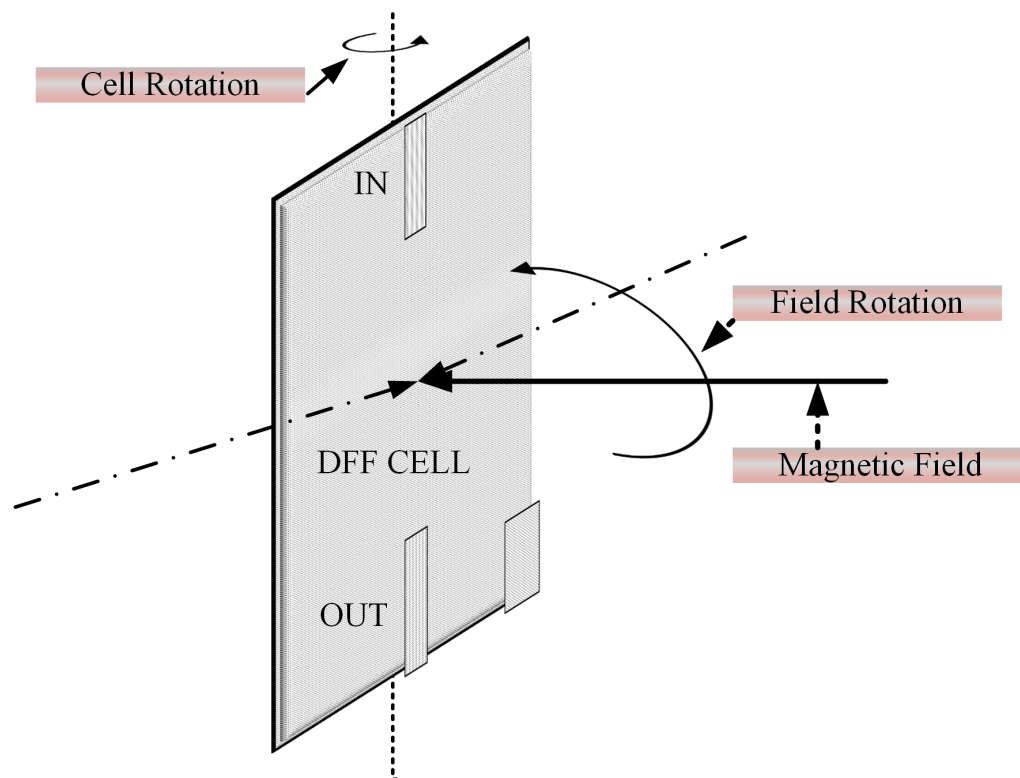


Figure 4.11: Analogy of the effected rotation of an external magnetic field around a fixed DFF cell. Alternatively, in experiments, the DFF can be rotated instead while keeping the field orientation fixed. The 5-Junction DFF was also used in these simulations, where IN and OUT are the DFF's input and output, respectively. The DFF is positioned as shown, i.e. vertically.

On the overall, the bias margins of the DFF for the shielded (Fig. 4.13(b) and Fig. 4.13(c)) cases lean towards the negative bias extents of the bias spread. This can be attributed to uneven shielding current distribution between the ground plane and the shields, because the shields are sporadically grounded by taking advantage of existing gaps in the initial cell layout. As a result, the ground plane carries more current than the shield. The issue of uneven current distribution of such type of grounding has been outlined before in this chapter. The solid shield had an overall wider bias margins for the entire magnetic field orientation spin. Apart from some shrinking in the bias margin in the grid shield (Fig. 4.13(b)), there is an operable bias margin for the entire 360°.

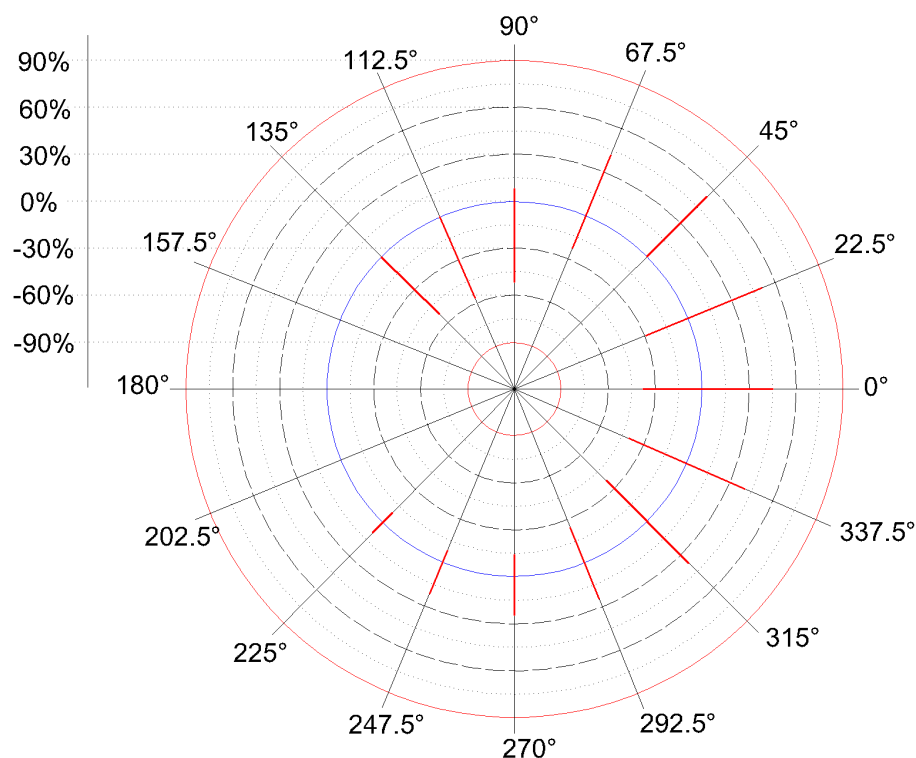


Figure 4.12: A simplified bias margins diagram for the DFF. The length of each line indicates the bias spread for that angle.

For comparison purposes, a DC-SFQ was simulated in the same manner as the DFF. The bias margin results of the DC-SFQ are shown in Fig. 4.14. It can be observed, by comparing the results in Fig. 4.14 to those in Fig. 4.13, that the DC-SFQ is affected more by the rotated 65 μT field than the DFF. In addition, the solid shield performs poorly in the DC-SFQ, while in the DFF, its performance is good. Further, the grid shield in the DC-SFQ performs better than the solid shield. The scenario is reversed in the DFF.

The simulation results in both the DFF and DC-SFQ for a rotated 65 μT field show that the vulnerability of an SFQ circuit to external magnetic fields of any orientation depends on the parameter composition of a cell and the positioning of those parameters on a layout. In addition, the cells have shown to respond differently to external magnetic fields of varying orientation. Hence, it is important to ensure that each shielding mechanism is tested for possible orientation of external magnetic fields. In circumstances where the orientation of the magnetic field cannot be anticipated, the shield that shows a good overall bias margin for the entire 360°, should be used. In this case, these are the solid shield in the DFF and the grid shield in the DC-SFQ. The results shown for both the DFF and DC-SFQ are for the external magnetic field orientation depicted in Fig. 4.11. Thus, it is important to test a SFQ circuit in other directions of rotation for a comprehensive simulation of a cell's performance against external magnetic fields in both unshielded and shielded cases.

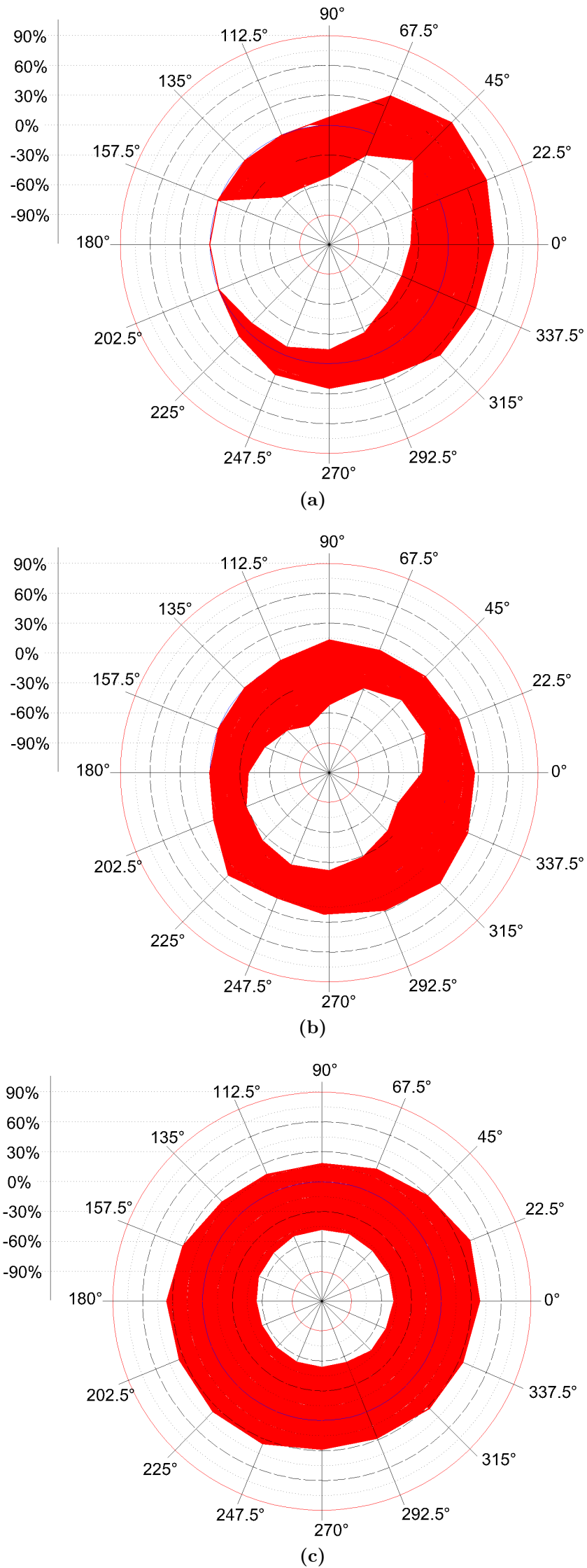


Figure 4.13: Bias margin results for the DFF with a magnetic field rotated around it, (a) unshielded, (b) grid shielded and (c) solid shielded DFFs.

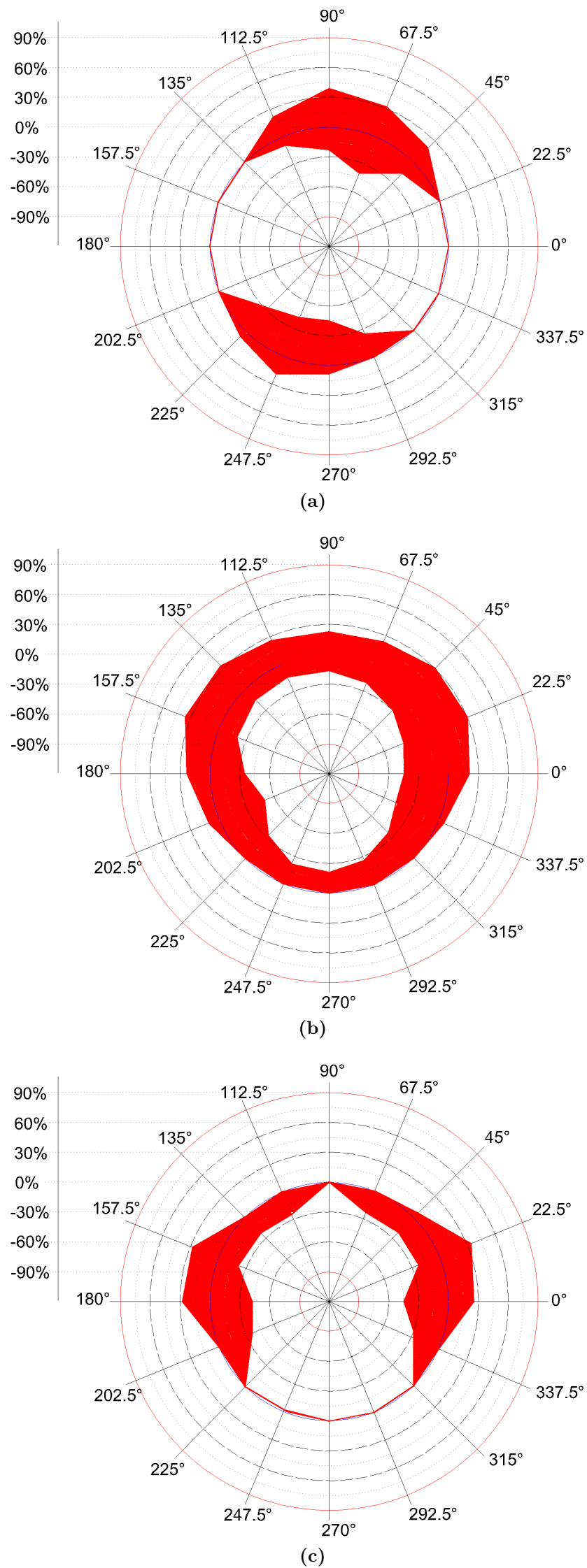


Figure 4.14: Bias margin results for the DC-SFQ with a magnetic field rotated around it, (a) unshielded, (b) grid shielded and (c) solid shielded DC-SFQs.

4.6 Chapter Conclusion

Several factors can affect the performance of on-chip magnetic shield implementations for SFQ. In this chapter, factors, such as ground contact positioning, grid bar spacing in grid shields and magnetic field orientation were investigated and reported. All these factors have to be considered in the design of on-chip shields against specific external magnetic field orientations. It has been established that the ground contact design has to be made specific to a particular cell, as shielding current distributions affect different cells uniquely. For the grid shield implementation, increase in grid bar spacing has a negative impact on shielding effectiveness. It was also confirmed that the orientation of the external magnetic field has a huge impact on the overall design of the shield. Therefore, the immunity of a circuit to an external magnetic field is only valid for a specific orientation of that field or the orientation of the cell.

Chapter 5

Magnetic Field Tolerant Design

Shielding assists circuit designers to come up with SFQ circuits that can withstand magnetic fields up to a known threshold. At a stage SFQ circuit design is, it is infeasible to design without shielding. In the earlier chapters, different solid and grid-shielded SFQ circuits were simulated in various magnetic fields in the excess of $65 \mu T$, from which the variations of the circuits' operating margins were determined to the point of failure. From the failure point, parameters were then redesigned to get practical working margins in the presence of those fields. However, the first step in the design process should be to come up with a cell that has a higher tolerance to magnetic field, even before shielding is implemented. In this chapter, design tenets that can be incorporated into circuit design before any form of either ferromagnetic or on-chip shielding can be incorporated, are discussed. These tenets centre on good layout design of each inductor as well as entire cells against known magnetic field orientations.

5.1 Inductor Design

Inductors are used in SFQ circuits to form and complete superconducting loops, store SFQ pulses and form current distribution lines. In current recycling [7], the inductors are required in the transfer of pulses between coupled sub-circuits. The challenge is that any external magnetic field could couple to these inductors and cause circuit malfunction. Nonetheless, meticulous design of inductors can lower the coupling between the external magnetic field and circuit inductors. Simulations were conducted to show the effect of circuit inductor's physical dimensions on the current that is induced in a particular superconducting loop. Inductors of varying dimensions were used in simulations with uniform static magnetic field, generated by *InductEx* v5.04 Professional. Unlike in the coils, where the the uniformity of the magnetic field on an entire cell depends on the coil radius, this methods produces magnetic fields through a single command line instruction.

The static magnetic field uses a virtual inductor of $1 H$ and the magnetic field that is generated is expressed as $\Phi = LI$ (Wb), where I is the current through the inductor. Therefore, the inductor should produce a magnetic field of $1 Wb$ for a current of $1 A$. Any magnitude of magnetic field is generated by simulating with an equal current. For instance, if the required field is $500 \mu T$, then the required current is $500 \mu A$.

5.1.1 Straight Discrete Inductors

Two sets, with three inductors in each, were used in simulations with a static magnetic field of $1 Wb$ and the induced currents in each inductor were compared. One set is comprised of three inductors of

equal inductance but different dimensions, while the other set is comprised of three inductors of equal length but different widths, hence different inductance. The inductors for Set 1 and their dimensions are shown in Fig. 5.1, while those for Set 2 are shown in Fig. 5.2.

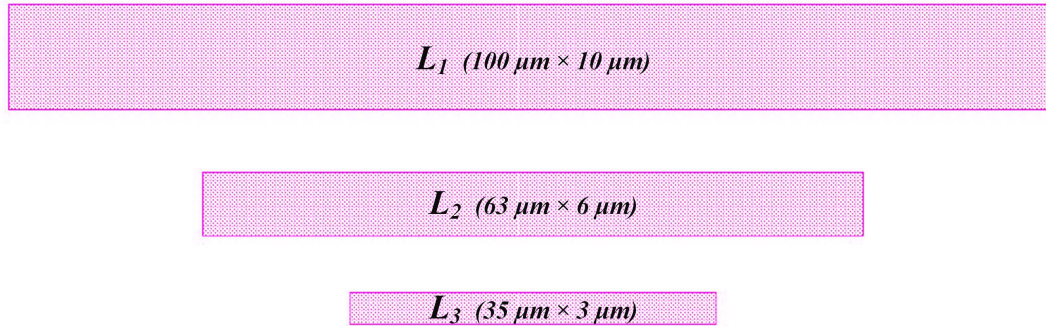


Figure 5.1: Set 1: Three inductors of different dimensions, but equal inductance.

Table 5.1: Induced currents in the Inductors of Set 1 .

Inductor	Inductance (pH)	Absolute Induced Current (A)	
		y -directed field	z -directed field
L_1	6.558	8.389	3.431×10^{-2}
L_2	6.573	5.271	2.537×10^{-2}
L_3	6.576	2.928	2.571×10^{-3}

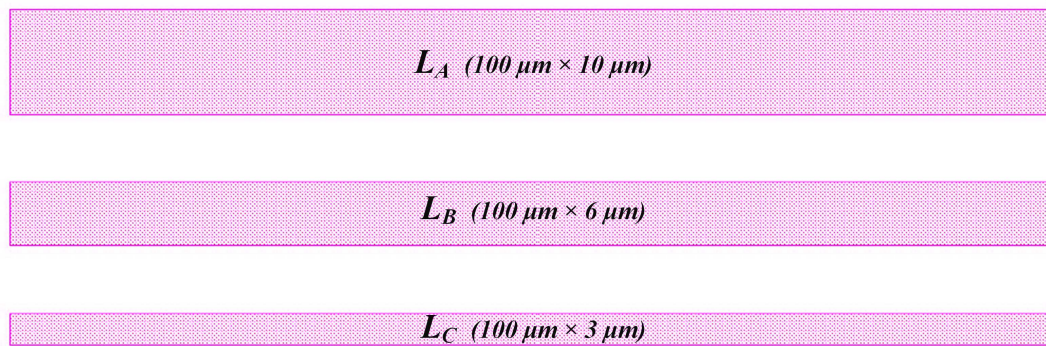


Figure 5.2: Set 2: Inductors of equal length, but different widths

Table 5.2: Induced currents in the inductors of Set 2

Inductor	Inductance (pH)	Absolute Induced Current (A)	
		y -directed field	z -directed field
L_A	6.558	8.388	3.432×10^{-2}
L_B	10.448	5.264	1.834×10^{-2}
L_C	18.815	2.923	3.120×10^{-3}

In both Set 1 and Set 2, the inductors were simulated, one inductor at a time, on a ground plane that was extended $150 \mu m$ in the x -direction and $60 \mu m$ in the y -direction. A wider ground plane has less effect on calculated inductance [79]. The simulations used static magnetic fields projected from the x , y and z directions for each inductor, one field direction at a time. The coupling due to x -directed magnetic fields was zero because the produced fields are in-plane, whereby the fields do not cut the inductors. Hence, only the results for y and z -directed fields are shown in Table 5.1 and Table 5.2.

In Set 1, with equal inductance in all three inductors, it shows that coupling, hence induced current decreased as the area of the inductor reduced, as depicted in Table 5.1. This behaviour is also replicated

in the uniform length inductors, depicted in Table 5.2. The results show that narrow and short inductors have less induced current from the external magnetic fields. In both sets, induced currents from the y -directed field case are higher than in the z -directed magnetic field case. This is attributed to the y -directed fields being able to cut the inductors at right angles, hence high coupling.

Therefore, a circuit's magnetic field tolerance can be improved by carefully laying out components, such as inductors. Inductors must be made as short as possible and as narrow as the fabrication process permits. For, instance the *Hypres'* 4.5 kA/cm^2 permits a minimum width of $2.5 \text{ }\mu\text{m}$ for a structure made in the layer $M2$. However, good design practice stipulates that the real width must be higher than the bare minimum to improve circuit yield and manufacturability. Against a known magnetic field orientation, inductors must be laid out along the magnetic field's direction, like in x -directed case, and not perpendicular, as the results show in Table 5.1 and Table 5.2.

5.1.2 Meandered Discrete Inductors

Inductors can be laid out to decrease coupling to specific magnetic field orientations. However, in most instances, the magnetic field orientation is unknown and layout designs that protect the circuit from more than one orientation are preferred. It is possible to improve circuit operation against one magnetic field direction, after layout and parameter changes. Nonetheless, this could also result in performance degradation against a different magnetic field orientation. This challenge is outlined in the simulations reported here. Three inductors, one straight (L_S) and the other two meandered (L_{ME1} and L_{ME2}), as shown in Fig. 5.3, were considered in this simulation. Their inductance was kept approximately equal in all inductors as shown in Table 5.3. In the simulations, the ground plane was kept wide by extending it to $150 \text{ }\mu\text{m}$ in the x direction and $60 \text{ }\mu\text{m}$ in the y direction, same as the one used in Section 5.1.1.

The results in Table 5.3 show a possible layout designer's predicament. The induced currents, by the y -directed fields, in the meandered inductors, L_{ME1} and L_{ME2} , are less than in the straight inductor L_S . This is a real improvement, however, it is also shown that the currents induced by z -directed fields are much higher in L_{ME1} and L_{ME2} than in L_S . The attempt to lower coupling in one magnetic orientation might result in increased coupling in the other. The design change could be important if the magnetic fields in the z -direction are in very small quantities. Comparatively, between the two meandered inductors, L_{ME1} and L_{ME2} , there is less coupled currents in L_{ME1} than in L_{ME2} . This is attributed to the physical layouts of the two, L_{ME2} meanders are small and looks almost straight, especially against y -directed magnetic fields. For the x -directed fields, the coupling is zero, hence no current is induced, because the two meandered inductors are laid out symmetrically on the x axis and hence any coupled magnetic fields will effectively cancel out.

Overall, L_{ME1} offers a good compromise, especially if the fields in the y -direction are the target. The concept in L_{ME1} inductor can be made to counter the effect of magnetic fields in any orientation by rotating the inductor layout accordingly. The results for L_{ME1} and L_{ME2} also show the importance of meander symmetry because the induced currents cancel out, as it has been shown in the x -directed magnetic fields.

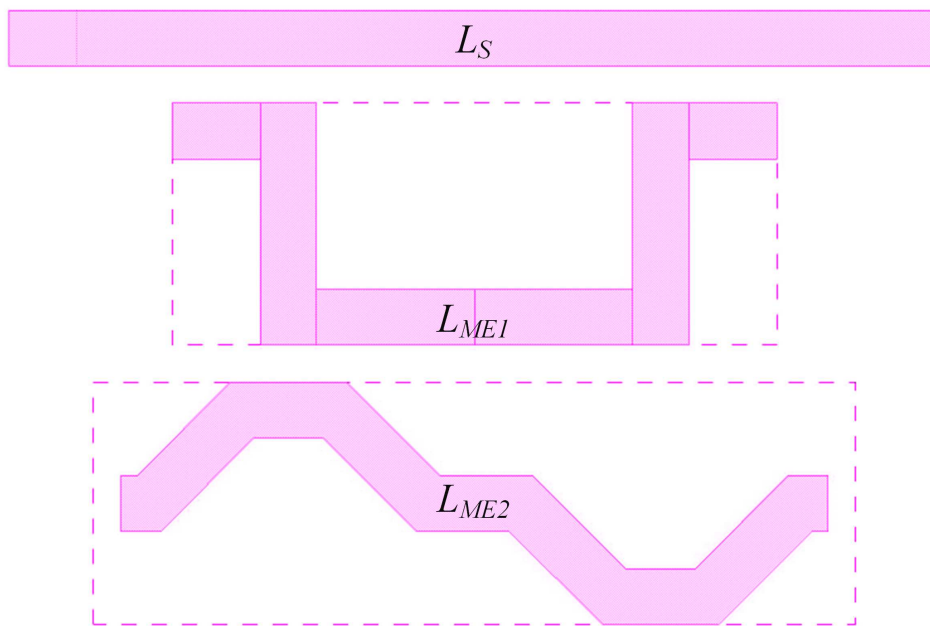


Figure 5.3: Inductors of equal inductance but different shapes. Inductor L_S has the same dimensions as L_B of Fig. 5.2.

Table 5.3: Induced currents in inductors with equal length but different widths as shown in Fig. 5.3.

Inductor	Inductance (pH)	Absolute Induced Current (A)	
		y -directed field	z -directed field
L_S	10.448	5.264	1.834×10^{-2}
L_{ME1}	10.498	3.405	$2.032 \times 10^{+0}$
L_{ME2}	10.437	4.005	$2.964 \times 10^{+0}$

5.1.3 Ring Shielded Inductors

SFQ circuit inductors can be shielded, separately, to lower coupling to magnetic fields of specific orientations. One technique is to use superconducting rings (or loops), without Josephson junctions, around an inductor. This method was investigated and tested before with a ring shielded SQUID [34]. However, this approach seeks to offer design changes to a specific inductor, so that coupling to that inductor is significantly reduced or prevented. Hence, ring shielded inductors were simulated in external magnetic fields. Three ring configurations were examined, A, B and C, as illustrated in Fig. 5.4. The inductor L_D has the same dimensions as L_1 shown in Fig. 5.1, with $100 \times 10 \mu m$ dimensions. All three configurations were grounded as shown, with ground contact pads marked GND. An ungrounded ring is not shown because the results obtained were the same as in the unshielded (no ring) case (results for L_1 in Table. 5.1).

Unlike in the earlier cases, where there was no coupling with x -directed fields, the ring introduces coupling to those fields. The grounded ring conducts coupled currents, afterwards it produces secondary fields that cut the inductor in the z orientation. Thus, enabling the coupling between the x -directed fields and the inductor L_D . The results in Table 5.4 show that coupling is least in case B for the x -directed fields. This is the case because the ground contacts divide the ring into two, and because the induced current flows in the same direction, the effect is almost half of the current introduced in case A.

The reduction in induced currents from the y -directed fields is comparable to that in the x -directed magnetic field case, only that the B and C cases interchange. However the small changes, in ring C, are unnoticeable due to the already large coupling to y -directed fields. The explanation is the same as in the x -directed case. In the z -directed case, configurations B and C show improvement over the unshielded

case. The grounded ring absorbs most of the magnetic energy from z -directed field, with configuration C the most efficient, with the least coupling. The results in Table 5.4 show that configuration C is the best compromise for an inductor to be shielded by a grounded ring.

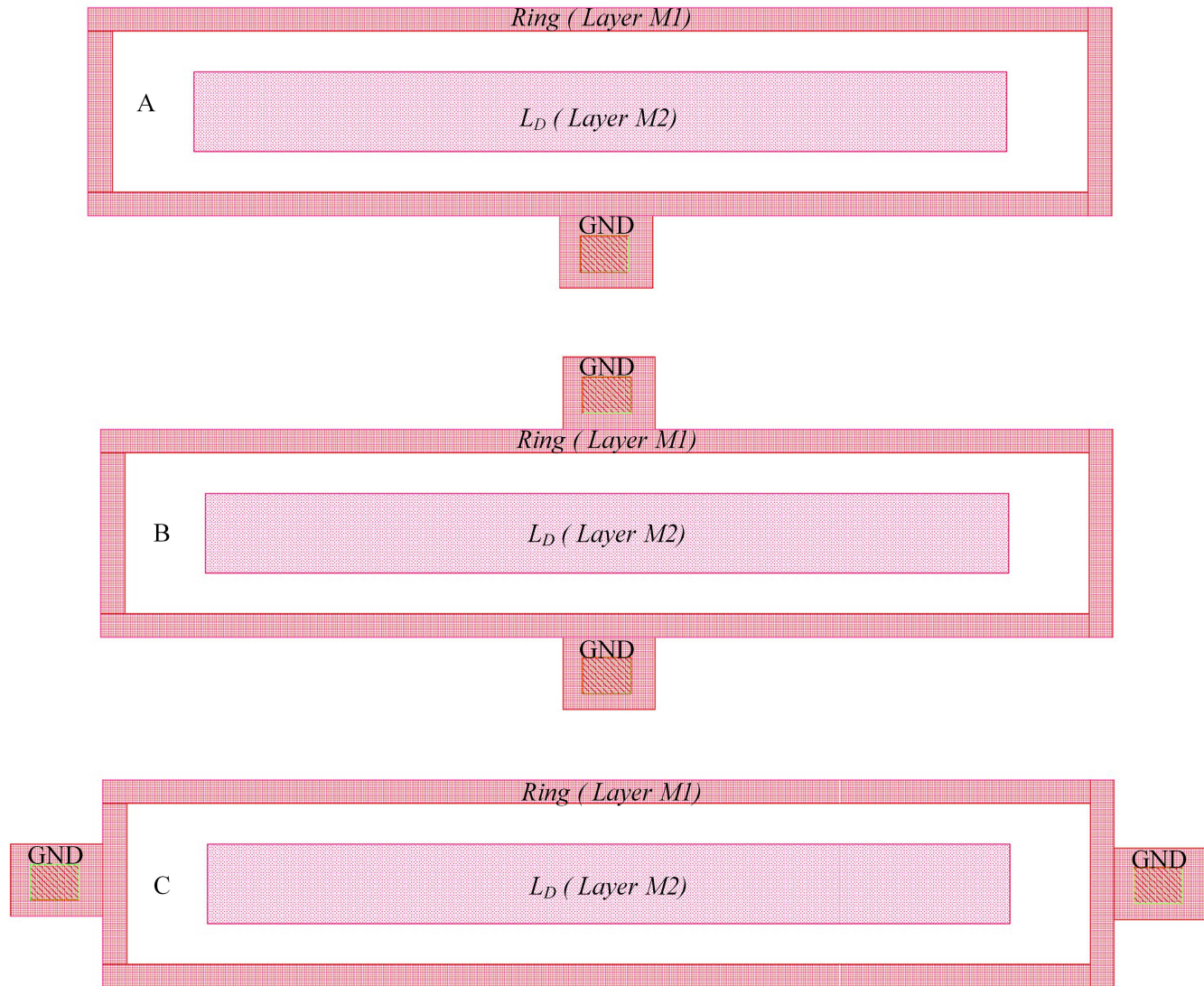


Figure 5.4: Three grounded (GND) ring configurations around the inductor L_D laid out in layer M2. A: Inductor with a ring in M1 and one ground contact, B: Inductor with a ring grounded at two locations across the Inductor and C: Inductor with a ring grounded at two locations at both ends of the inductor.

Table 5.4: Induced currents from different magnetic fields in the ring configurations shown in Fig. 5.4.

Setup	Absolute Induced Current in L_1 (A)		
	x -directed field	y -directed field	z -directed field
L_D	0	8.388	3.431×10^{-2}
A	2.724×10^{-5}	8.393	2.072×10^{-1}
B	1.506×10^{-5}	8.396	1.401×10^{-2}
C	1.616×10^{-4}	8.346	4.002×10^{-4}

Results for inductor L_D are the same as those for inductor L_1 reported in Table 5.1, included here for comparison with the ringed versions of the same inductor. All the inductors have the same dimension, hence inductance of 6.558 pH.

The results in Table 5.4 and the accompanying explanations are supported by the magnetic field plots shown in Fig. 5.5, which shows three plots for each configuration in Fig. 5.4, for all three magnetic field orientations: x , y and z . Further explanation is offered in the caption of Fig. 5.5.

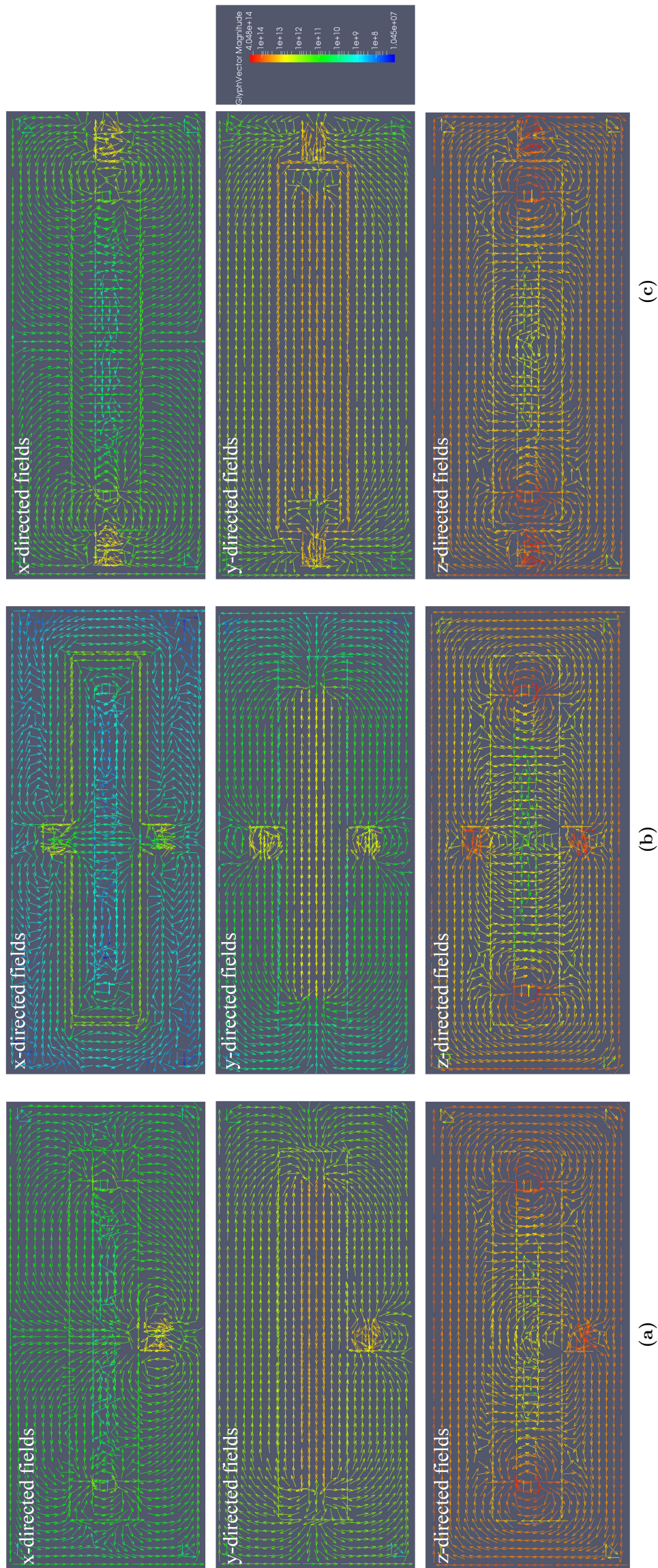


Figure 5.5: Magnetic field plots for the three configurations (a), (b) and (c), corresponding to A, B and C, respectively, shown in Fig 5.4, for x , y and z -directed magnetic field density

The magnetic field plots show the extent of coupling in each case, in reference to the scale, on the right. Red is the highest, while blue is the lowest. The arrows in the plots point to the direction of coupled magnetic fields on the inductors and their rings. In the x -directed cases, the coupling is least in (b), represented by the blue arrows on the inductor, while the ground contacts for the x -directed case. The magnetic field in the y -directed cases are high because the coupled magnetic flux flows along the inductor and that the ground contacts have little effect on this flow. Lastly, in the z -directed field case, the coupling is very high to the ground contacts and the inductor ends, however, the fields point in opposite directions and cancel out on most areas in the layout. Most of the inductor length is exposed to reduced fields (green colour), signifying less coupling. The results depicted in these plots are consistent with those shown in Table 5.4.

5.2 Cell Layout for Improved Magnetic Field Tolerance

Operating field margins (OFMs) of SFQ cells could be improved by implementing some of the inductor design changes outlined in Section 5.1. In order to show this on real SFQ cells, the 5-Junction DFF and DC-SFQ were modified to improve unshielded OFMs. The original layouts, with bias resistors, are shown in Fig. 5.6 and have been used in this discussion.



Figure 5.6: Two SFQ cell layouts in their formally optimised form: (a) DFF and (b) DC-SFQ

5.2.1 The DFF Cell

Tolerance and hence immunity of a SFQ circuit to external magnetic field is dependent on the orientation of the said magnetic field. The most effective shield for all orientations is a thick sealed cylindrical superconducting shield that covers the entire SFQ circuit, which is impractical and difficult to implement on-chip, with the current fabrication technologies. However, the proper interpretation of calculated coupling coefficients could aid in designing circuit layouts that have improved tolerance to external magnetic fields of specific orientations. An unshielded DFF was established to have the OFMs depicted in Table 5.5. Coils of $125 \mu\text{m}$ radius were used in the calculation of the OFMs using *Biot – Savart* Law.

Table 5.5: Operating field margins for the unshielded DFF

xy -coil (z -directed fields)		xz -coil (y -directed fields)		yz -coil (x -directed fields)	
-OFM	+OFM	-OFM	+OFM	-OFM	+OFM
$28 \mu\text{T}$	$30 \mu\text{T}$	$87 \mu\text{T}$	$80 \mu\text{T}$	$90 \mu\text{T}$	$68 \mu\text{T}$

Simulations for calculating the OFMs were carried out using the orthogonal coils already discussed in Section 2.3.3. The coil method was chosen for these simulations to compare the results to those obtained in the shield analyses already made and presented in the preceding chapters. Each cell was simulated with one coil, xy , xz and yz , at a time. The coupling of the x -directed fields (from the yz -coil in this case) to the circuit inductance are shown in Table 5.6. The coupling coefficients are higher for inductors L2, L4 and L6. Two things are common to all three inductors; they are all comparatively wider and

perpendicular with respect to the x -directed magnetic fields, hence the high coupling, as established in Section 5.1.

Table 5.6: Coupling coefficients between the yz -coil and respective inductors L1 to L7. K2, K4 and K6 (all in bold), are, on average, higher than the rest by over 10 times.

Inductor	Coupling to the yz -coil
K1	+1.05E-4
K2	+1.29E-3
K3	-6.35E-4
K4	-1.07E-3
K5	-8.14E-4
K6	+1.45E-3
K7	+3.64E-4

In normal operating margin calculation, the coupling coefficients are fixed, while the external magnetic field is varied. However, if the coupling coefficients were made variable, the circuit designer should be able to decide what coupling coefficients need to be altered to improve tolerance to magnetic fields. It is usually tempting to simply reduce the width of the inductors, in this case, L2, L4 and L6, but the circuit dynamics might not let such crude changes. The external magnetic field contributes coupled currents to the circuit loops, and the directions of the coupled currents are determined by the coupling coefficients. An increase or reduction of these coupled currents introduces different switching thresholds for Josephson junctions in each loop. The distribution of such currents is illustrated in Fig. 5.7. The current distribution in Fig. 5.7 shows that I_{k_2} and I_{k_3} subtract from the bias currents for J_2 and J_4 , respectively. Josephson junctions whose designed switching pattern could be affected are J_2 and J_4 . A circuit optimizer could be used to find the best possible coupling coefficient changes to ensure better operating margins and immunity to magnetic fields. One coupling coefficient, K2, was chosen to determine how the circuit could be affected, if varied. By using margin analysis results, that include all coupling coefficients, a designer can determine how the coupling can be changed to realize any improvement.

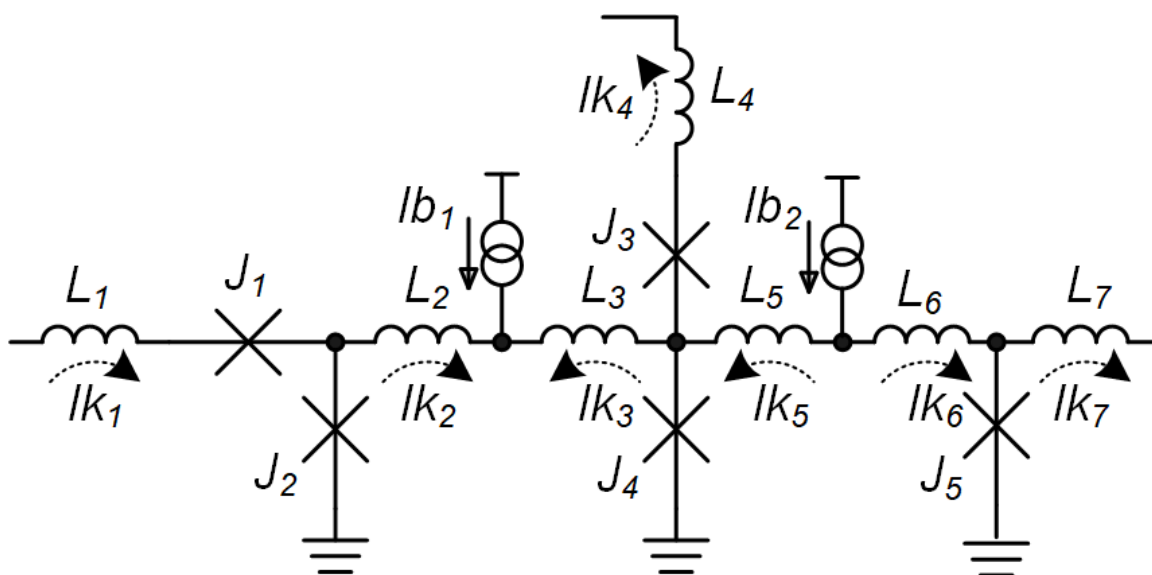


Figure 5.7: Directions of flow for the coupled currents in each loop according to the coupling coefficients depicted in Table 5.6. The assumed positive direction of flow is left to right.

The coupling coefficients were included in the simulation model and the x -directed (yz -coil) field margin analysis results of the DFF, just before failure are shown in Fig. 5.8. The failure point is the +OFM for the x -directed (yz -Coil) shown in Fig. 5.5, that is $68 \mu\text{T}$ (or $13.5 \mu\text{A}$). The results in Fig. 5.8 show that the coupling coefficients K1 and K7 have little effect on the operation of the DFF up to the simulated

magnetic field density, with a spread of -90% to 90% . However, K2 and K5 need to be increased, while K3, K4 and K5 could improve the circuit operation if they were reduced. The circuit operates in an equilibrium and any changes to these parameters shifts this balance.

If K2 alone was increased by 50%, from 1.29e-03 to 1.94e-03, the +OFM of the DFF against yz -coil's x -directed field changes from 68 μT to 76 μT , while the -OFM shifts from 90 μT to 123 μT . This is a big improvement achieved by changing one coupling coefficient. The process could be repeated by calculating margins soon before failure, to find how the rest of the coupling coefficients could be altered to realize the best equilibrium that makes the circuit more immune to magnetic fields. The increase in K2 from 1.29e-03 to 1.94e-03 changes the circuit dynamics such that K6 needs to be increased to improve either -OFM or +OFM. An increase in K6 by 10% from 1.45e-3 to 1.60e-3, while keeping K2 = 1.94e-03, increases the +OFM to 76 μT from 72 μT , while the -OFM increases to 157 μT from 123 μT . This means a 10% increase in K6 improved the -OFM, but had a minimal effect on the +OFM. The layout designer should always strive to strike a balance, when making cell layouts, with the aim of altering coupling coefficients.

Name	Margins		
B1	[.....===== =====]	-40.1,	90.0
B2	[.....===== =====]	-12.0,	35.9
B3	[.....===== =====]	-75.9,	0.7
B4	[.....===== =====]	-1.4,	85.8
B5	[.....===== =====]	-8.4,	42.9
IB1	[.....===== =====]	-47.8,	5.6
IB2	[.....===== =====]	-90.0,	4.9
K1	[.....===== =====]	-90.0,	90.0
K2	[.....===== =====]	-6.3,	90.0
K3	[.....===== =====]	-90.0,	5.6
K4	[.....===== =====]	-90.0,	2.1
K5	[.....===== =====]	-3.5,	90.0
K6	[.....===== =====]	-90.0,	2.8
K7	[.....===== =====]	-90.0,	90.0
L1	[.....===== =====]	-90.0,	90.0
L2	[.....===== =====]	-56.2,	90.0
L3	[.....===== =====]	-54.8,	35.9
L4	[.....===== =====]	-90.0,	2.1
L5	[.....===== =====]	-5.6,	90.0
L6	[.....===== =====]	-90.0,	3.5
L7	[.....===== =====]	-90.0,	90.0

Figure 5.8: Margins of the DFF, before failure that is 67 μT (or 13.4 μA through the yz -coil) for only one direction of coil current. K2, K4 and K6 are in blocks.

5.2.2 Layout Changes to the DFF Cell

Layout changes were made to the DFF as shown in Fig. 5.9. However, it was noted that the changes suggested in Fig. 5.8 could not be realised because, as explained before, for coupling to reduce, the width of an inductor has to be reduced as well. However, a reduction in width increases inductance. For instance, in the case of K6 - L6, it is required that the coupling K6 be reduced, while at the same time the inductance of L6 needs to be reduced. The inductance of L6 can be reduced by increasing the inductor's width, however, that could increase the coupling, K6. The case is similar to K2 - L2 and K4 - L4. Positive results were realised by considering other combinations, such as K3 - L3 and K5 - L5, which are shown in Fig. 5.9 marked A and B, respectively.

The changes depicted in Fig. 5.9 had diverse implications. The change marked by arrow A, was for inductor L3. The inductance of L3 was maintained, however, coupling (K3), to the x -directed magnetic field (from the yz -coil) dropped in magnitude, from -6.35E-4 to -5.24E-4 (Table 5.7), in line with the recommendations in Fig. 5.8. In order to realize the change in K3, the inductor L3 had a meandered

section in layer M1 added, as shown in Fig. 5.9. Dropping part of the inductor into layer M1 from M2 proved beneficial, because of the normal separation that exists between layers that has shown to reduce coupling to the x -directed magnetic field. As for the change marked B, for inductor L5, coupling and inductance of L5 could not be realised without compromising the coupling to other inductors. Hence, L5 was increased from 2.12 pH to 2.65 pH and K5 reduced, in magnitude, from $-8.14\text{E-}4$ to $-6.95\text{E-}4$.

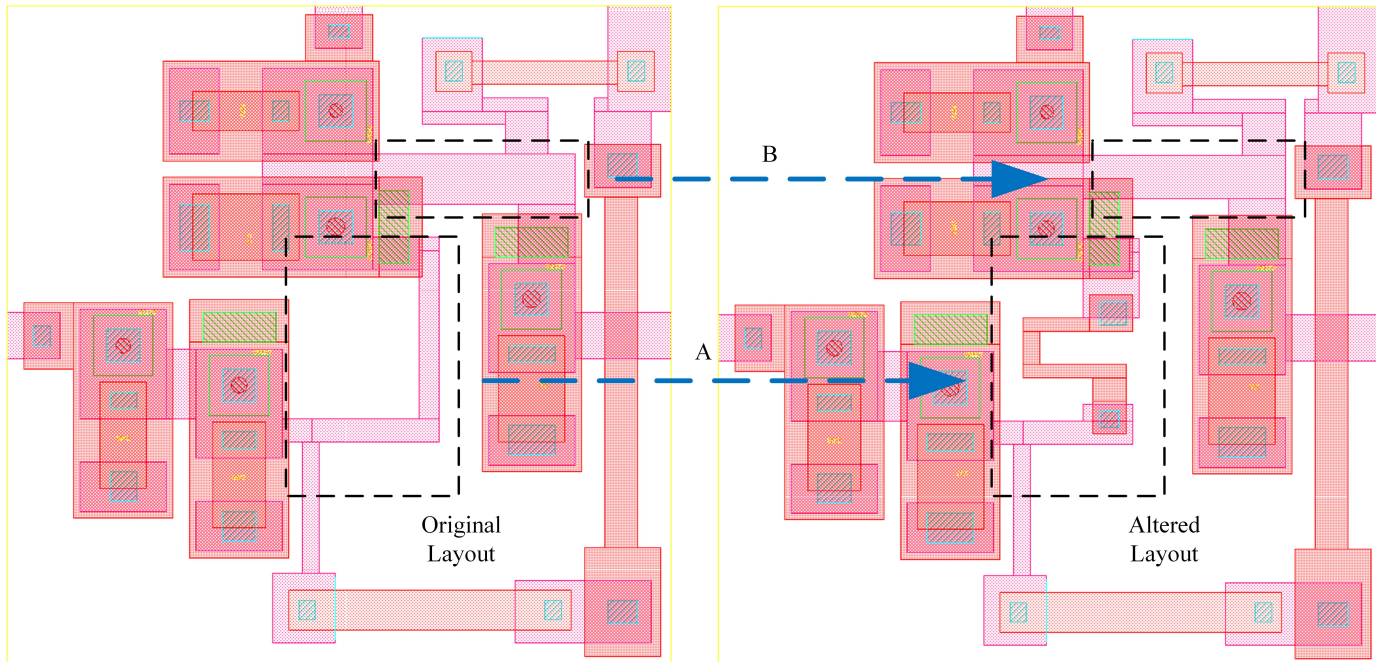


Figure 5.9: Two DFF cells, lined-up side by side. The dashed boxes show the effected changes

Table 5.7: New coupling coefficients between DFF circuit inductance and x -directed fields from the yz -coil

Inductor	Old Coupling to the yz -coil	New Coupling to the yz -coil
K1	+1.05E-4	+1.16E-4
K2	+1.29E-3	+1.29E-3
K3	-6.35E-4	-5.24E-4
K4	-1.07E-3	-1.05E-3
K5	-8.14E-4	-6.95E-4
K6	+1.45E-3	+1.52E-3
K7	+3.64E-4	+3.77E-4

The combined changes marked A and B produced a shift in OFM in a such a way that -OFM improved from $90 \mu\text{T}$ to $147 \mu\text{T}$, while the +OFM only improved from $68 \mu\text{T}$ to $76 \mu\text{T}$. The effect on OFMs is substantial only in the -OFM, hence, the DFF has to be aligned properly to take advantage of the increased OFM in that direction for x -directed magnetic fields.

5.2.3 The DC-SFQ Cell

Similar to what was done in the DFF, the DC-SFQ's coupling coefficients were examined to design a cell that had increased immunity against a specific magnetic field orientation. The DC-SFQ is a relatively strong cell against external magnetic fields, compared to the DFF. The OFMs for the unshielded DC-SFQ are shown in Fig. 5.8 and the superiority against the DFF is clear, especially against x -directed fields. In some cases, y and x -directed fields, both the DFF and DC-SFQ can operate unshielded in an environment with an ambient magnetic field density not exceeding $65 \mu\text{T}$.

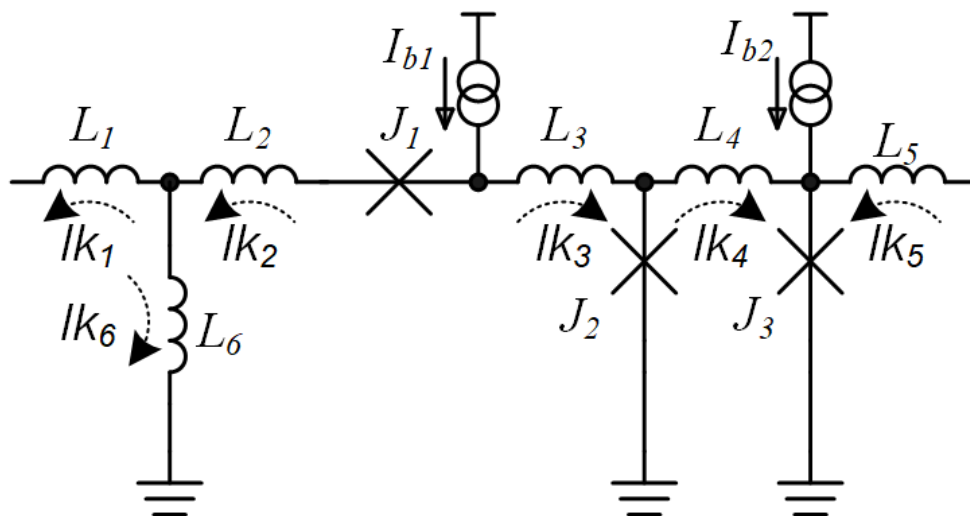
Table 5.8: Operating field margins for the unshielded DC-SFQ

xy -coil (z -directed fields)		xz -coil (y -directed fields)		yz -coil (x -directed fields)	
-OFM	+OFM	-OFM	+OFM	-OFM	+OFM
$47 \mu\text{T}$	$39 \mu\text{T}$	$108 \mu\text{T}$	$74 \mu\text{T}$	$211 \mu\text{T}$	$200 \mu\text{T}$

The coupling coefficients against the x -directed magnetic fields from the yz -coil are shown in Table 5.9. Coupling is much higher to L2 (K2) and L3 (K3), quoted in bold. The two coupling coefficients give the first step to take to make improvements to the layout. However, caution has to be exercised as the current distribution shown in Fig. 5.10 is difficult to handle. The challenge is that an increase or decrease in coupled currents can shift the loop currents in another loop to the point of circuit failure, as described in Section 5.2.1. The loop currents are shown in Fig. 5.10. In the loop comprising L_6 , L_2 , J_1 , L_3 and J_2 , a reduction in I_{k_2} means an increase in the total loop current, which increases the effect I_{k_3} brings into the loop. This loop is the most critical in the operation of the DC-SFQ. The layout of inductor L_6 in layer M1, shown in Fig. 5.6(b), causes less coupling to the yz -coil fields, because M1 layer lies on a lower level and magnetic fields at the top could be blocked by other cell structures. The current subtracted from the loop by I_{k_4} is relatively smaller, unlikely to have much affect on the loop's operation. The aim is to make sure that the operation of the loop is dependent on the input DC and bias currents conditions, as close as possible.

Table 5.9: Coupling coefficients between yz -coil and respective inductors L1 to L6. K2, K3 (all in bold), are much higher than the rest, by over 10 times, on average.

Inductor	Coupling to the yz -coil
K1	-3.25E-4
K2	-1.47E-3
K3	+1.34E-3
K4	+5.90E-5
K5	-3.51E-5
K6	+3.83E-4

**Figure 5.10:** Directions of flow for the coupled currents in each loop according to the coupling coefficients depicted in Table 5.9. The assumed positive direction of flow is left to right.

The OFMs for the unshielded DC-SFQ are shown in Table 5.8. However, by examining the margins before circuit failure, shown in Fig. 5.11, it can be decided what components could be adjusted to improve the OFMs in the DC-SFQ. The coupling coefficients K2 and K3, highlighted in Fig. 5.11, can be altered to improve the OFMs. The results show that K2 needs to be reduced while K3 needs to be

increased. These changes cannot be done at the same time manually, as a change in one parameter, K2, shifts the balance point and K3 might need to be reduced, instead. A change of 20% in K2, from $-1.47\text{e-}3$ to $-1.18\text{e-}3$ causes a significant change in both the -OFM and +OFM. The new value of K2 is fed back into the simulation model to calculate the new OFMs. The OFM calculations are done with a MATLAB script that calculates the margins at every increment of coil currents. In this case, the proposed increase in K2 yields changes, in that the -OFM is improved from $211\ \mu\text{T}$ to $373\ \mu\text{T}$, while the +OFMs shifts from $200\ \mu\text{T}$ to $298\ \mu\text{T}$, against the x -directed magnetic fields.

Name	Margins		
B1	[..... =====]	-12.0,	4.2
B2	[..... =====]	-0.7,	90.0
B3	[..... =====]	-2.8,	63.3
IB1	[..... =====]	-10.5,	0.0
IB2	[..... =====]	-87.9,	2.8
K1	[..... =====]	-90.0,	90.0
K2	[..... =====]	-90.0,	1.4
K3	[..... =====]	-0.7,	72.4
K4	[..... =====]	-90.0,	5.6
K5	[..... =====]	-51.3,	90.0
K6	[..... =====]	-90.0,	1.4
L1	[..... =====]	-90.0,	90.0
L2	[..... =====]	-90.0,	2.8
L3	[..... =====]	-1.4,	90.0
L4	[..... =====]	-90.0,	2.8
L5	[..... =====]	-90.0,	90.0
L6	[..... =====]	-64.7,	2.1

Figure 5.11: Margins of the DFF, soon before failure that is $199\ \mu\text{T}$ (or $39.6\ \mu\text{A}$ through the yz -coil) for only one direction of coil current). K2 and K3 are the block.

The changes in coupling coefficients in both the DFF and DC-SFQ are only good for the said magnetic field orientation. Other orientations could require different changes in the coupling coefficients. Therefore, it is imperative to consider making changes that fit the magnetic field orientation in which the circuit is designed to operate.

The quest for laying out narrow inductors is impeded by wide Josephson junctions. The top and bottom superconducting layers used to make junctions are also used to connect and hence become part of inductors. This makes some parts, if not the whole inductor unnecessarily wider. As it has been shown in Section 5.1, wider a structure provides stronger coupling to external magnetic fields.

5.2.4 Layout Changes to the DC-SFQ Cell

Following the estimates made in Section 5.2.3, changes can be made to the DC-SFQ to realize the new value for coupling coefficient K2. When the coefficient K2 was reduced from $-1.47\text{e-}3$ to $-1.18\text{e-}3$ in Section 5.2.3, the assumption was that the rest of the coupling factors and inductances remained unchanged. This does not happen in practice. Small changes to one parameter are bound to affect several others, positively or negatively. The original layout for the DC-SFQ is shown in Fig. 5.6(b). The layout of the DC-SFQ cell was altered as shown in Fig. 5.12(b), shown alongside Fig. 5.12(a), which is the original cell, also depicted in Fig. 5.6(b). The change in K2 was achieved by reducing the width of L2, however, that increased its inductance. In addition, inductor L6 had to be reduced in value and its width reduced to lower coupling to x -directed magnetic fields. The new coupling coefficients are shown in Fig. 5.10, with notable changes to K2, K3 and K4. In order to increase the coupling coefficient K3, as indicated by the results in Fig. 5.11, its width had to be increased, causing its inductance to drop, whereas the parameter margin for L3 suggests otherwise. Alternatively, the orientation of the inductor, in the layout, had to be changed to alter the coupling coefficient. However, it was easier to reduce the

inductance of L6, by making it shorter, and thinner to reduce coupling also as recommended in Fig. 5.11. These changes are shown in Fig. 5.12.

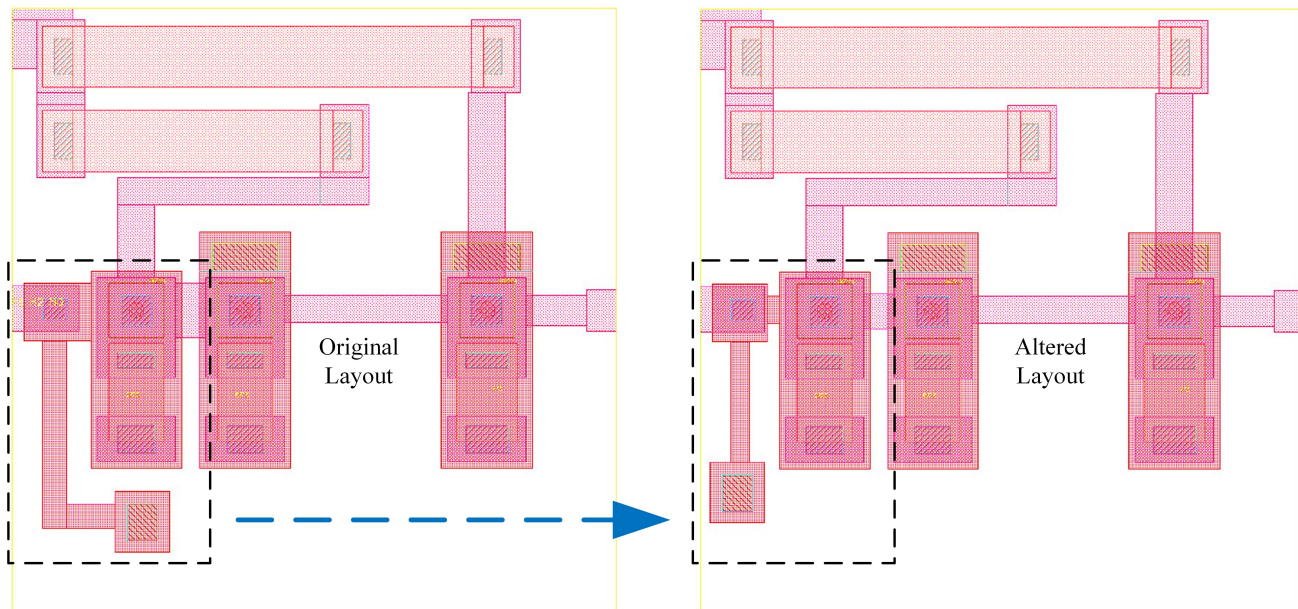


Figure 5.12: Two DC-SFQ cells, lined-up side by side. The dashed boxes show the changes made.

Table 5.10: New coupling coefficients between DC-SFQ circuit inductance and x -directed fields from the yz -coil.

Inductor	Old Coupling to the yz -coil	New Coupling to the yz -coil
K1	-3.25E-4	-3.60E-4
K2	-1.47E-3	-1.05E-3
K3	+1.34E-3	+1.13E-3
K4	+5.90E-5	+2.96E-5
K5	-3.51E-5	-4.81E-5
K6	+3.83E-4	+3.63E-4

The changes made to the DC-SFQ layout, hence the coupling coefficients resulted in a shift in OFMs. The DC-SFQ had -OFM increased from, 211 μT to 254 μT while the +OFM increased from 200 μT to 365 μT . The -OFM, while superior before the changes were made, fell below the +OFM by over 100 μT . This is the case because the coupling coefficients contribute to loop currents differently as shown in Fig. 5.10. Therefore, a change in direction of the x -directed magnetic fields has an opposing effect on the loop currents.

5.3 Design for Known Magnetic Fields

This is an extension of what has been presented in Section 5.2, the only difference is that at this point the design of SFQ circuits is done against a known external magnetic field. The aim is to ensure that an SFQ circuit operates beyond that magnetic field. In the analysis here, grid and solid shielded DFF and DC-SFQ circuits have been used, however, the same principle can be applied to unshielded cells to improve the OFMs.

The effect of altering selected circuit parameters, such as Josephson junctions critical currents and inductance values, was investigated. By using already optimised circuits as a starting point, the circuit can be modified. For the DFF and DC-SFQ, schematics, optimised parameter values and bias margins are shown in Fig. 5.13 and Fig. 5.14, respectively.

Most SFQ cells have shown to recover operation, with broader OFMs, by adjusting bias currents to compensate for the induced currents from external magnetic fields. This approach is mostly not practical due to the nature of biasing systems for SFQ circuits. It is not easy to adjust the bias current for a single cell in a large circuit, without affecting the rest. A better approach is to alter selected circuit parameters. Margin analysis results of a circuit close to failure show what parameters can be altered to recover functionality. The cells in Fig. 5.13 and Fig. 5.14 were grid and solid shielded and their operating field margins calculated. The margin spread for the cells close to their failure limits are shown in Fig. 5.15 where the parameters that can be altered are marked in boxes. The main focus is to make the cells more tolerant to external magnetic field by establishing counter measures against the extra loop currents from the external fields. In the DFF, the parameter L_5 , in Fig. 5.15 was chosen for alteration, while for B1 (J_1), B3 (J_3) and L6 were marked for the DC-SFQ. Other combinations can be made as long as a noticeable change is attainable and that initial margins, those without external fields, are within acceptable limits. In the simulation, the 3-D coil system was used, hence the calculated OFMs are the vector sums of the three orthogonal fields from the xy , xz and yz -coils [76]¹.

In Table 5.11, the *Initial OFMs* are the ones shown in Fig. 3.12 for both the grid (at $5 \mu\text{m}$ spacing) and the solid (at $0 \mu\text{m}$ spacing) shields. The *Initial OFMs* were calculated for the shielded cells, before the alterations were made. The *New OFMs* were calculated after selected parameters were altered in both cells. In the DFF, only the value of L_5 was changed, while in DC-SFQ, the values of L_6 , J_1 and J_3 were changed (refer to Fig. 5.13, Fig. 5.14 and Table 5.11). Simulations for both grid and solid shielded DFF and DC-SFQ cells showed improvement in OFMs, especially for the positive currents, as summarised in Table 5.11. The results underscore the argument that improvement in OFMs for one direction of magnetic field direction could compromise the same if the direction reversed. However, with this approach, coupled with good shielding, grid or solid, SFQ circuits can be made more tolerant to magnetic fields of specific orientation, if the orientation is known beforehand.

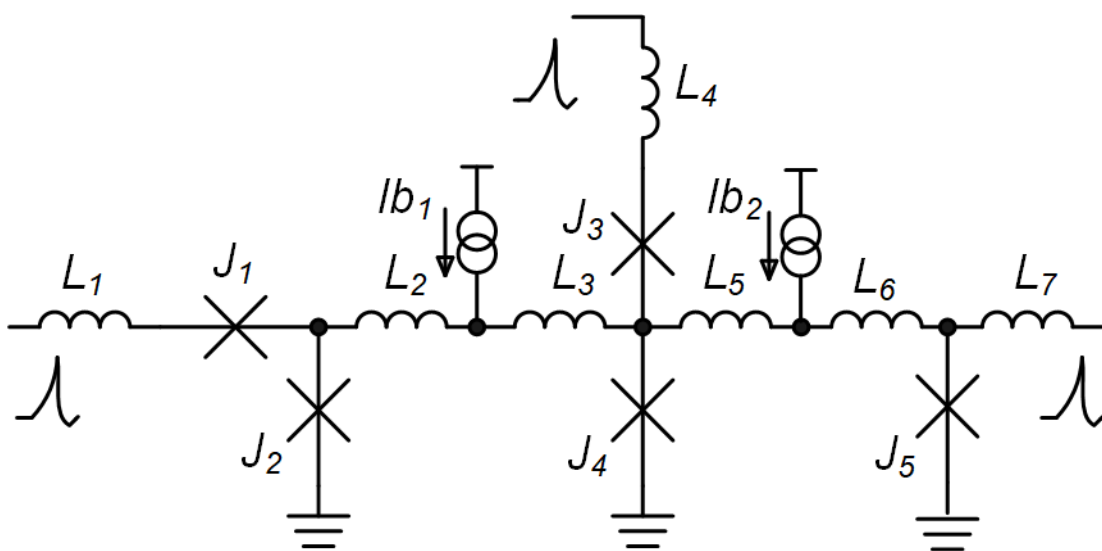


Figure 5.13: A 5-Josephson junction DFF with parameters: $L_1 = 1.86 \text{ pH}$, $L_2 = 1.59 \text{ pH}$, $L_3 = 7.73 \text{ pH}$, $L_4 = 1.5 \text{ pH}$, $L_5 = 2.13 \text{ pH}$, $L_6 = 1.3 \text{ pH}$, $L_7 = 1.91 \text{ pH}$, $J_1 = J_4 = 200 \mu\text{A}$, $J_2 = J_5 = 250 \mu\text{A}$, $J_3 = 150 \mu\text{A}$, $I_{b1} = 230 \mu\text{A}$ and $I_{b2} = 135 \mu\text{A}$. Optimised bias margins: $-53\% \sim 42\%$

¹Part of the work presented in this section was published by the author in [76]

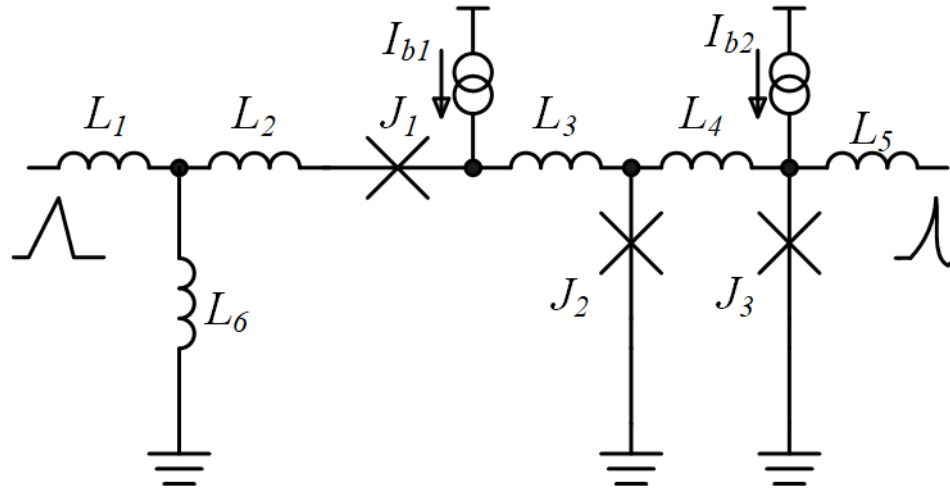


Figure 5.14: A DC-SFQ with parameters: $L_1 = 0.56 \text{ pH}$, $L_2 = 0.52 \text{ pH}$, $L_3 = 1.0 \text{ pH}$, $L_4 = 4.78 \text{ pH}$, $L_5 = 2.2 \text{ pH}$, $L_6 = 4.1 \text{ pH}$, $J_1 = 225 \text{ }\mu\text{A}$, $J_2 = 225 \text{ }\mu\text{A}$, $J_3 = 250 \text{ }\mu\text{A}$, $I_{b1} = 275 \text{ }\mu\text{A}$ and $I_{b2} = 175 \text{ }\mu\text{A}$. Optimised bias margins: $-56\% \sim 34\%$

Name	Margins		
B1	[.....===== =====]	-57.7,	90.0
B2	[.....===== =====]	-19.0,	28.1
B3	[.....===== =====]	-0.7,	70.3
B4	[=====]	-90.0,	0.7
B5	[=====]	-90.0,	2.1
IB1	[.....===== =====]	-2.8,	27.4
IB2	[.....===== =====]	-1.4,	90.0
L1	[===== =====]	-90.0,	90.0
L2	[===== =====]	-90.0,	38.0
L3	[.....===== =====]	-74.5,	1.4
L4	[===== =====]	-90.0,	90.0
L5	[.....===== =====]	-1.4,	90.0
L6	[.....===== =====]	-53.4,	90.0
L7	[.....===== =====]	-15.5,	90.0

(a)

Name	Margins		
B1	[.....===== =====]	-50.6,	4.9
B2	[.....===== =====]	-4.9,	47.1
B3	[.....===== =====]	-0.7,	43.6
IB1	[.....===== =====]	-10.5,	2.8
IB2	[.....===== =====]	-62.6,	0.7
L1	[===== =====]	-90.0,	90.0
L2	[===== =====]	-90.0,	14.8
L3	[.....===== =====]	-6.3,	90.0
L4	[===== =====]	-90.0,	90.0
L5	[===== =====]	-90.0,	7.0
L6	[.....===== =====]	-59.8,	7.0

(b)

Figure 5.15: Margins calculated one step before failure point (OFM) for (a) DFF and (b) DC-SFQ, showing critical components (in boxes) marked for alteration.

Table 5.11: New operating field margins (OFMs) for the DFF and DC-SFQ after selected parameters were altered. OFMs presented for positive & negative currents, respectively.

Cell	Initial OFMs	Altered Parameters	New OFMs
DFF - Grid	98 & 50 μT	$L_5=2.6 \text{ pH}$	126 & 42 μT
DFF - Solid	86 & 50 μT	$L_5=2.6 \text{ pH}$	101 & 32 μT
DC-SFQ - Grid	117 & 67 μT	$L_6=3.5 \text{ pH}$	134 & 67 μT
		$J_1=200 \text{ }\mu\text{A}$ $J_3=275 \text{ }\mu\text{A}$	
DC-SFQ - Solid	113 & 59 μT	$L_6=3.5 \text{ pH}$	123 & 49 μT
		$J_1=200 \text{ }\mu\text{A}$ $J_3=275 \text{ }\mu\text{A}$	

Table 5.12: A comparison of between a no-moat DFF's OFMs to another with moats

Type	xy -coil (z -directed fields)		xz -coil (y -directed fields)		yz -coil (x -directed fields)	
	-OFM	+OFM	-OFM	+OFM	-OFM	+OFM
A (No-Moats)	28 μ T	30 μ T	87 μ T	80 μ T	90 μ T	68 μ T
B (With Moats)	24 μ T	24 μ T	86 μ T	81 μ T	68 μ T	63 μ T

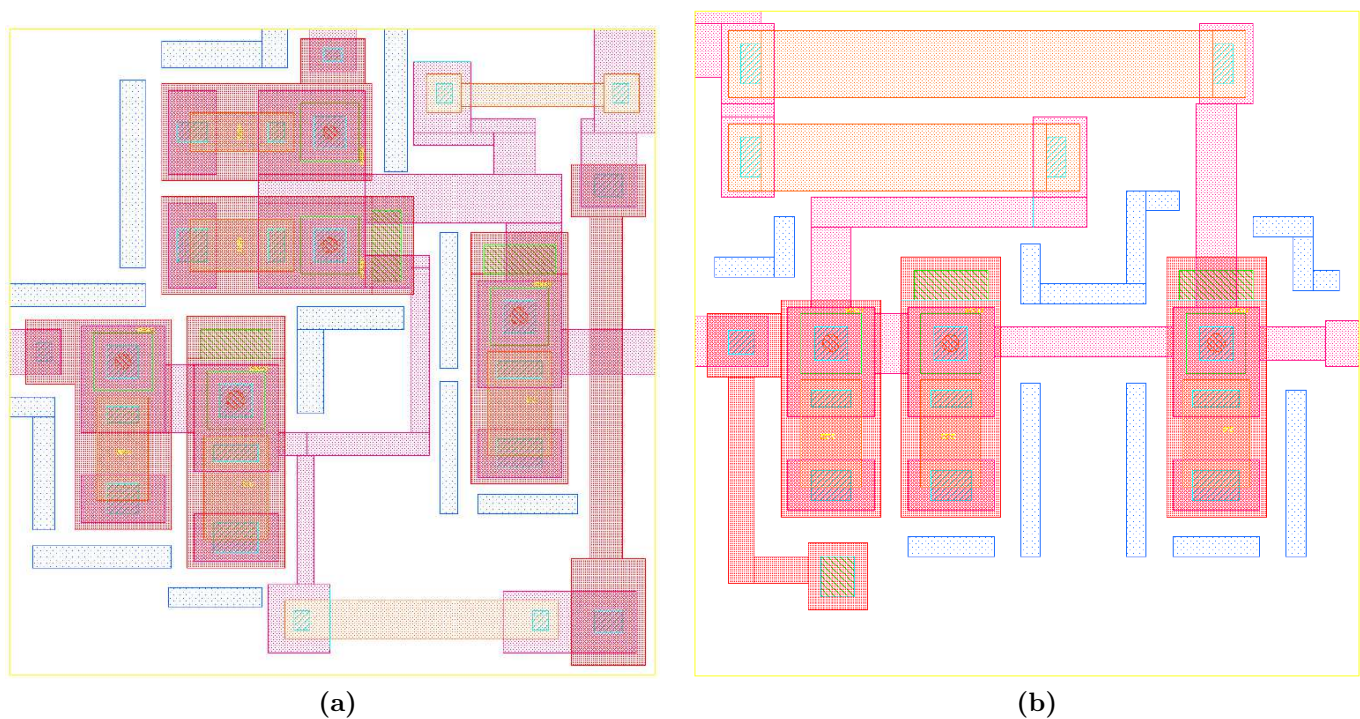
Table 5.13: A comparison of between a no-moat DC-SFQ's OFMs to another with moats.

Type	xy -coil (z -directed fields)		xz -coil (y -directed fields)		yz -coil (x -directed fields)	
	-OFM	+OFM	-OFM	+OFM	-OFM	+OFM
C (No-Moats)	47 μ T	39 μ T	108 μ T	74 μ T	211 μ T	200 μ T
D (With Moats)	36 μ T	44 μ T	48 μ T	47 μ T	202 μ T	120 μ T

5.4 Moats and Magnetic Field Tolerant SFQ Circuits

Moats are rectangular structures that are laid out to create holes in the ground plane. They are crucial in reducing the probability of flux trapping in SFQ circuits. It is widely accepted that the creation of moats is as essential as the circuit itself. However, moats can affect the magnetic field tolerance of SFQ circuits. The ground plane is the return path for both bias currents and shielding currents, where shielding is applied. Moats could interfere with the flow of such currents, thereby compromising or improving the OFMs of such cells. In addition, in the event that there is no trapped flux in the moat, then some flux from the external magnetic fields could couple to the moats. The outcome could be the improvement in OFMs as the moats accommodate some of the flux or the moats could radiate more magnetic fields from the trapped flux to nearby inductors (secondary coupling).

DFF and DC-SFQ cells with moats were analysed with magnetic fields from the xy , xz and yz -coils to calculate the effect that moats could have on their OFMs. The cells, with moats are shown in Fig. 5.16, while the cells without moats are shown in Fig. 5.6. The moats are laid out liberally and can be seen close to most of the Josephson junctions in the layouts in Fig. 5.16.

**Figure 5.16:** Cell layouts with moats (a) DFF and (b) DC-SFQ

In the DFF with moats, Fig. 5.16(a), there is a notable reduction in -OFM for yz -coil (x -directed fields) from 90 μ T in Type A to 68 μ T in Type B (Fig. 5.12). There are small reductions in OFMs in other

orientations as shown in Table 5.12. Nonetheless, the effect of moats on the cells OFMs is still noticeable. The DC-SFQ with moats, (D), had reduced -OFM and +OFM against y -directed fields (from the xz -coil) and a reduction in +OFMs as shown in Table 5.13. Similar to DFF, the DC-SFQ with moats had reduced OFM in all the six magnetic field orientations.

The reduction of OFMs due to the presence of moats depends on the distance between the moats and critical circuit inductance. While serving the purpose of reducing flux trapping, moats could couple to the cell's inductance [79], thereby influencing circuit behaviour, including OFMs.

5.5 Chapter Conclusion

SFQ cell's operating conditions, such as parameter and operating field margins, improve by carefully designing inductors that reduce coupling to external magnetic fields. Different designs of inductors were demonstrated and evaluated using either static magnetic fields or magnetic fields produced by virtual coils. Thin inductors have shown a reduction in coupling to external fields. In addition, inductors that are laid out along the magnetic field plane showed reduced coupling compared to those laid out in a perpendicular fashion. The shielding of specific inductors was also looked into and a configuration that incorporated ground contacts at both ends of a ring shield, proved to be the most effective approach to reduce coupling. Further, it has been demonstrated that the cells could be made immune to external magnetic fields with a design approach that assumes a known quantity of external magnetic fields at the design stage. Tolerance of SFQ circuits to external magnetic fields can be improved by incorporating the methods presented here, including the shielding mechanisms presented before.

Chapter 6

Conclusions and Recommendations

6.1 Conclusions

A method for analysing SFQ circuits in a simulated magnetic field has been evaluated and validated. In this approach, virtual coils, created in *InductEx* were used to project uniform magnetic fields on SFQ cells. Coupling coefficients between the external coils and circuit inductance were then used to determine circuit behaviour at specific magnetic field orientations. The orientation of the simulated magnetic field can be rotated by using a 3-D coil setup with varied coil currents. It is now possible to analyse SFQ circuits with an external magnetic field of any orientation.

Two shielding approaches, the conventional solid shield and the novel grid shield were presented and evaluated in magnetic fields of different orientations. The solid shield is more effective against perpendicular (z -directed) magnetic fields than against those in-plane (x and y -directed fields). In addition, the solid shield's inclusion in SFQ cells results in the reduction of circuit inductance by up to 25 %. The grid shield is a very effective approach against in-plane magnetic fields, even though its effectiveness has shown to degrade with an increase in grid bar spacing. Compared to the solid shield, the grid shield has less effect on circuit inductance with a typical reduction of 8 % at a grid bar spacing of 5 μm . The solid shield has shown to improve the operating field margin of a DFF cell against a z -directed magnetic field from 30 μT to 531 μT , while the grid shield, of 5 μm grid spacing, improved the margin from 68 μT to 290 μT against an x -directed magnetic field. In the DC-SFQ cell, the operating field margin was improved with a solid shield from 47 μT to 464 μT , against a z -directed magnetic field, while with a grid shield, the improvement was from 211 μT to 381 μT , against an x -directed fields.

Grounding has shown to be crucial to the shielding process. This is achieved by incorporating contact vias between the shielding layer and the ground plane. Grounded shields are better at channelling the shielding currents to the ground plane, thereby improving the shielding effectiveness. However, there is a need to carefully lay out ground contacts because grounding causes the shielding layer to conduct part of the currents in the ground plane and that could create secondary coupling to circuit inductance. Uniformly grounded contacts that are close to and on each side of protected circuit inductance are most efficient at providing shielding against in-plane fields, especially with the grid shield. Unlike the solid shield, the grid shield has shown to be more responsive to the positioning of ground contacts. However, in both shields, uniformly laid out ground contacts have shown more predictability in the shield's performance. Shielding has shown to be effective at protecting SFQ circuits against particular orientations of magnetic fields. Therefore, any shielding solution, solid or grid, has to be designed against a known orientation of magnetic field. So far, no shield has shown good effectiveness against all magnetic field orientations.

SFQ circuits can be made more tolerant to external magnetic fields by making changes to the design and layout of circuit inductors. Narrow and short inductors have shown to couple less to external magnetic fields as compared to wide and long ones. Further, selected inductors can be shielded with rings that have ground contacts, to reduce coupling to external magnetic fields. Rings grounded at the ends along the protected inductors have shown to be efficient against x , y and z oriented magnetic fields. At the beginning of the design process, an assumed external magnetic field could be included to design a more tolerant SFQ circuit for such an environment, by altering the most vulnerable circuit parameters.

By incorporating the analysis techniques presented here, the proposed shielding methods and efficient design of inductors and circuit parameters, SFQ circuits can be made more tolerant to magnetic fields from bias lines and external sources, such as the Earth.

6.2 Recommendations

Design of magnetic field tolerant SFQ circuits is a complex subject because a lot of things have to be considered. Firstly, the nature of the SFQ circuits makes them vulnerable to unwanted magnetic field. It has been shown in this document and in literature that minute magnetic fields have a potential to cause malfunction in SFQ circuits. This problem is fundamental to SFQ circuits, hence a modified technology that is inherently immune to magnetic fields could be vital in making circuits that do not need on-chip shielding. Secondly, SFQ circuits have shown to have different operating field margins for varying magnetic field orientations, even after implementing shielding. No shielding implementation has shown good shielding effectiveness against all orientations of magnetic fields. There is still a need for a shield that protects SFQ circuits against magnetic fields of any orientation. Lastly, the fabrication process used in this work, the *Hypres'* 4.5 kA/cm^2 , is still a relatively low integration technology and the Josephson junctions and inductors are of large physical sizes. Wide structures have shown to have higher coupling to external magnetic fields. The use of higher current density fabrication processes could increase SFQ circuit's magnetic field immunity.

To realise further improved magnetic field tolerance of SFQ circuits, a number of things still need to be accomplished. Firstly, shielding could be improved if the layers used for shielding were made thicker, which can only be done by modifying the current fabrication processes. However, this approach could also negatively impact large scale integration. Secondly, the bias lines have to be laid out several layers away from circuit inductance, applicable only to multi-layer fabrication process. Through this method, the circuit could be shielded from coupling to these bias lines.

The solutions, towards magnetic field tolerant SFQ circuit design, presented in the document were accomplished through simulations only. There is a need to have them tested and verified. This requires that the shielding solutions be incorporated in proper on-chip test benches, fabricated at an appropriate foundry and then tested. For testing purposes, Helmholtz coils can be used to generate an ambient magnetic field. At that point the SFQ circuits, with the incorporated solutions, could be tested for bias, parameter and operating field margins in the presence of external magnetic fields.

Bibliography

- [1] K. K. Likharev and V. K. Semenov, "Rsfq logic/memory family: a new josephson-junction technology for sub-terahertz-clock-frequency digital systems," *IEEE Transactions on Applied Superconductivity*, vol. 1, no. 1, pp. 3–28, 1991.
- [2] V. K. Kaplunenko, M. I. Khabipov, V. P. Koshelets, K. K. Likharev, O. A. Mukhanov, V. K. Semenov, I. L. Serpuchenko, and A. N. Vystavkin, "Experimental study of the rsfq logic elements," *IEEE Transactions on Magnetics*, vol. 25, no. 2, pp. 861–864, 1989.
- [3] H. Terai, Y. Kameda, S. Yorozu, A. Fujimaki, and Z. Wang, "The effects of dc bias current in large-scale SFQ circuits," *IEEE Transactions on Applied Superconductivity*, vol. 13, no. 2, pp. 502–506, 2003.
- [4] M. Suzuki, M. Maezawa, and F. Hirayama, "Effects of magnetic fields induced by bias currents on operation of RSFQ circuits," *Physica C: Superconductivity*, vol. 412-414, pp. 1576 – 1579, 2004.
- [5] E. Tolkacheva, H. Engseth, I. Kataeva, and A. Kidiyarova-Shevchenko, "Influence of the bias supply lines on the performance of RSFQ circuits," *IEEE Transactions on Applied Superconductivity*, vol. 15, no. 2, pp. 276–279, 2005.
- [6] R. Collot, P. Febvre, J. Kunert, and H. Meyer, "Operation of low-Tc circuits in a magnetic environment," *IEEE Transactions on Applied Superconductivity*, vol. 23, no. 3, p. 1700404, Jun 2013.
- [7] J. Kang and S. Kaplan, "Current recycling and sfq signal transfer in large scale RSFQ circuits," *IEEE Transactions on Applied Superconductivity*, vol. 13, no. 2, pp. 547–550, 2003.
- [8] O. A. Mukhanov, "Energy-efficient single flux quantum technology," *IEEE Transactions on Applied Superconductivity*, vol. 21, no. 3, pp. 760–769, 2011.
- [9] M. H. Volkmann, A. Sahu, C. J. Fourie, and O. A. Mukhanov, "Implementation of energy efficient single flux quantum digital circuits with sub-aj/bit operation," *Supercond. Sci. Technol.*, vol. 26, no. 1, p. 015002, Nov 2012.
- [10] (2017) British Geological Survey - Natural Environment Research Council. [Online]. Available: http://www.geomag.bgs.ac.uk/data_service/data/annual_means.shtml
- [11] K. Fujiwara, T. Hikida, N. Yoshikawa, A. Fujimaki, S. Yorozu, and H. Terai, "The influence of the ground current on large-scale single-flux-quantum circuits," *Supercond. Sci. Technol.*, vol. 19, no. 5, pp. S362–S365, Mar 2006.
- [12] S. Nagasawa, K. Hinode, T. Satoh, M. Hidaka, H. Akaike, A. Fujimaki, N. Yoshikawa, K. Takagi, and N. Takagi, "Nb 9-layer fabrication process for superconducting large-scale sfq circuits and its process evaluation," *IEICE Transactions on Electronics*, vol. E97.C, no. 3, pp. 132 – 140, 2014.

- [13] H. Akaike, A. Fujimaki, S. Nagasawa, Y. Kitagawa, and M. Hidaka, “Effects of the film thickness of a ground plane in the sfq circuits with a dc-power layer,” *Superconductor Science and Technology*, vol. 20, no. 11, p. S336, 2007.
- [14] C. Fourie, “Full-gate verification of superconducting integrated circuit layouts with inductex,” *IEEE Transactions on Applied Superconductivity*, vol. 25, no. 1, 2015.
- [15] C. J. Fourie, A. Takahashi, and N. Yoshikawa, “Fast and accurate inductance and coupling calculation for a multi-layer nb process,” *Superconductor Science and Technology*, vol. 28, no. 3, p. 035013, 2015.
- [16] C. J. Fourie, S. Miyanishi, and N. Yoshikawa, “Grounding methods to reduce stray coupling in multi-layer layouts,” *15th ISEC 2015*, 2015.
- [17] A. Kadin, R. Webber, and S. Sarwana, “Effects of superconducting return currents on RSFQ circuit performance,” *IEEE Transactions on Applied Superconductivity*, vol. 15, no. 2, pp. 280–283, 2005.
- [18] C. J. Fourie, O. Wetzstein, J. Kunert, H. Toepfer, and H.-G. Meyer, “Experimentally verified inductance extraction and parameter study for superconductive integrated circuit wires crossing ground plane holes,” *Superconductor Science and Technology*, vol. 26, no. 1, p. 015016, 2013.
- [19] H. Akaike, A. Fujimaki, T. Satoh, K. Hinode, S. Nagasawa, Y. Kitagawa, and M. Hidaka, “Effects of a dc-power layer under a ground plane in sfq circuits,” *IEEE Transactions on Applied Superconductivity*, vol. 17, no. 2, pp. 466–469, 2007.
- [20] Y. Mizugaki and R. Kashiwa, “Magnetic shielding effect of grounded superconducting niobium layers,” *Journal of Physics: Conference Series*, vol. 97, no. 1, p. 012056, 2008.
- [21] K. Ehara, A. Takahashi, Y. Yamanashi, and N. Yoshikawa, “Development of pulse transfer circuits for serially biased sfq circuits using the nb 9-layer 1- process,” *IEEE Transactions on Applied Superconductivity*, vol. 23, no. 3, 2013.
- [22] M. Igarashi, Y. Yamanashi, N. Yoshikawa, K. Fujiwara, and Y. Hashimoto, “Sfq pulse transfer circuits using inductive coupling for current recycling,” *IEEE Transactions on Applied Superconductivity*, vol. 19, no. 3, pp. 649–652, 2009.
- [23] M. Johnson, Q. Herr, D. Durand, and L. Abelson, “Differential sfq transmission using either inductive or capacitive coupling,” *IEEE Transactions on Applied Superconductivity*, vol. 13, no. 2, pp. 507–510, 2003.
- [24] S. Bermon and T. Gheewala, “Moat-guarded josephson SQUIDS,” *IEEE Transactions on Magnetism*, vol. 19, no. 3, pp. 1160–1164, 1983.
- [25] R. Robertazzi, I. Siddiqi, and O. Mukhanov, “Flux trapping experiments in single flux quantum shift registers,” *Applied Superconductivity, IEEE Transactions on*, vol. 7, no. 2, pp. 3164–3167, 1997.
- [26] Y. Polyakov, S. Narayana, and V. K. Semenov, *Applied Superconductivity, IEEE Transactions on*, vol. 17, no. 2, pp. 520–525, 2007.
- [27] S. Narayana, Y. A. Polyakov, and V. K. Semenov, “Evaluation of flux trapping in superconducting circuits,” *IEEE Transactions on Applied Superconductivity*, vol. 19, no. 3, pp. 640–643, 2009.
- [28] K. Fujiwara, S. Nagasawa, Y. Hashimoto, M. Hidaka, N. Yoshikawa, M. Tanaka, H. Akaike, A. Fujimaki, K. Takagi, and N. Takagi, “Research on effective moat configuration for nb multi-layer device structure,” *IEEE Transactions on Applied Superconductivity*, vol. 19, no. 3, pp. 603–606, 2009.

- [29] Q. P. Herr, J. Osborne, M. J. Stoutimore, H. Hearne, R. Selig, J. Vogel, E. Min, V. V. Talanov, and A. Y. Herr, “Reproducible operating margins on a 72 800-device digital superconducting chip,” *Superconductor Science and Technology*, vol. 28, no. 12, p. 124003, 2015.
- [30] B. Ebert, T. Reich, T. Ortlepp, P. Febvre, and F. H. Uhlmann, “Influence of trapped flux on critical currents of josephson junctions,” *IEICE Electronics Express*, vol. 5, no. 11, pp. 431–436, 2008.
- [31] K. Suzuki, H. Kawamura, M. Maruyama, T. Hato, H. Suzuki, S. Yorozu, Y. Kameda, Y. Ishimaru, K. Nakayama, H. Wakana *et al.*, “Investigation of the flux state in single-flux-quantum circuits with moats by scanning SQUID microscope,” *Superconductor Science and Technology*, vol. 19, no. 5, p. S316, 2006.
- [32] V. K. Semenov and M. M. Khapaev, “How moats protect superconductor films from flux trapping,” *IEEE Transactions on Applied Superconductivity*, vol. 26, no. 3, pp. 1–10, Apr. 2016.
- [33] Y. Yamanashi and N. Yoshikawa, “Design and evaluation of magnetic field tolerant single flux quantum circuits for superconductive sensing systems,” *IEICE Transactions on Electronics*, vol. 97, no. 3, pp. 178–181, 2014.
- [34] R. Collot, P. Febvre, J. Kunert, H. G. Meyer, R. Stolz, and J. L. Issler, “Characterization of an on-chip magnetic shielding technique for improving sfq circuit performance,” *IEEE Transactions on Applied Superconductivity*, vol. 26, no. 3, pp. 1–5, Apr. 2016.
- [35] S. K. Tolpygo, “Superconductor digital electronics: Scalability and energy efficiency issues,” *Low Temperature Physics*, vol. 42, no. 5, pp. 361–379, 2016.
- [36] T. Ortlepp, O. Wetzstein, S. Engert, J. Kunert, and H. Toepfer, “Reduced power consumption in superconducting electronics,” *IEEE Transactions on Applied Superconductivity*, vol. 21, no. 3, pp. 770–775, 2011.
- [37] Y. Yamanashi, T. Nishigai, and N. Yoshikawa, “Study of lr-loading technique for low-power single flux quantum circuits,” *IEEE Transactions on Applied Superconductivity*, vol. 17, no. 2, pp. 150–153, 2007.
- [38] N. Yoshikawa and Y. Kato, “Reduction of power consumption of rsfq circuits by inductance-load biasing,” *Superconductor Science and Technology*, vol. 12, no. 11, p. 918, 1999.
- [39] Q. Herr, “Single flux quantum circuits,” Patent US Patent 7 724 020, May 25, 2010.
- [40] D. Kirichenko, S. Sarwana, and A. Kirichenko, “Zero static power dissipation biasing of rsfq circuits,” *IEEE Transactions on Applied Superconductivity*, vol. 21, no. 3, pp. 776–779, 2011.
- [41] I. Vernik, S. Kaplan, M. Volkmann, A. Dotsenko, C. Fourie, and O. Mukhanov, “Design and test of asynchronous esfq circuits,” *Superconductor Science and Technology*, vol. 27, no. 4, pp. 44 030–44 036, 2014.
- [42] C. J. Fourie, O. Wetzstein, T. Ortlepp, and J. Kunert, “Three-dimensional multi-terminal superconductive integrated circuit inductance extraction,” *Superconductor Science and Technology*, vol. 24, no. 12, p. 125015, 2011.
- [43] C. Fourie, X. Peng, R. Numaguchi, and N. Yoshikawa, “Inductance and coupling of stacked vias in a multilayer superconductive IC process,” *IEEE Transactions on Applied Superconductivity*, vol. 25, no. 3, pp. 1–4, 2015.

- [44] Inductex v5.04 pro. [Online]. Available: <http://www0.sun.ac.za/ix/?q=home>
- [45] “gEDA,” GNU’s General Public Licence - Electronic Design Automation, <http://www.geda-project.org/>, Tech. Rep.
- [46] J. E. Fang and T. V. Duzer, “A Josephson integrated circuit SIMulator (JSIM) for superconductive electronics application,” *Extended Abstracts of 2nd International Superconductive Electronics Conference*, pp. 407–410, 1989.
- [47] Lasi 6.0. [Online]. Available: <http://www.lasihomesite.com>
- [48] Matlab. [Online]. Available: www.mathworks.com
- [49] Gnuplot. [Online]. Available: <http://www.gnuplot.info/>
- [50] ParaView. [Online]. Available: <http://www.paraview.org/>
- [51] R. S. Bakolo, “Design and implementation of a RSFQ superconductive digital electronics cell library,” Master’s thesis, Faculty of Engineering, Stellenbosch University, 2011.
- [52] M. H. Volkmann, “A superconducting software defined radio frontend with application to the square kilometre array,” Ph.D. dissertation, Stellenbosch: Stellenbosch University, 2013.
- [53] “Ipht, rsfq-design rules for niobium process: Rsfq1d ver. 1.2,” IPHT Jena: <http://www.ipht-jena.de/uploads/media/a13rsfqrul1d.pdf>, Tech. Rep., 2007.
- [54] Hypres, “Niobium integrated circuit fabrication: Design rules rev 24,” Hypres: <http://www.hypres.com>, Tech. Rep., 2008, Jan 11.
- [55] R. S. Bakolo and C. J. Fourie, “Modelling of the influence of magnetic fields on the operation of digital superconductive circuits,” in *15th International Superconductive Electronics Conference (ISEC), 2015*. IEEE, 2015, pp. 1–3.
- [56] “Ipht cell library,” IPHT Jena: <http://www.tu-ilmenau.de/en/kontrast/departement-of-advanced-electromagnetics/research/superconductive-high-speed-electronics/rsfq-cell/cells>, Tech. Rep., 2011.
- [57] P. Febvre, “Private Conversation,” 2015.
- [58] R. S. Bakolo, R. Staden, P. Febvre, and C. J. Fourie, “Modelling magnetic fields and shielding efficiency in superconductive integrated circuits,” *Journal of Superconductivity and Novel Magnetism*, p. 1, Sep. 2016.
- [59] M. N. Sadiku, *Principles of Electromagnetics*, 4th ed. Oxford University Press Inc., 2015.
- [60] S.-b. Liao, P. Dourmashkin, and J. Belcher. (2004) Visualization E&M: Inductance and energy in magnetic fields. [Online]. Available: <http://web.mit.edu/viz/EM/visualizations/coursenotes/modules/guide11.pdf>
- [61] S. Celozzi, G. Lovat, and R. Araneo, *Electromagnetic Shielding*. Wiley Online Library, 2008.
- [62] M. Pavlík, I. Kolcunová, and L. Lisoň, “Measuring the shielding effectiveness and reflection of electromagnetic field of building material,” in *2015 16th International Scientific Conference on Electric Power Engineering (EPE)*. IEEE, 2015, pp. 56–59.
- [63] X. C. Tong, *Advanced materials and design for electromagnetic interference shielding*. CRC press, 2016.

- [64] K. H. Carpenter, “Magnetostatic simulations for design of superconducting magnetic shields,” *IEEE Transactions on Applied Superconductivity*, vol. 6, no. 3, pp. 142–146, Sep. 1996.
- [65] L. Gozzelino, R. Gerbaldo, G. Ghigo, F. Laviano, and M. Truccato, “Comparison of the shielding properties of superconducting and superconducting/ferromagnetic bi- and multi-layer systems,” *Journal of Superconductivity and Novel Magnetism*, p. 1, Aug. 2016.
- [66] W. Hamilton, “Superconducting shielding,” *Revue de physique appliquée*, vol. 5, no. 1, pp. 41–48, 1970.
- [67] F. Pavese, “Magnetic shielding,” in *Handbook of Applied Superconductivity, Volume 2*. Taylor & Francis, 1998, pp. 1461–1483.
- [68] W. Meissner and R. Ochsenfeld, “Ein neuer effekt bei eintritt der supraleitfähigkeit,” *Naturwissenschaften*, vol. 21, no. 44, pp. 787–788, 1933.
- [69] F. London and H. London, “The electromagnetic equations of the supraconductor,” in *Proceedings of the Royal Society of London A: Mathematical, Physical and Engineering Sciences*, vol. 149, no. 866. The Royal Society, 1935, pp. 71–88.
- [70] P. Seidel, *Applied Superconductivity: Handbook on Devices and Applications*. John Wiley & Sons, 2015.
- [71] Y. Mizugaki, K. Yanagisawa, T. Onomi, T. Yamashita, K. Nakajima, H. Yamamori, and A. Shoji, “Magnetic isolation on a superconducting ground plane,” *Japanese Journal of Applied Physics*, vol. 38, no. 10R, p. 5869, 1999.
- [72] Y. Mizugaki, H. Hakii, M. Moriya, K. Usami, and T. Kobayashi, “Mutual inductance coupled through superconducting thin film in niobium josephson integrated circuits,” *Japanese Journal of Applied Physics*, vol. 44, no. 6L, p. L763, 2005.
- [73] K. Suzuki, S. Yorozu, Y. Kameda, and K. Tanabe, “Investigation of magnetic flux state in nb sfq circuits by scanning squid microscope,” *Physica C: Superconductivity and its Applications*, vol. 445, pp. 1034–1036, 2006.
- [74] Y. Mizugaki, R. Kashiwa, M. Moriya, K. Usami, and T. Kobayashi, “Grounding positions of superconducting layer for effective magnetic isolation in josephson integrated circuits,” *Journal of Applied Physics*, vol. 101, no. 11, p. 114509, 2007.
- [75] Y. Mizugaki, A. Kawai, R. Kashiwa, M. Moriya, and T. Kobayashi, “Mutual coupling between two superconducting strip lines horizontally-placed in niobium integrated chips,” in *Journal of Physics: Conference Series*, vol. 234, no. 4. IOP Publishing, 2010, p. 042021.
- [76] R. S. Bakolo, J. A. Delpont, P. Febvre, and C. J. Fourie, “Analysis of a shielding approach for magnetic field tolerant sfq circuits,” *IEEE Transactions on Applied Superconductivity*, vol. 27, no. 4, pp. 1–5, 2017.
- [77] M. Schmelz, “Development of a high sensitive receiver system for transient electromagnetics,” PhD Thesis, 2014.
- [78] R. van Staden, K. Jackman, C. J. Fourie, and P. Febvre, “Influence of the superconducting ground plane on the performance of rsfq cells,” *IEEE Transactions on Applied Superconductivity*, vol. 27, no. 4, pp. 1–4, 2017.

[79] C. Fourie, *InductEx Users Manual*, 2017.

[80] S. Whiteley, "Fasthenry version 3.0wr. available: <http://www.srware.com>, [accessed april 05, 2011]."

Appendix A

Additional Procedure for Magnetic Field Calculations

A.1 Calculation of Parameter Margins with External Magnetic Fields

This is a description of how SFQ circuit operating margins are calculated in the presence of varied external magnetic fields. The magnetic fields are generated by *InductEx* [44] using the coil system method or the static magnetic field generator engine. This discussion focuses on the latter method, however, the steps followed and the MATLAB code used, are transferable to the coil method. Bias and parameter margins are calculated in the presence of magnetic fields from the x , y and z directions. In this outline, a Josephson Transmission Line (JTL) has been used. The JTLs schematic was captured in gEDA's schematic editor, gschem [45] and its layout was made in LASI [47].

The generated magnetic field uses a virtual inductor of 1 H , which makes it easy to incorporate the external magnetic fields in a circuit schematic. For example, if the required magnetic field is 10 μT , then, with the 1 H inductor, the required current in that loop is 10 μA . All the coupling coefficients, for each magnetic field orientation, are then incorporated in the schematic.

The schematic for the JTL is shown in Fig. A.1 and its layout is shown in Fig. A.2. In the schematic, the magnetic field inductor LF1 can be seen, including the coupling coefficients between the 4 JTL's inductors and the y -directed magnetic fields. The mutual and self inductances are calculated from the JTL layout shown in Fig. A.2.

In order to calculate margins, three files are required. These are the circuit file (netlist, .js or .cir), population (.pop) file which contains the design parameter values and their required spread and a file that contains the required switching patterns (.sp) of Josephson junction. In a case where an external magnetic field needs to be varied, a script that automates the process of increasing the field current, calculates margins at each step and either store or displays the results, becomes handy. In the view of this a MATLAB script was written to automate the process. The script is shown in Listing A.1.

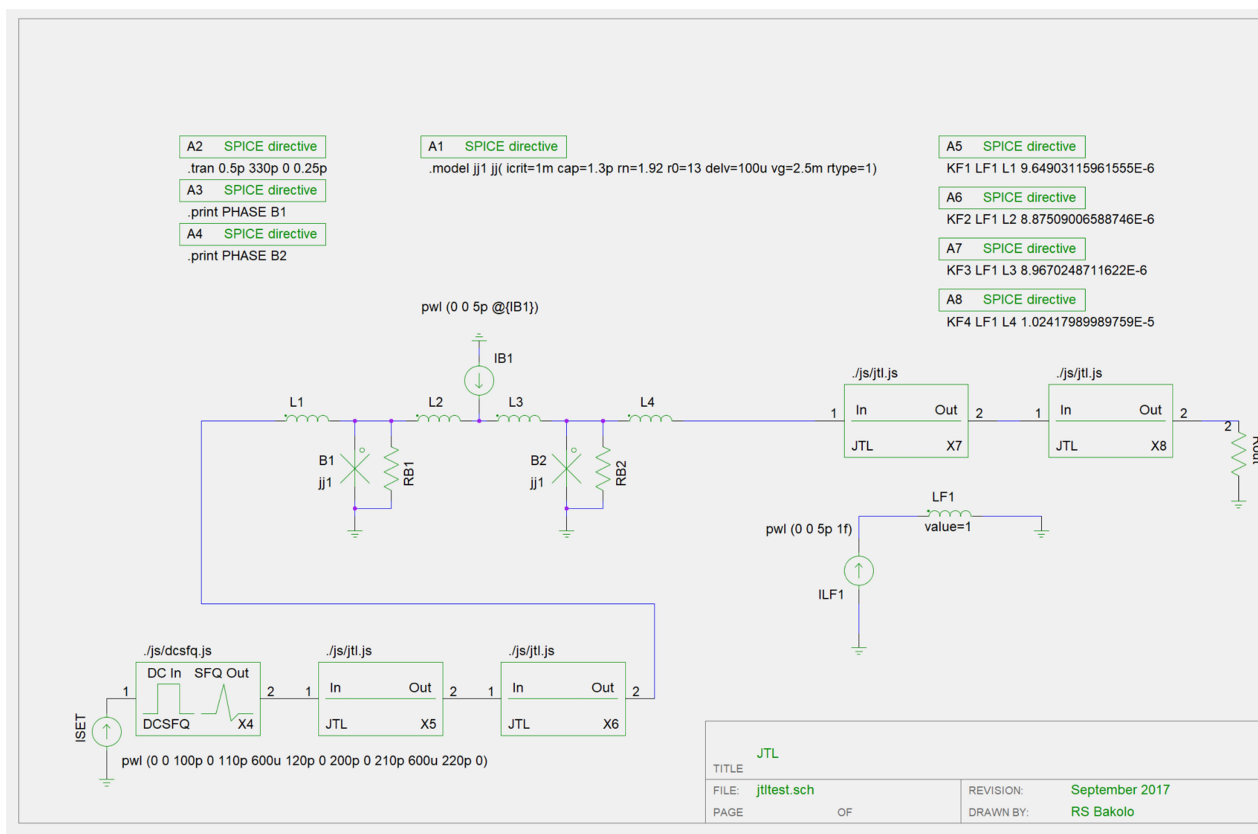


Figure A.1: JTL schematic showing the magnetic field inductor LF1 and simulated current ILF1

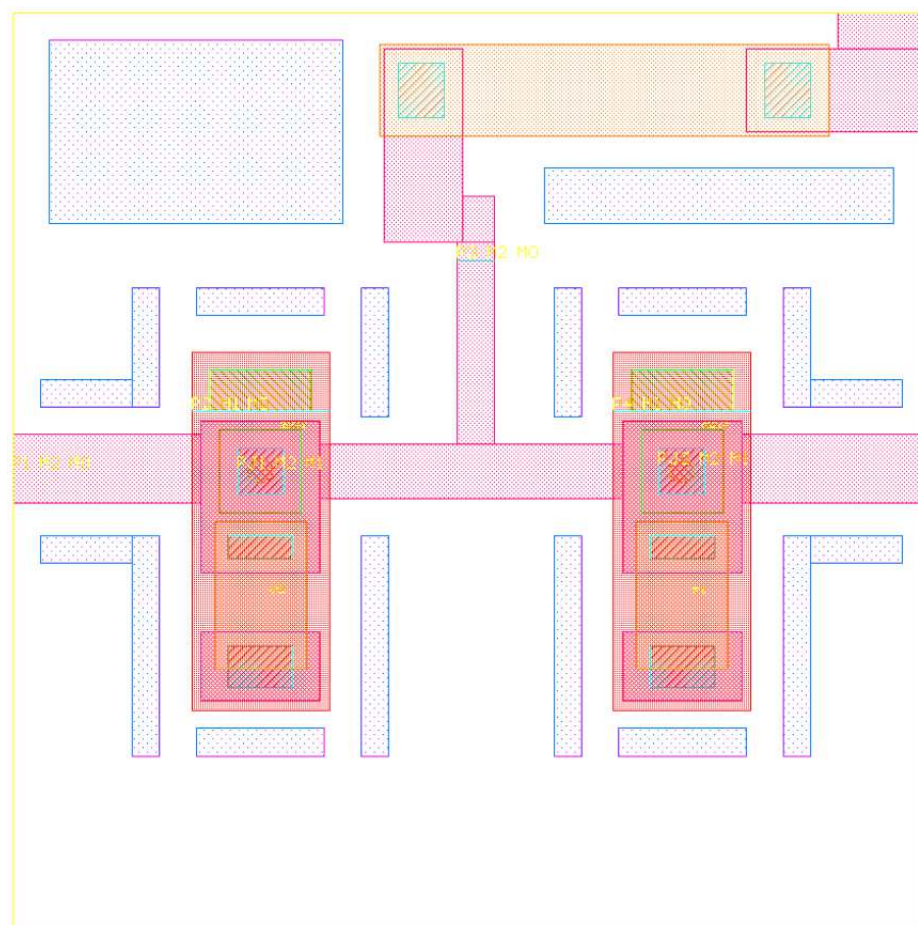


Figure A.2: JTL Layout made in LASI 6

The script is located in the $C:\Program Files (x86)\geda\lib$ directory. Therefore, MATLAB needs to be run with administrative privileges. The user is prompted to enter the name of the schematic file stored in the same location as the script. The script generates the circuit file (.js). Then, the script searches the circuit file for the line that contains the coil current ILF1 and replaces it with a new one that contains a new value of current. Thereafter, margins are calculated using the .sp and .pop files.

Finally, the calculated margins are displayed on the MATLAB command window and also stored in a text file.

Listing A.1: A MATLAB code for iterative calculation of parameter and bias margins

```

1  %Calculation of margins and failure points of SFQ cells
2  %Searching for particaular ILF1 and replacing it
3  %By Rodwell S Bakolo, Contributor: Dr. Nicasio Maguu Muchuka
4  %Date: 26-04-2016, Updated: 28-09-2017
5  clc;
6  clear;
7  filename = input('Please enter file name without extension: ', 's');
8  x_filename = strcat(filename, '.js');
9  new_file = strcat(filename, '-xy.js');
10 % Switches
11 g = '-g';
12 0 = '-0';
13 v = '-v';
14 o = '-o';
15 m = '-m';
16 ma = '-ma';
17 sch_file = strcat(filename, '.sch');
18 dos('cd c:\Program files (x86)\geda\lib\ ', '-echo');
19 construct_gnet = {'gnetlist' g 'spice-sdb' 0 'jsim' 0 'param' o
    x_filename sch_file};
20 cmd_gnet = strjoin(construct_gnet);
21 dos(cmd_gnet);
22 fid = fopen('output.txt', 'a+');
23 %Picking and replacing a line in text file
24 for new_value=0:0.000001:0.0001
25     fidin = fopen(x_filename, 'r');
26     fidout = fopen(new_file, 'w');
27     line = fgetl(fidin);
28     while ~feof(fidin)
29         fprintf(fidout, '%s\n', line);
30         line = fgetl(fidin);
31         x = strfind(line, 'ILF1');
32         if x ==1
33             y = num2str(new_value);
34             string_start = sprintf('%s %s', 'ILF1 0 11 pwl(0 0 5p', y);
35             new_string = strcat(string_start, ')');
36             line = new_string;
37         end
38     end
39 fprintf('\n%s\n', 'Margin Analysis for Coil Current = ', new_value)
40 construct_ma = {'analyse' ma new_file './sp/jtltestnew1-y.sp' './pop/
    jtltestnew1-y.pop'};
41 cmd_ma = strjoin(construct_ma);

```

```

42 [status, Result] = dos(cmd_ma, '-echo');
43
44         fwrite(fid, Result);
45 fclose(fidin);
46 fclose(fidout);
47 end
48 fclose(fid);
49 fclose all;

```

The JTL, shown in Fig. A.1 (schematic) and Fig. A.2 (layout) was simulated with currents that ranged from 0 to 100 μA . The calculated margins are shown in Fig. A.3(a), Fig. A.3(b), Fig. A.3(c), Fig. A.4(a), Fig. A.4(b) and Fig. A.4(c) for 0 μA , 10 μA , 20 μA , 30 μA , 40 μA and 47 μA respectively. The margins can be seen to get narrower as the external magnetic field is increased. The margins of the circuit keep shrinking until at 47 μA (47 μT) where total failure occurs. This point is referred to as the failure point or the operating fields margin (OFM) for the cell. The circuit produces uncharacteristic pulses or none at all and in such instances, some junctions might not switch at all.

Name	Margins		
B#	[.....===== =====.....]	-54.1,	70.3
B1	[..===== =====..]	-85.8,	83.0
B2	[...===== =====...]	-83.0,	80.9
I#	[.===== =====.....]	-87.2,	73.1
IB1	[.===== =====.....]	-87.2,	73.1
L#	[===== =====]	-90.0,	90.0
L1	[===== =====]	-90.0,	90.0
L2	[===== =====]	-90.0,	90.0
L3	[===== =====]	-90.0,	90.0
L4	[===== =====]	-90.0,	90.0

(a)

Name	Margins		
B#	[.....===== =====.....]	-50.6,	71.0
B1	[.....===== =====]	-73.1,	90.0
B2	[===== =====.....]	-90.0,	68.9
I#	[.....===== =====.....]	-74.5,	69.6
IB1	[.....===== =====.....]	-74.5,	69.6
L#	[===== =====]	-90.0,	90.0
L1	[===== =====]	-90.0,	90.0
L2	[===== =====]	-90.0,	90.0
L3	[===== =====]	-90.0,	90.0
L4	[===== =====]	-90.0,	90.0

(b)

Name	Margins		
B#	[.....===== =====.....]	-44.3,	58.4
B1	[.....===== =====]	-58.4,	90.0
B2	[===== =====.....]	-90.0,	57.0
I#	[.....===== =====.....]	-61.9,	59.1
IB1	[.....===== =====.....]	-61.9,	59.1
L#	[===== =====]	-90.0,	90.0
L1	[===== =====]	-90.0,	90.0
L2	[===== =====]	-90.0,	90.0
L3	[===== =====]	-90.0,	90.0
L4	[===== =====]	-90.0,	90.0

(c)

Figure A.3: Margins of the JTL against a y-directed magnetic field produced with a current ILF1 through Inductor LF1. The margins calculated at (a) ILF1=0 μA , (b) ILF1=10 μA and ILF1=20 μA .

Name	Margins		
B#	[..... =====]	-33.0,	46.4
B1	[..... =====]	-41.5,	90.0
B2	[=====]	-90.0,	45.7
I#	[..... =====]	-49.2,	44.3
IB1	[..... =====]	-49.2,	44.3
L#	[===== =====]	-90.0,	90.0
L1	[===== =====]	-90.0,	90.0
L2	[===== =====]	-90.0,	90.0
L3	[===== =====]	-90.0,	90.0
L4	[===== =====]	-90.0,	90.0

(a)

Name	Margins		
B#	[..... =====]	-16.9,	34.5
B1	[..... =====]	-19.0,	90.0
B2	[..... =====]	-75.2,	34.5
I#	[..... =====]	-36.6,	21.8
IB1	[..... =====]	-36.6,	21.8
L#	[===== =====]	-90.0,	87.9
L1	[===== =====]	-90.0,	90.0
L2	[..... =====]	-51.3,	90.0
L3	[=====]	-90.0,	67.5
L4	[... =====]	-82.3,	90.0

(b)

Name	Margins		
B#	[..... =====]	0.0,	26.0
B1	[..... =====]	0.0,	90.0
B2	[..... =====]	0.0,	26.7
I#	[..... =====]	-27.4,	0.0
IB1	[..... =====]	-27.4,	0.0
L#	[..... =====]	0.0,	59.8
L1	[=====]	-90.0,	0.0
L2	[..... =====]	0.0,	90.0
L3	[=====]	-90.0,	0.0
L4	[..... =====]	-68.9,	0.0

(c)

Figure A.4: Margins of the JTL against a y-directed magnetic field produced with a current ILF1 through Inductor LF1. The margins calculated at (a) ILF1=30 μ A, (b) ILF1=40 μ A and ILF1=47 μ A.

The procedure described up this point is only in one direction of magnetic field, however, the other directions, x and z could be analysed in the same manner by replacing the coupling coefficients in the schematic. If the coil system is used, then the inductance of the coil should be used instead of the 1 H inductor used in the static magnetic field model. *InductEx* calculates the inductance of the coils and their coupling coefficients to circuit inductance. If three directions of magnetic field, using the static magnetic field or the coil method, are required in a single simulation, then the MATLAB code in Listing A.1 needs to be modified as shown in Listing A.2. The inductor or coil currents for each direction are varied at the same time. This results in a resultant magnetic field that is a vector sum of the three magnetic field orientations, hence its orientation is different from the fundamental directions. The orientation of the resultant field could be changed by varying the currents accordingly, as described earlier in this document.

Listing A.2: A MATLAB code for iterative calculation of parameter and bias margins

```

1 %Calculation of margins and failure points of SFQ cells with 3 field
  directions
2 %Searching for particaular IBX1,IBX2 and IBX3 and replacing them
3 %By Rodwell S Bakolo, Contributor: Dr. Nicasio Maguu Muchuka
4 %Date: 26-04-2016, Updated: 28-09-2017
5 clc
6 clear
7 filename = input('Please enter file name without extension: ', 's');
8 x_filename = strcat(filename, '.js');
9 new_file = strcat(filename, '-xy.js');
10 % Switches
11 g = '-g';
12 O = '-O';
13 v = '-v';
14 o = '-o';
15 m = '-m';
16 ma = '-ma';
17 sch_file = strcat(filename, '.sch');
18 dos('cd c:\Program files (x86)\geda\lib\ ', '-echo');
19 construct_gnet = {'gnetlist' g 'spice-sdb' O 'jsim' O 'param' o
  x_filename sch_file};
20 cmd_gnet = strjoin(construct_gnet);
21 dos(cmd_gnet);
22 %Picking and replacing a line in text file
23 fid = fopen('output.txt', 'a+');
24 for new_value=0.012:0.0001:0.025
25     fidin = fopen(x_filename, 'r');
26     fidout = fopen(new_file, 'w');
27     line = fgetl(fidin);
28     while ~feof(fidin) %ischar(line)
29         fprintf(fidout, '%s\n', line);
30         line = fgetl(fidin);
31         x1 = strfind(line, 'IBX1');
32         x2 = strfind(line, 'IBX2');
33         x3 = strfind(line, 'IBX3');
34         if x1 == 1
35             new1 = (new_value);
36             y1 = num2str(new1);
37             string_start = sprintf('%s %s', 'IBX1 0 9 pwl(0 0 5p', y1);
38             new_string = strcat(string_start, ')');
39             line = new_string;
40         end
41         if x2 == 1
42             new2 = (new_value);
43             y2 = num2str(new2);
44             string_start = sprintf('%s %s', 'IBX2 0 10 pwl(0 0 5p', y2)

```

```

        ;
45     new_string = strcat(string_start,')');
46     line = new_string;
47     end
48     if x3 == 1
49         new3 = (new_value);
50         y3 = num2str(new3);
51         string_start = sprintf('%s %s','IBX3 0 11 pw1(0 0 5p',y3)
        ;
52         new_string = strcat(string_start,')');
53         line = new_string;
54     end
55     end
56 fprintf('\n%s\n', 'Margin Analysis for Coil Current = ', new_value)
57 construct_ma = {'analyse' ma new_file './sp/dcsfqh-3c-grid.sp' './pop
        /dcsfqh-3c-grid.pop'};
58 cmd_ma = strjoin(construct_ma);
59 [status, Result] = dos(cmd_ma, '-echo');
60
61         fwrite(fid, Result);
62 fclose(fidin);
63 fclose(fidout);
64 end
65 fclose(fid);
66 fclose all;

```

A.2 Circuit's Failure Point

In the simulations conducted in this work, the term failure point was used to also mean the operating field margin (OFM). This is a point at which the margin analysis results of a particular circuit show a 0% on a parameter of bias current spread. It was observed that at output SFQ pulses begin to show errors at that point. Therefore, this is the point at which the circuit fails and this also happens at a particular external coil current, that produces a magnetic field to cause the circuit failure. This explains why this point is also called the OFM of the circuit. Apart from calculating OFMs, the method could be used to simply observe circuit margins, parameter and bias, in the presence of external magnetic fields.

Appendix B

Software Tools

B.1 *InductEx*

InductEx [42–44, 79] is arguably the world’s most powerful inductance extraction tool. It is a back and front end that uses a highly modified *FastHenry* [80] engine to calculate inductance in superconducting circuit structures. *InductEx* accepts industry-standard graphic database system version 2 (GDSII) file format. GDS contains all the geometry, text and types of structures in a layout, which may include superconducting and resistive layers. A layer definition file (LDF) is needed to match and provide interpretation of the layer numbers and necessary fabrication process data. Lastly, *InductEx* needs a circuit netlist file that matches the structures and ports in the layout. The 3-D numerical solver, *FastHenry*, is then called to execute the extraction of parameters from a 3-D model of the GDS file [14, 79]. *InductEx* was used extensively throughout this work to extract parameters, such as self and mutual inductance, Josephson junction critical currents and resistance. *InductEx* enables calculation of inductance of via structures and it is well suited for single layer and multilayer structures. In addition, *InductEx* also calculates the current distribution in conductors including magnetic field distribution. Another special feature of *InductEx* is that it can be executed from the command line, but also integrates easily with graphical user interface based applications. At the time of writing, *InductEx* has been equipped with two methods that enables the incorporation of external magnetic fields. These include the use of external virtual superconducting coils and a another that generates static magnetic fields directly onto the chip. The coil method was used extensively in this work, because it was developed early enough to take advantage of. However, the static magnetic field method was used in Chapter 5. Both methods are described in detail in the *InductEx* Manual [79]. For further evaluation of results, *InductEx* also has bundled visualisation tools, which include *Inp2dxf*, *Idensity* and *Magix*.

B.2 gEDA

GNU’s general public license electronic design automation (*gEDA*) [45], is a toolkit for schematic capture (*gschem*), for creating SPICE netlists (*gnetlist*), among others. Under the Stellenbosch software toolkit, *gEDA* is used with Josephson SIMulator (*JSIM*) or its noise enabled version, *jsim_n* for circuit simulations. *gEDA* is open-source and custom circuit models can be added. Its graphical user interface makes it easy to build and edit circuit schematics.

B.3 Stellenbosch University (SU) Tool set

The SU tool set is a set of purpose built interrelated tools that are used in the analysis of superconducting circuits. These include:

- **apply** is used to load fixed nominal values for circuit parameters in a netlist, from a user created text file called a population. This produces a simulation-ready netlist. In addition, noise sources can also be incorporated at this stage. The netlist is generated from an original file that is generated by **gnetlist**,
- **jsim_n** is simply a modified version of **JSIM** that accepts circuit files with noise sources. Otherwise, if no noise sources are included in a circuit file, **JSIM** should suffice. This tool was used in this work to determine the transient response of superconducting circuits. The output junction phase waveforms are then properly marked to determine margin, yield or Bernoulli analyses and
- **analyse** is a tool that enables calculation of bias and parameter margins, yield and Bernoulli analyses. This program uses a circuit file, a file that contains junction switching characteristics and a population file that contains all the parameters that need to be varied during any of the analyses. Special directives within the population determine the number of runs each set of parameters has to be tested for averaging purposes.

B.4 LASI

All the layouts in this work were done in LAYOUT System for Individuals (LASI) [47], which is an open source layout tool that has been there for a long time. It has been used extensively in the semiconductor industry. LASI 6 and 7 can be modified for superconductor circuit layouts. Currently, LASI can accept design files that conform to the Institute of Photonic Technology (IPHT) and Hypres processes and others. The popularity of LASI lies in the attribute that it is free and it also generates an industry standard, GDS file format, which is a production ready format. One of the limitations of LASI is the absence of a design rule checker for superconducting circuit layouts and a layout-versus-schematic verifier.